ABSTRACT

MECHANISMS OF OSCILLATIONS AND POLYGLOT ENTRAINMENT IN NEURONAL AND CIRCADIAN MODELS

by
Emel Khan

Entrainment is a type of synchronization in which the period of an endogenous oscillator matches the period of an external forcing signal and a stable phase relationship is maintained between them. Entrainment patterns are described in terms of the number of input oscillations (N) that are phase-locked to a number of output oscillations (M), referred to as N:M patterns. Arnold tongue diagrams are used to depict the regions of N:M entrainment patterns in the input period-amplitude parameter space. Although the entrainment of self-sustained oscillators by periodic forcing are well investigated is a well-studied problem, entrainment of damped oscillators has been less explored. This thesis characterizes entrainment responses for several models of biological oscillators with the unforced system in different dynamic regimes, such as an unstable focus with large amplitude oscillations, a stable focus with weakly damped oscillations, and a stable focus with strongly damped oscillations. The main finding of this dissertation is the existence of multiple disconnected 1:1 entrainment regions when the unforced system is in the vicinity of a Hopf bifurcation. This entrainment structure is termed *polyglot* to distinguish it from the single 1:1 entrainment region (*monoglot*) structure typically observed in Arnold tongue diagrams. The emergence of polyglot entrainment is then explained using phase plane analysis and other dynamical systems tools.

Chapter 1 provides an introduction to oscillator theory and the importance of biological oscillations. Chapters 2 and 3 consider the Fitzhugh-Nagumo model of neuronal oscillations and explore its entrainment properties. Chapter 4 focuses on two models of circadian (∼24-hour) rhythms in cyanobacteria and uncovers the

dynamical mechanism underlying post-translational oscillations (PTOs). Chapter 5 then analyzes entrainment of these PTO models. In Chapter 6, entrainment results are presented for other models of neuronal, circadian, and glycolytic oscillations. These investigations lead to the conclusion that polyglot entrainment structure (multiple 1:1 regions) is observed when the unforced system is in the vicinity of a Hopf bifurcation and the Hopf point is located near a knee of a cubic nullcline. Concluding thoughts and future work are presented in Chapter 7.

MECHANISMS OF OSCILLATIONS AND POLYGLOT ENTRAINMENT IN NEURONAL AND CIRCADIAN MODELS

by
Emel Khan

A Dissertation
Submitted to the Faculty of
New Jersey Institute of Technology and
Rutgers, The State University of New Jersey – Newark
in Partial Fulfillment of the Requirements for the Degree of
Doctor of Philosophy in Mathematical Sciences

Department of Mathematical Sciences

May 2021

APPROVAL PAGE

MECHANISMS OF OSCILLATIONS AND POLYGLOT ENTRAINMENT IN NEURONAL AND CIRCADIAN MODELS

Emel Khan

Dr. Casey O. Diekman, Dissertation Co-Advisor — Date
Associate Professor of Mathematical Sciences, NJIT

Dr. Horacio G. Rotstein, Dissertation Co-Advisor — Date
Professor of Biological Sciences, NJIT

Dr. Amitabha K. Bose, Committee Member — Date
Professor of Mathematical Sciences, NJIT

Dr. Yong-Ick Kim, Committee Member — Date
Assistant Professor of Chemistry and Environmental Science, NJIT

Dr. James N. MacLaurin, Committee Member — Date
Assistant Professor of Mathematical Sciences, NJIT

BIOGRAPHICAL SKETCH

Author: Emel Khan

Degree: Doctor of Philosophy

Date: May 2021

Undergraduate and Graduate Education:

- Doctor of Philosophy in Mathematical Sciences,
  New of Jersey Institute of Technology, Newark, NJ, 2021
- Master of Science in Applied Mathematics,
  New Jersey Institute of Technology, Newark, NJ, 2017
- Bachelor of Science in Mathematics,
  University of Peshawar, Peshawar, KPK, 2005

Major: Mathematical Sciences

Publications:

Emel Khan, Soheil Saghafi, Casey O. Diekman, and Horacio G. Rotstein "The Emergence of Polyglot Entrainment Responses to Periodic Inputs in Vicinities of a Hopf Bifurcation". *(In Preparation)*

Emel Khan, Casey O. Diekman, Horacio G. Rotstein, and Soheil Saghafi "Mechanisms of Oscillations in Post-translational Circadian Clock Models". *(In Preparation)*

Ning Wei, Soheil Saghafi, Emel Khan, and Casey O. Diekman "Circadian Rhythms and COVID-19: Modeling Circadian Clock Regulation of Immune System Response to SARS-CoV-2 Infection and Treatment with Remdesivir". *(In Preparation)*

Presentations:

Soheil Saghafi and Emel Khan, "Circadian Rhythms and COVID-19: Modeling Circadian Clock Regulation of Immune System Response to SARS-CoV-2 Infection and Treatment with Remdesivir," *NSF Student Conference on COVID19 Modeling*, University of Texas at Dallas (Virtual), January 29, 2021.

M. Polin, O. Iaroshenko, C. Bisnath, D. Nigro, A. Korn, B. DeCourcy and Emel Khan, "Mathematical Modeling of Capillary Origami," *Graduate Student Math Modeling Camp (GSMMC) and Mathematical Problems in Industry (MPI)*, June 14, 2013.

Posters:

Emel Khan, "Modeling of Cyanobacterial Circadian Oscillations," *Institute for Brain and Neuroscience Research* , New Jersey Institute of Technology, April 29, 2019.

Emel Khan, Horacio G. Rotstein, and Casey O. Diekman "Investigating Frequency Preferences of Chemical Systems in Response to Periodic Forcing," *Dana Knox Student Research Showcase* , New Jersey Institute of Technology, April 20, 2016.

I dedicate my dissertation work to my parents, Akhtar Munir and Ulfat Begum, my wife, Zobia Khooban, and my children, Haider Khan and Hafsa Khan for their unconditional love and support

ACKNOWLEDGMENT

Though my Ph.D. took many unwanted turns and bumps, I have been surrounded by wonderful people and their phenomenal support throughout these past years.

First and foremost, I would like to thank my dissertation advisors, Prof. Casey O. Diekman and Prof. Horacio G. Rotstein, for their extraordinary support. I am truly blessed to have such great advisors. They helped me both academically and on a personal level and made it possible for me to complete my PhD dissertation.

I would also like to thank my committee members for their insightful discussion and support. Learning dynamical system concepts from Prof. Amitabha K. Bose in discussion sessions has been a great experience. Prof. Yong-Ick Kim provided helpful details and experimental data related to my project. Prof. James N. MacLaurin has shown a very welcoming approach during my research and discussion sessions.

I have huge respect for Prof. Denis Blackmore and thank him for our discussions on topics related to the dynamical system. Thank you to Prof. David Shirokoff for allowing me to use your computer screen, which helped me a lot in the writing of this dissertation.

I am thankful to New Jersey Institute of Technology and the Department of Mathematical Sciences for offering me admission and financial support to pursue my Ph.D. degree. It has been a great experience working as a teaching assistant.

Many thanks to the math department administrative staff for their untiring services they have been offering to all Ph.D. students. Great team!

Special thanks to Soheil Saghafi for collaborating on this project and for his marvelous support. Soheil Saghafi and Sepideh Nikookar, thanks for offering countless rides to schools. You guys have been a great support. Best wishes to both of you for your upcoming Ph.D. proposals. Many thanks to my other fellow graduate students,

Omar Itani and Guangyuan Liao for their generous support and perceptive discussion of mathematical neuroscience and dynamical system.

I would also like to thank my friends, Pejman Sanaie, Christeen Bisnath and Kaiser Niknam for their support.

Special thanks to my US community friends, Abdul Wahab Zafar, Shaheda Begum Shaik, Riaz Choudhary, Fraz Zafar, Hamza Hassun, Furqan Akhtar, Faheem Arshad and Raza Rafique for their love and support these past years.

My sincere gratitude to my mentors Aurangzeb Khan and Falaknaz Khan. Their support and counseling have been very instrumental in my career decisions

I acknowledge my employer, Kohat University of Science and Technology, for countless favors related to my study leave and official matters. A special shout-out to my friends, Asad Ullah, Asif Jan, Shahid Khan, Israr Khan, Fawad Ullah, Ikram Ullah, Yasir Saeed, Mohammad Zaman, Salman Sadiq, and Adnan Khan for believing in me that I can achieve this. If I have missed naming anyone, I apologize.

Heartfelt thanks to my parents, Akhtar Munir and Ulfat Begum for their unconditional love and encouragement. Dad, mom, brothers, and sister, without your support, I never would have achieved this.

Finally, many thanks to my wife, Zobia Khooban, who has been by my side through tough times. I married the best person indeed.

TABLE OF CONTENTS

TABLE OF CONTENTS
(Continued)

Chapter **Page**

LIST OF TABLES

Table **Page**

LIST OF FIGURES

Figure **Page**

LIST OF FIGURES
(Continued)

Figure **Page**

LIST OF FIGURES
(Continued)

Figure **Page**

LIST OF FIGURES
(Continued)

Figure **Page**

LIST OF FIGURES
(Continued)

Figure **Page**

LIST OF FIGURES
(Continued)

Figure **Page**

LIST OF FIGURES
(Continued)

Figure **Page**

LIST OF FIGURES
(Continued)

Figure **Page**

CHAPTER 1

INTRODUCTION

1.1 Background

In a deterministic dynamical system, an oscillation is a solution that repeats in time. Such periodic solutions occur across different time scales ranging from milliseconds in models of neuronal oscillations to years in models of ecological and epidemiological oscillations. Rhythmic events are ubiquitous in nature across biological, chemical, and physical systems and can be modeled as limit cycle oscillations. A limit cycle is an isolated closed trajectory. If the limit cycle is stable, then all trajectories in its vicinity will approach the limit cycle as time goes on to infinity [88]. This property distinguishes limit cycles, which only exist in nonlinear systems, from linear oscillators for which the amplitude of the oscillation depends on initial conditions. Furthermore, linear oscillations always have a sinusoidal waveform, whereas limit cycle oscillators can exhibit various waveforms depending on parameters. Since biological oscillations are not usually sinusoidal and tend to have a characteristic amplitude independent of initial conditions, limit cycles are often used to model them. Examples of limit cycle oscillations in biological systems include the repetitive firing of action potentials in neurons, glycolytic oscillations, and circadian ($\sim$24-hour) oscillations.

Neuronal oscillations are generated either due to intrinsic mechanisms in a single neuron or via coupling between neurons. Such oscillations occur at various frequencies and are important for communication between different parts of the brain [84]. They are also associated with different cognitive processes [30]. Glycolytic oscillations are found in many cells, e.g., pancreatic beta cells and muscle cells. Such oscillations have important implications for glucose-stimulated insulin secretion [8, 85]. Circadian oscillations are observed at multiple scales from the cellular level

up through the behavior of whole organisms. Experiments by Carl Johnson and his group demonstrated that from an evolutionary point of view, the ability of circadian oscillations in cyanobacteria to synchronize to external forcing enhances their reproductive fitness [98]. In particular, they found that strains of cyanobacteria that could entrain to light-dark cycles outcompeted strains that could not entrain.

1.2 Entrainment of Different Types of Oscillators

The interaction of periodic forcing with an oscillator unveils some interesting dynamical phenomenon. One of them is a type of synchronization called entrainment. Entrainment occurs when the period of an endogenous oscillator matches the period of an external forcing signal and a stable phase relationship is maintained between them [18, 40, 63, 77, 78]. Equivalent terminologies for entrained solutions are 'mode-locked', 'frequency-locked', or 'phased-locked' solutions [77]. When an external periodic forcing drives an autonomous system and there is no feedback from the system to the external forcing, it is an example of *unidirectional coupling*. An example of such coupling is the effect of the light-dark cycle (external forcing) on the circadian oscillator of a system. When entrainment occurs, the region of entrainment is well represented by a two-parameter bifurcation diagram called an *Arnold tongue* [4,73,77]. Within the entrained region, the period of the intrinsic oscillator is adjusted to match the period of an external periodic forcing and we have 1:1 phase-locked solutions. The phenomenon of 1:1 entrainment is a particular case of more general $N : M$ synchronization [4]. In synchronization language, here $N : M$ means N cycles of forcing and M cycle of response. Outside the 1:1 region, we have synchronization of other orders like 2:1, 3:1, 3:2, 2:3, 1:2 etc. For example, within a 2:1 phase-locked region, for every two cycles of input, we have one cycle of the response. For a fixed amplitude of external forcing, different orders of synchronization can be achieved by changing the period of forcing. Alternately, for a fixed amplitude and varying period,

bifurcations occur as a transition from one region to another occurs. In other words, the region of $N : M$ phase-locked solutions are bounded by global bifurcations such as saddle node of periodic orbits or Neimark-Sacker bifurcations [4, 49, 77].

Besides self-sustained oscillations, damped oscillations are also found in nature. For example, cyanobacteria exhibit damped circadian oscillations if one of the key clock proteins is absent [48]. Entrainment of self-sustained oscillations is a well-studied problem [1,3,4,16,25,32,36,77,78,82,83,86,93]. Although the entrainment of damped oscillations has been less explored, there have been some experimental and theoretical studies on this topic. Experimental work shows the presence of damped oscillations in the circadian clock of insects [6]. In mammals, the central circadian clock (the suprachiasmatic nucleus, or SCN) is comprised of a heterogeneous cell population with a large proportion of cells that show weak (damped) oscillations [95]. In a theoretical work, Woller et al. studied a classic circadian oscillator model (the Goodwin model) and compared the entrainment properties when the unforced system shows either damped oscillations or limit cycle oscillations [99]. They found that the entrainment region is larger (entrainment is achieved over a wider range of forcing periods) when the unforced system exhibits damped oscillations. With periodic forcing applied to limit cycle oscillators, they found a richer set of behaviors, including non-entrained chaotic and quasiperiodic solutions, which are not desirable biologically. A modeling study by Westermark et al. investigated the effect of noise on damped oscillators [96]. They showed that noise can generate sustained oscillations in a damped oscillator. They compared their simulations to experimental data from individual cells, and concluded that whether the circadian clock is a damped or self-sustained oscillator at the single-cell level could not be determined.

Further work by Gonze et al. [34] considered synchronization of populations of coupled circadian oscillators. In their work, they showed that when the coupled oscillators being considered are damped, high synchronization efficiency is achieved.

Work by Bernard et al. [7] also shows that efficient and robust synchronization is achieved in coupled damped oscillators. In the context of coupled oscillations and synchronization. Komin et al. [52] studied entrainment of coupled oscillators where each oscillator has a different intrinsic period. They found that cells having damped oscillators are entrained more efficiently to external forcing than cells with sustained oscillations with different intrinsic periods.

Based on the above interesting results on entrainment of different types of oscillators, this thesis explore the entrainment of self-sustained oscillators, damped oscillators, and non-oscillators. Their entrainment properties, in particular the structure of Arnold tongues, are then compared.

1.3 Structure of the Dissertation

In the first half of the thesis (Chapters 2 and 3), we examine autonomous and non-autonomous neuronal models. The second half of the thesis (Chapters 4 and 5) examines autonomous and non-autonomous circadian clock models. In each half of thesis, the goal is twofold. First, dynamical system tools are used to understand the mechanisms of oscillations. Second, using the considered biological models, entrainment properties are explored with the unforced systems in different qualitative regimes.

In Chapter 2, we consider the Fitzhugh-Nagumo (FHN) model of neuronal excitability. The FHN model is a planar mathematical model which captures the spiking behavior observed in the Hodgkin-Huxley model [41]. Since the FHN model is two-dimensional, it gives us a great advantage to analyze how the different qualitative behaviors are produced as a control parameter is varied using the phase-plane techniques. The autonomous FHN model is examined in this chapter by varying the systems parameters. Dynamical systems tools like phase-plane analysis and bifurcation diagrams are used to gain insight into the systems behaviour.

Understanding the different dynamics that arise for the autonomous FHN model gives us a good platform for the subsequent chapter in which the external periodic forcing comes into play.

In Chapter 3, we examine the FHN model under square-wave periodic forcing which represents an abrupt change in the system. The advantage of using square-wave forcing is that the system can be decomposed into two-dimensional subsystems with constant forcing, which are autonomous systems and hence easier to analyze. We investigate entrainment properties for the different dynamical regimes of the FHN model described in Chapter 2. We refer to Arnold tongues with single and multiple 1:1 entrainment regions as *monoglot* and *polyglot* entrainment responses, respectively. The mechanisms underlying monoglot versus polyglot entrainment are explained using phase-plane diagrams. We also explore entrainment responses for other parameter regimes of the FHN model by changing the amount of time scale separation (ϵ), the slope of the $w-$nullcline (α), and using sine-wave periodic forcing.

In Chapter 4, we study post-translational oscillations (PTO) in two circadian clock models: the Rust [81] and Byrne [12] models. The Rust model is a three-dimensional mathematical model for circadian oscillations in cyanobacteria. The circadian clock of cyanobacteria is relatively simple and easy to manipulate [15, 54]. Although transcriptional and translational feedback is an essential mechanism in the circadian clock of eukaryotes, in vitro experiments show that the circadian clock of cyanobacteria does not require this type of feedback. This enables the reconstitution of the core oscillator in a test tube with just three proteins (KaiA, KaiB, and KaiC), ATP, and magnesium [69]. On the other hand, the Byrne model is two-dimensional and represents circadian PTO for a generic protein with two regulatory sites. Both circadian models considered in this chapter are continuous time and non-smooth as the phase space is partitioned into regions with different vector fields. We call these regions linear and nonlinear regions as their associated differential equations

are linear and nonlinear, respectively. These regions are separated by a switching manifold which is a plane in the Rust model and a curve in the Byrne model. For these models, we perform dynamical systems analysis to understand the mechanisms of intrinsic circadian oscillations and explore the similarities and differences in their qualitative behaviors.

In Chapter 5, we analyze entrainment properties in the Rust and Byrne models. We use square-wave periodic forcing to represent the light-dark cycles. We use dynamical system tools (fixed points analysis in linear and nonlinear regions when forcing turns off and on) and study how forcing affects the system's dynamics. Similar to Chapter 3, we also investigate the existence of polyglot entrainment responses.

In Chapter 6, we analyze entrainment properties for some other neuronal, circadian, and glycolytic oscillations. We conclude that polyglot entrainment structure (multiple 1:1 regions) is observed when the unforced system is in the vicinity of a Hopf bifurcation and the Hopf point is located near a knee of a cubic nullcline.

In Chapter 7, implications and extension of polyglot entrainment to the network of coupled oscillators are proposed as future work.

CHAPTER 2

FITZHUGH-NAGUMO MODEL

2.1 Introduction

In neuronal physiology, an action potential is a rapid change in membrane potential of a neuron [41]. Such rapid changes are called depolarization, repolarization and hyperpolarization and these changes are the result of the opening and closing of different ion channels. An action potential travels down the axonal compartment of a neuron. Through action potentials, neuron communicate with each others [30, 37]. The temporal sequence of action potentials is called spike trains. How action potentials (or spikes) are generated are described by a prototype mathematical model called the HodgkinHuxley model [41]. Hodgkin-Huxley is a system of four non-linear differential equations. With Hodgkin-Huxley being a more biophysically and realistic model which describes the initiation and generation of spiking mechanism, a full model is very complicated and the visual interpretation of how system's trajectory evolve is not possible. To capture most of the Hodgkin-Huxley model qualitative dynamics like excitability and spiking mechanism, FitzHugh and Nagumo [68] developed a two dimensional phenomenological model called FitzHugh-Nagumo model. Being relatively simple model with only two equations and fewer parameters, geometric and visual explanation of neuronal excitability and spiking is possible.

2.2 FitzHugh-Nagumo Model Equations

The FitzHugh-Nagumo (FHN) is a mathematical model of neuronal oscillations developed independently by FitzHugh [28, 29] and Nagumo [68]. As it is a two-dimensional model, it allows us to study neuronal oscillations geometrically phase plane analysis. We use the following notation for the model of FHN type [29] used in [79]

$$\frac{dv}{dt} = f(v) - w = F(v, w), \tag{2.1}$$

$$\frac{dw}{dt} = \epsilon(\alpha v - \lambda - w) = G(v, w). \tag{2.2}$$

where v and w are dimensionless state variables representing the membrane potential and the recovery variable, respectively. The function $f(v) = -2v^3 + 3v^2$ is a cubic whose minimum and maximum occur at $(0, 0)$ and $(1, 1)$, respectively. The parameter ϵ represents the time scale separation between the two dependent variables, the parameter α denotes the slope of the w-nullcline (N_w) and the parameter λ denotes the displacement of the w-nullcline with respect to the v-nullcline (N_v). These nullclines are given by

$$N_v = f(v), \tag{2.3}$$

$$N_w = \alpha v - \lambda. \tag{2.4}$$

The Jacobian matrix evaluated at fixed point $(\hat{v}, \hat{w})$ becomes:

$$J = \begin{bmatrix} F_v & F_w \\ G_v & G_w \end{bmatrix} \tag{2.5}$$

$$= \begin{bmatrix} 6\hat{v^2} + 6\hat{v} & -1 \\ \epsilon\alpha & -\epsilon \end{bmatrix}. \tag{2.6}$$

The intersection of the v-nullcline and w-nullcline gives the fixed point (equilibrium point). The location of fixed point change as we vary parameters λ and α. The stability properties of the fixed point depend upon the parameters α, ϵ, and not λ (Jacobian depends upon α and ϵ). In the next sections, we discuss the dynamics of the the FHN model by changing λ, α, and ϵ.

2.3 Varying the Parameter λ

In the context of neuroscience, the parameter λ captures the effect of a constant input current to the system which can produces different qualitative behaviour similar to the Hodgkin-Huxley model [41] like excitable state, resting state and spiking state. Input currents affect the (first) equation for v. However, because the dependence on w is linear, a change of variables brings this input current to the equation for w. As discussed before that the location of fixed points change as we vary λ. In this section, for fixed α and ϵ, we categorize different types of fixed points by varying λ. Classification of different types of fixed points have been given in the Table 2.1. For $\epsilon = 0.01$ and various α values, we have different types of fixed points. For $\alpha = 2$, by varying λ, evolution of the trajectory in the phase plane and time course are shown in the Figure 2.1.

If $\lambda < 0.11$, the fixed point is a stable node located on the left branch of the cubic v-nullcine. For such type of fixed points, both eigenvalues are real and negative. Trajectory starting from an initial point converges to the fixed point as shown in the Figure 2.1 A1.

If $\lambda \in [-0.11, 0.0033)$, the fixed point is a stable focus located in the vicinity of the lower knee of the cubic v-nullcline. For such fixed points, both eigenvalues are complex conjugate with real parts negative. Trajectory evolving around stable focus type fixed points has damping behaviour. As the real part of the eigenvalues decreases in magnitude, damping increases, which means it takes a longer time for the

Table 2.1 Classification of Fixed Points by Varying λ with $\alpha = 2$ (First and Second column), $\alpha = 4$ (Third and Fourth column), and $\epsilon = 0.01$

Parameter range	Fixed point type	Parameter range	Fixed point type
$\lambda < -0.11$	Stable node	$\lambda < -0.265$	Stable node
$\lambda \in [-0.11, 0.0033)$	Stable focus	$\lambda \in [-0.265, 0.0067)$	Stable focus
$\lambda \in (0.0033, 0.089)$	Unstable focus	$\lambda \in (0.0067, 0.266)$	Unstable focus
$\lambda \in [0.089, 0.91)$	Unstable node	$\lambda \in [0.266, 2.73)$	Unstable node
$\lambda \in [0.91, 0.9967)$	Unstable focus	$\lambda \in [2.73, 2.99)$	Unstable focus
$\lambda \in [0.9967, 1.098]$	Stable focus	$\lambda \in [2.99, 3.265]$	Stable focus
$\lambda > 1.098$	Stable node	$\lambda > 3.265$	Stable node

trajectory to approach towards the fixed point. A representative example of stable focus has been shown in the Figure 2.1 A2.

Figure 2.1 A3 and A4 shows the canard phenomenon. The canard phenomenon [20,21,23,26,55,79] refers to a very fast transition from small amplitude oscillations to large amplitude amplitude relaxation oscillations upon varying a parameter (in this case λ). Canard phenomenon occurs with in very small range of a parameter. For $\alpha = 2$, the small amplitude oscillations are unstable and large amplitude oscillations are stable. For $\alpha = 4$, the small amplitude oscillations and large amplitude oscillations are both stable. Due to the symmetry of the cubic, canard phenomenon also occurs in the vicinity of the upper knee of the cubic v-nullcline (not shown here).

For $\lambda \in (0.0033, 0.089)$, the fixed point is an unstable focus located in the vicinity of the lower knee of the cubic v-nullcline. Both eigenvalues are complex conjugates with their corresponding real parts positive. In this case, we have sustained oscillations. The trajectory evolving in the vicinity of an unstable fixed point shows

some damping and then converge toward the limit cycle oscillations as shown in the Figure 2.1 A5.

For $\lambda \in (0.089, 0.91)$, the fixed point is an unstable node. The unstable node covers most of the middle branch of the cubic nullcline. Both eigenvalues are real and positive. In this case, we also have sustained oscillations. The trajectory starting in the vicinity of an unstable node converges toward the limit cycle oscillations without any damping as shown in the Figure 2.1 A6.

Due to the symmetry of the cubic, we have a similar structure for the fixed points in the region of unstable nodes. Particularly, to the left and right of the region of unstable node type fixed points, different fixed points are located in the same pattern.

If $\lambda \in (0.91, 0.9967)$, the fixed point is a unstable focus located in the vicinity of the upper knee of the cubic v-nullcline. For such fixed points, both eigenvalues are complex conjugates with real parts positive. The trajectory starting in the vicinity of an unstable focus shows some damping and then converge toward the limit cycle oscillations (not shown).

If $\lambda \in [0.9967, 1.098)$, the fixed point is a stable focus located in the vicinity of the upper knee of the cubic v-nullcline. The trajectory evolving around stable focus type fixed points has damping behaviour.

If $\lambda > 1.098$, the fixed point is a stable node located on the right branch of the cubic v-nullcline. The trajectory starting from an initial point converges to the fixed point.

We have a similar structure for the location and stability of the fixed points for $\alpha = 4$ shown in the Table 2.1. By increasing α, the difference we observed is that the range of λ values for focus and unstable node increases.

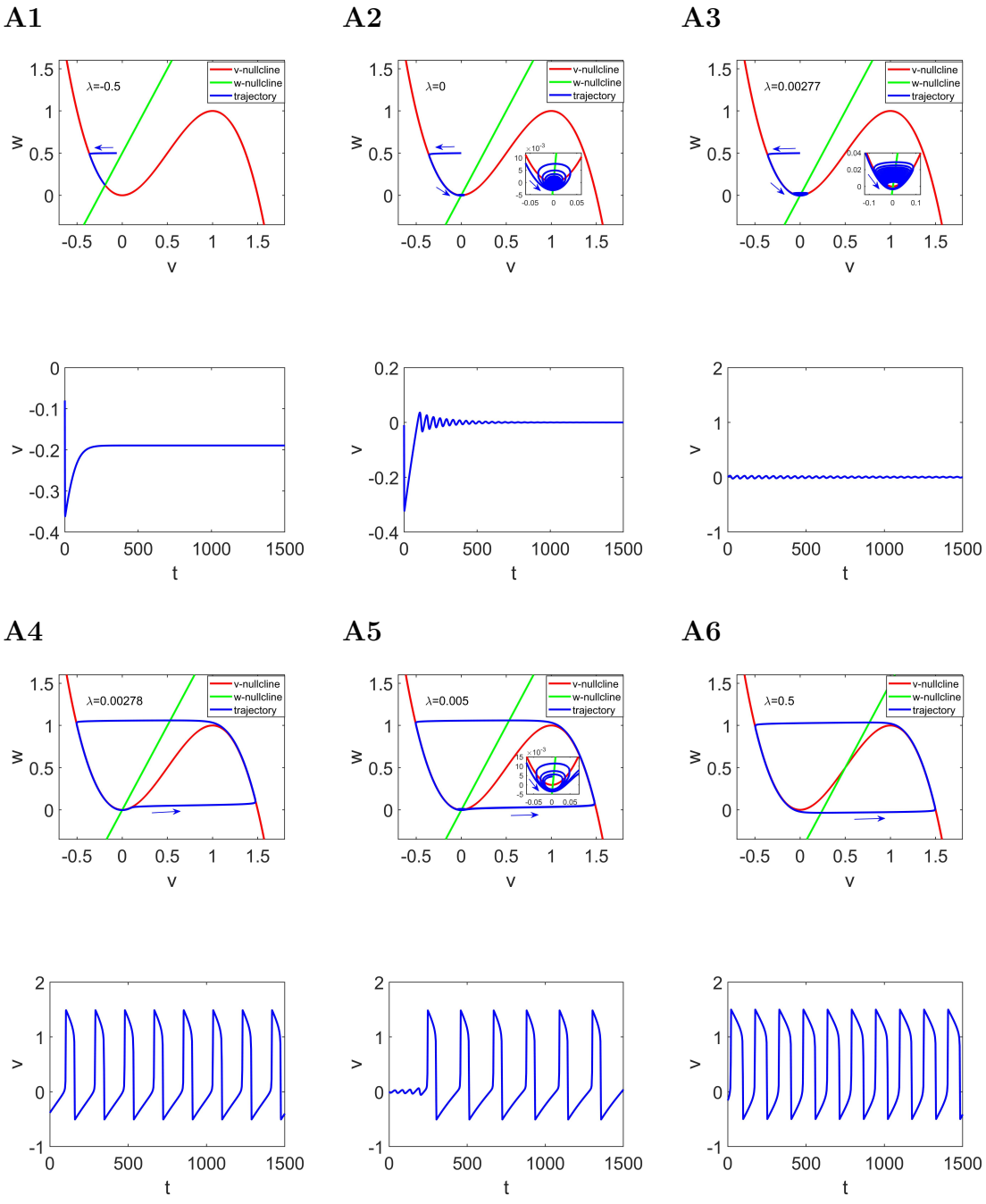

Figure 2.1 Representative phase-plane diagrams and v time course dynamics for the FHN model by varying λ. **A1.** $\lambda = -0.5$. Fixed point is a stable node. **A2.** $\lambda = 0$. Fixed point is a stable focus. **A3 and A4.** $\lambda = 0.00277$ and $\lambda = 0.00278$. Canard phenomenon. **A5.** $\lambda = 0.05$. Fixed point is an unstable focus. **A6.** $\lambda = 0.5$. Fixed point is an unstable node. We used the following parameter values: $\alpha = 2$, $\epsilon = 0.01$.

2.4 Varying the Parameter α

For $\epsilon = 0.01$, varying α gives different bifurcation structures, as shown in the Figure 2.2. For $\alpha = 2$, we have two subcritical Hopf bifurcations. The first Hopf point is located at $\lambda_{H_1} = 0.0033$. Small amplitude unstable limit cycle oscillations emerged at λ_{H_1}. These small amplitude oscillations give rapid transition to the large amplitude oscillations at the left canard point which is located a $\lambda_{c_1} = 0.00277$. The second Hopf point is located at $\lambda_{H_2} = 0.9967$. Due to the symmetry of the cubic, we also have second canard point located at $\lambda_{c_2} = 0.9972$. Between λ_{c_1} and λ_{H_1} is the region of bistability for which large amplitude oscillations and the stable focus attractor coexist (Figure 2.3). Due to symmetry, we also have bistability between λ_{H_2} and λ_{c_2} (not shown).

For $\alpha = 4$, we have two supercritical Hopf bifurcations. The first Hopf point is located at $\lambda_{H_3} = 0.0067$. Small amplitude stable limit cycle oscillations emerged at λ_{H_1}. These small amplitude oscillations explode and becomes large amplitude oscillations as λ crosses the left canard point. The left canard point is located $\lambda_{c_3} = 0.0078$. The second Hopf and canard points are located at $\lambda_{H_4} = 2.993$ and $\lambda_{c_4} = 2.992$, respectively.

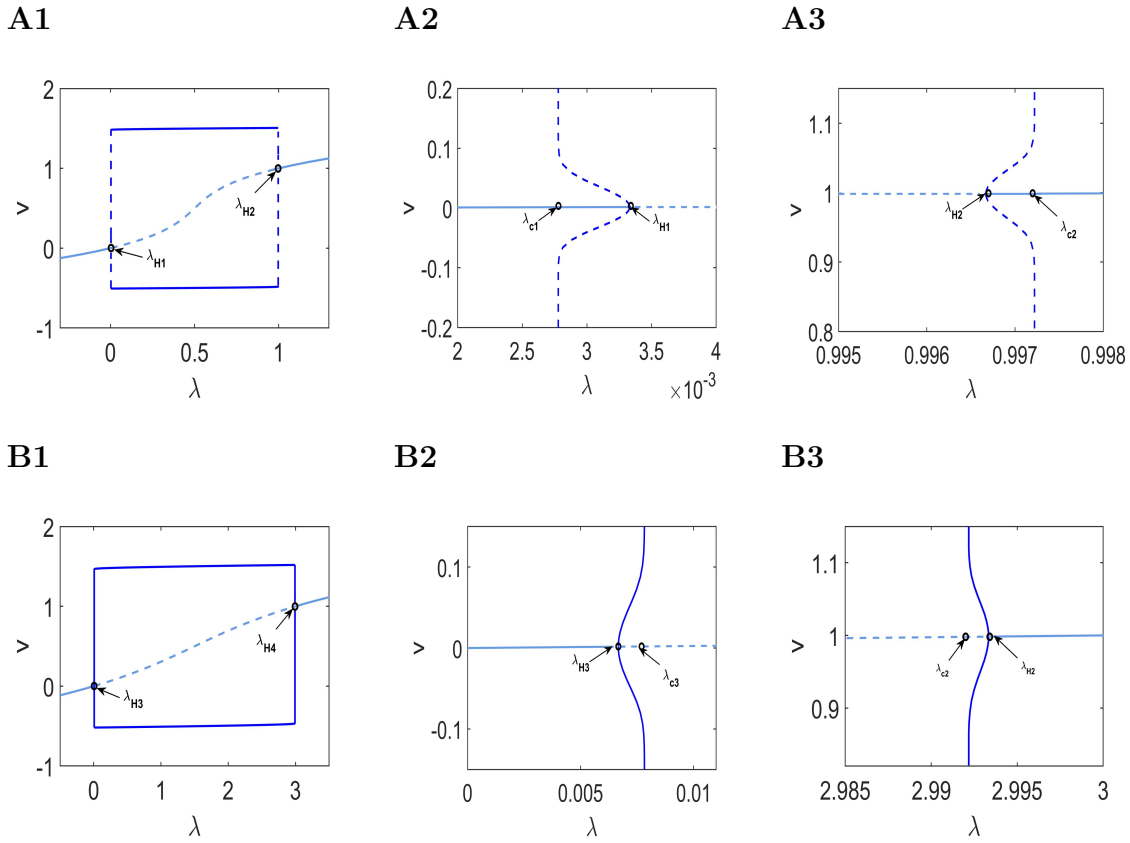

Figure 2.2 Bifurcation diagrams as a function of parameter λ. **A1.** For $\alpha = 2$, we have two Hopf bifurcations. **A2. and A3.** are the magnifications of **A1.** around λ_{H1} and λ_{H2}, respectively. This shows that both bifurcations are subcritical as unstable limit cycle emerge from Hopf points. **B1.** For $\alpha = 4$, we also have two Hopf bifurcations. **B2. and B3.** are the magnifications of **B1.** around λ_{H3} and λ_{H4}, respectively. This shows that both are supercritical as stable limit cycle emerge from Hopf points. Magnified panels also shows the λ values at which canard phenomenon occurs. For both panels, $\epsilon = 0.01$.

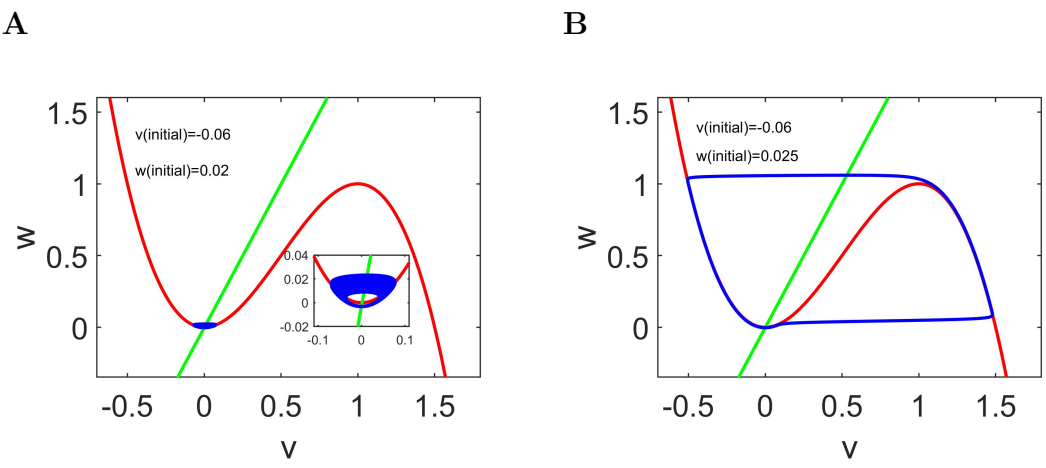

Figure 2.3 Representative phase planes showing bistabilty for fixed parameter values and changing initial values of the state variables. Two stable steady states coexist for different initial conditions. We have stable focus attractor for initial values of state variables (**A**) and stable limit cycle attractor for another initial condition (**B**). We used the following parameter values: $\alpha = 2$, $\lambda = 0.0028$, $\epsilon = 0.01$.

2.5 Varying the Parameter ϵ

In this section, we discuss the effects of the parameter ϵ on the system's trajectory. For small ϵ, the variables v and w evolve on fast and slow time scales, respectively. We refer to v as fast variable and w as slow variable. The cubic v-nullcline have three branches. The left and right branches are slow and attracting which means for small ϵ, the trajectory evolves slowly along these branches whose direction is determined by the sign of $\frac{dw}{dt}$. The middle branch is a repelling branch as the trajectory moves faster as it crosses the lower knee to the right or crosses the upper knee to the left. For small ϵ, the oscillations created are called relaxation as the trajectory exhibit abrupt changes as it crosses the lower knee or upper knee of the cubic (Figure 2.4 A). For small ϵ, the $\frac{dv}{dt}$ versus v shows the speed of the trajectory as it travels across the phase plane. In the speed plot (Figure 2.4 A right panel), we see non-uniform changes as the trajectory crosses the lower knee (upper knee) and moves to the right

branch (left branch) of the cubic. For higher ϵ values, oscillations almost behaves like harmonic oscillations and the slow-fast time scales disappears (Figure 2.4 B and C).

Another qualitative change we have for varying epsilon is that for small ϵ values, the region of fixed points lying on the middle branch of the cubic is unstable as shown in the shaded region(Figure 2.4 A). As ϵ increases, the shaded region of the unstable fixed points decreases and as a result the oscillations are of small amplitude. More specifically, the region of stable focus increases and the region of unstable fixed points decrease by increasing ϵ.

For small ϵ values, we have subcritical and supercritical Hopf bifurcations. For higher ϵ values, we only have supercritical Hopf bifurcation.

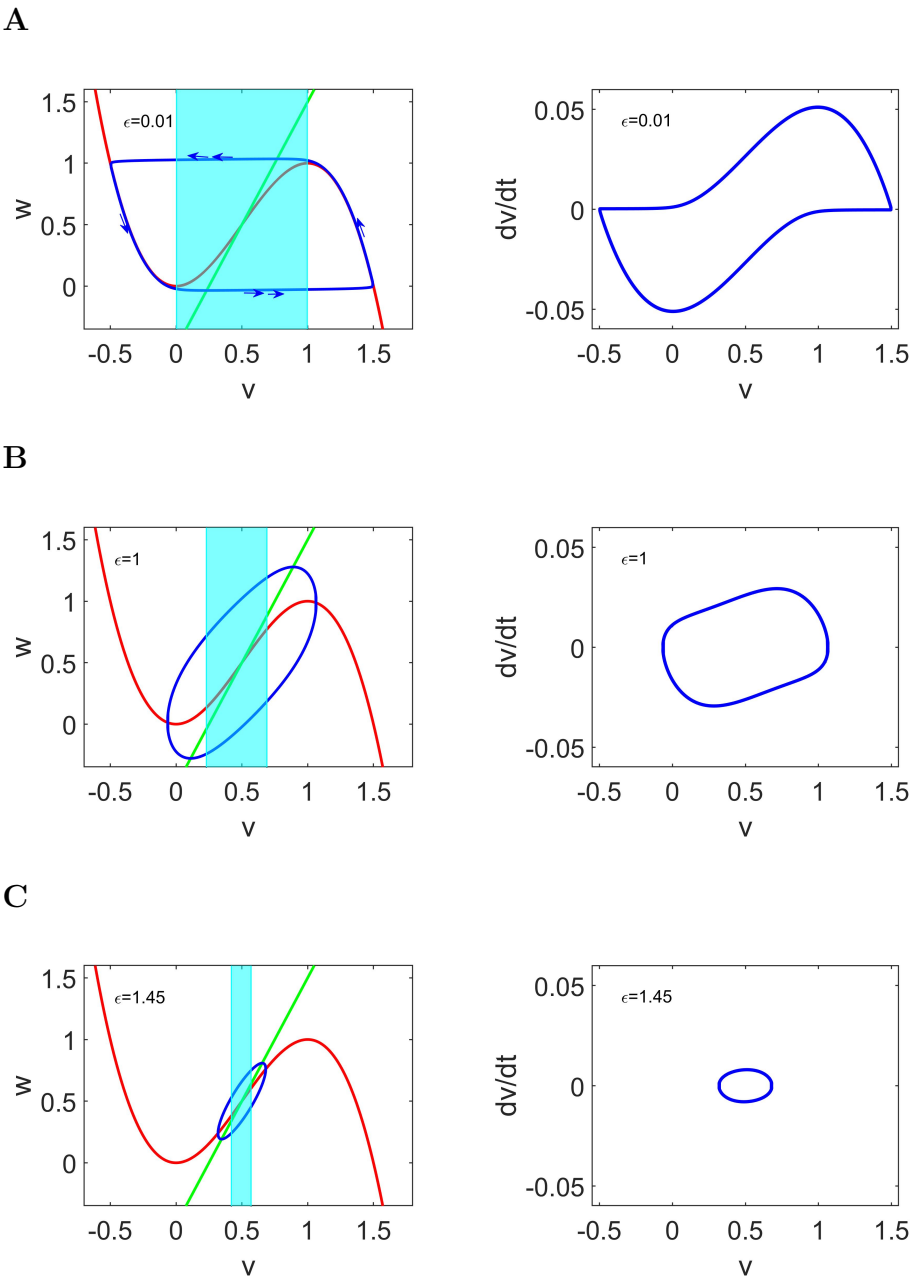

Figure 2.4 Representative phase-plane diagrams (left panel) and speed plots (right panel) for the FHN model by varying ϵ. We used the following parameter values: $\alpha = 2$, $\lambda = 0.5$.

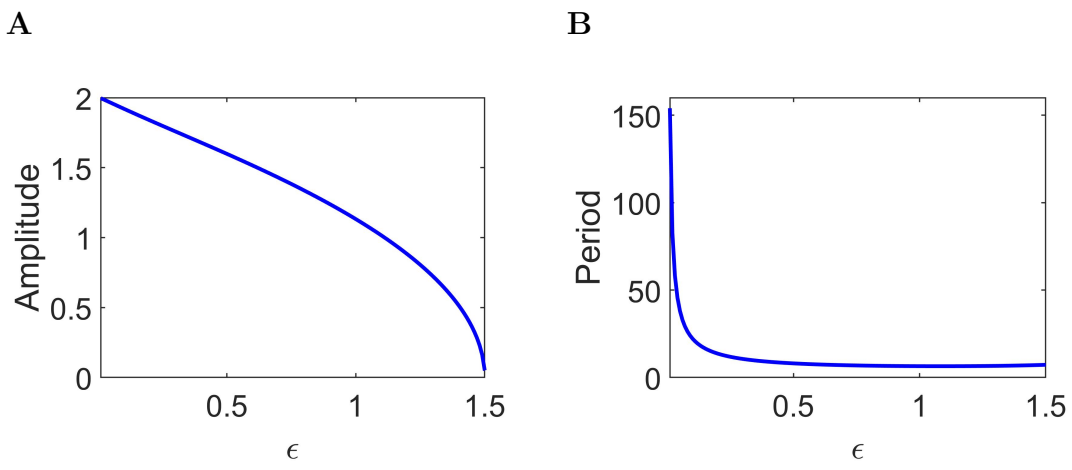

Figure 2.5 Amplitude (**A**) and period (**B**) of the self-sustained oscillations in the FHN model by varying ϵ. We used the following parameter values: $\alpha = 2$, $\lambda = 0.5$.

The amplitude and period of limit cycle oscillations also change as we increase ϵ (Figure 2.5). For small ϵ, we know that the trajectory touches the right and left branches of the cubic nullcline and as a result we the amplitude is larger for small ϵ. For small ϵ, the period of oscillations is larger, as the trajectory spends most of the time on the left and right branches (slow manifolds) of the cubic. As ϵ increases, the trajectory starts crossing the middle branch and does not go far right or left of the cubic. As a result, the amplitude decreases. As the slow-fast nature of the trajectory decreases as ϵ increases, the period also decreases.

CHAPTER 3

ENTRAINMENT RESPONSES IN FHN MODEL

3.1 Introduction

In Chapter 2, for an unforced FHN model, by varying different control parameters, we have observed different qualitative behaviors from non-oscillatory to oscillatory solutions, the slow-fast nature of the limit cycle trajectories and different bifurcation structures. In this Chapter, we explore the entrainment properties when an unforced system has self-sustained oscillation, damped oscillations or non-oscillatory solutions. In Section 3.2, we describe the type of periodic forcing we are considering and the way it is applied to the FHN model. Entrainment properties are described in terms of showing Arnold tongues. The methods we used to compute the Arnold tongues is discussed in Section 3.2. The different types of entrainment responses are shown in Section 3.3.

3.2 Methods

3.2.1 Periodically Forced FHN

We use the following periodically forced model of FHN type [29] used previously in [79]

$$\frac{dv}{dt} = f(v) - w + A\,F(t), \tag{3.1}$$

$$\frac{dw}{dt} = \epsilon(\alpha v - \lambda - w), \tag{3.2}$$

where v and w are dimensionless variables representing the membrane potential and the recovery variable, respectively. The function $f(v) = -2v^3 + 3v^2$ is cubic

with the minimum and maximum occurring at $(0, 0)$ and $(1, 1)$, respectively. The parameters ϵ, α and λ represent the time scale separation between the two dependent variables, the slope of the w-nullcline, and the displacement of the w-nullcline with respect to the v-nullcline. The last term in Equation (3.1) is a time-dependent, periodic input with a constant amplitude A. We use two different types of waveforms for $F(t)$: square-wave and sinusoidal, with period T, duty cycle 50%, and minima and maxima equal to $F = 0$ and $F = 1$, respectively. We refer to the time intervals where $F > 0.5$ as the "on" state and $F < 0.5$ as the "off" state.

One advantage of using a square-wave forcing is that one can decompose the periodically driven system into two autonomous systems, one in the first case with the forcing turned off and in the other case with the forcing turned on. In the latter case, a change of variables $W = w - A$ allows us to move the constant forcing term A into the second equation, yielding

$$\frac{dv}{dt} = f(v) - W, \tag{3.3}$$

$$\frac{dW}{dt} = \epsilon[\alpha v - (\lambda + A) - W]. \tag{3.4}$$

When the forcing is on, the forcing amplitude contributes to the displacement of the W-nullcline. Alternatively, without the change of variables, A causes the v-nullcline to displace abruptly between the two regimes. For sinusoidal inputs, this displacement is continuous and gradual.

3.2.2 Computation of Arnold Tongues and Numerical Simulations

Arnold tongue is a two dimensional bifurcation diagram in parameter space which shows different frequency locking modes in response to periodic forcing [38, 77]. Outside the Arnold tongues, the input and output are not synchronized. Here we

focus on investigating 1:1 entrainment. For the Arnold tongues we use here, the horizontal axis corresponds to the forcing period T and the vertical axis corresponds to the forcing amplitude A. Typically, by increasing the forcing amplitude, the Arnold tongue widens, indicating that entrainment can occur for a larger range of periods [71, 77].

In order to numerically compute the Arnold tongues, for each fixed value of A,we found the minimum and maximum values of T for which the system exhibits 1:1 entrainment. 1:1 entrainment has been determined on the basis of matching of period of the forcing (T) and period of the system (T_s). If $|T - T_s| < 0.001$, then we have 1:1 entrainment. To compute T_s, we are using MATLAB *findpeaks* with its feature *MinPeakProminence* to set a threshold for admissible peaks.

Numerical simulations were carried out using the modified Euler method [11] (a Runge-Kutta method of order 2) with a time step $\Delta t = 0.05$ in MATLAB (The Mathworks, Natick, MA). Bifurcation diagrams were computed using the AUTO feature of XPPAUT [24] and plotted in MATLAB.

3.3 Results

In this part we want to discover the main reason for having 1:1 polyglot entrainment. In other words, we want to clarify if the emergence of 1:1 polyglot structure is due to the birth of the second 1:1 region in the Arnold tongue or whether it is actually due to the death of some parts of the first 1:1 tongue?

Based on the intersection point of the w nullcline with the v nullcline, we have different types of fixed point which effect the dynamics of the system. This intersection point changes depending on varying λ and α values. By changing the λ value, we can move w nullcline to the right or to the left, where changing the α value changes the slope of the w nullcline, which in turn effects the intersection point to the right or to the left if the slope getting steeper or shallower.

According to these changes, we have different types of fixed points for the system: **stable node**, **stable focus**, **unstable focus** and **unstable node**. For the forced system, besides λ and α, the amplitude of the forcing (A) also plays a role in defining the type of fixed point. The change in amplitude for the forced system behaves like changing the λ value for the unforced system. This means moving the w-nullcline to the right (increasing the λ value) for the unforced system is analogous to increasing the amplitude (A) for the forced system.

In the following parts, we are going to restrict our focus only on $\alpha = 2$ for which we have subcritical Hopf bifurcation by varying λ and $\alpha = 4$ for which we have supercritical Hopf bifurcation by varying λ and we analyze the entrainment results based on these different λ values. We split the λ axis based on a fact that we have monoglot entrainment (single 1:1 region in the Arnold Tongue) or polyglot entrainment (multiple 1:1 region in the Arnold Tongue).

We then consider periodic forcing with different frequencies and two types of waveforms, sinusoidal and square-wave, which are representative of gradual and abrupt transitions, respectively, between the up and down states. Both are amenable to analysis using dynamical systems tools. In the latter case, the dynamics of the periodically forced system can be decomposed into two two-dimensional subsystems with constant forcing, which simplifies the analysis. We call the times at which the forcing turns on and off the *switching times*, and the corresponding points in the phase-plane diagrams the *switching points*. Switching points serve as initial conditions at the transitions between the on and off states of the forcing (when 1:1 entrainment occurs, the switching points always stay fixed).

3.3.1 Monoglot Entrainment Responses

Here we consider the FHN model with $\alpha = 2$ and $\epsilon = 0.01$ and representative values of λ using a square-wave input with amplitude A (50 % duty cycle). Figure 3.1 shows

representative phase-plane diagrams (arranged in the order in which they will be used in the following sections). As λ increases (panels B1, C1, D1, A1), the w-nullcline moves to the right and the fixed point transitions from a stable node (away from the knee of the v-nullcline, on the left, not shown); to a stable focus (Figure 3.1 B1 and C1); to an unstable focus (Figure 3.1 D1 and A1); to an unstable node (away from the knee of the v-nullcline, on the right, not shown). The stable focus in Figure 3.1 B1 is located close to the boundary between stable foci and nodes (further away from the knee of the v-nullcline than in Figure 3.1 A1) and therefore it exhibits strongly damped oscillations, but not sustained oscillations.

The effect of periodic forcing by positive square-wave inputs (with amplitude A) can be thought of as the abrupt transition between two autonomous FHN systems, one with $A = 0$ (forcing "turned off") and the other with a nonzero value of A (forcing "turned on"). We refer the latter as the tonically forced FHN system. In the absence of time-dependent forcing, increasing constant values of A has the same effect as increasing values of λ (i.e., increasing the constant forcing A is equivalent to increasing λ via a translation of the variable w). Therefore, as A increases, the fixed-point moves to the right and its stability properties change accordingly. If the unforced FHN model exhibits large amplitude oscillations (LAOs) for $A = 0$, then it will do so for $A > 0$ as well (e.g., Figure 3.1 A2 and D2). If the unforced FHN exhibits small amplitude (damped) oscillations (SAOs), then the tonically forced FHN model may exhibit SAOs with a weaker damping (e.g., the transition from Figure 3.1 B1 and C1) or LAOs (e.g., Figure 3.1 B2 and C2). We consider the response of the FHN model to periodic forcing in these three scenarios below. Finally, if the unforced FHN model has a stable node, then the tonically forced FHN model may have a stable node, exhibit SAOs or LAOs. We note that the existence of LAOs does not preclude the existence of damped SAOs for the small bistability range of values of λ.

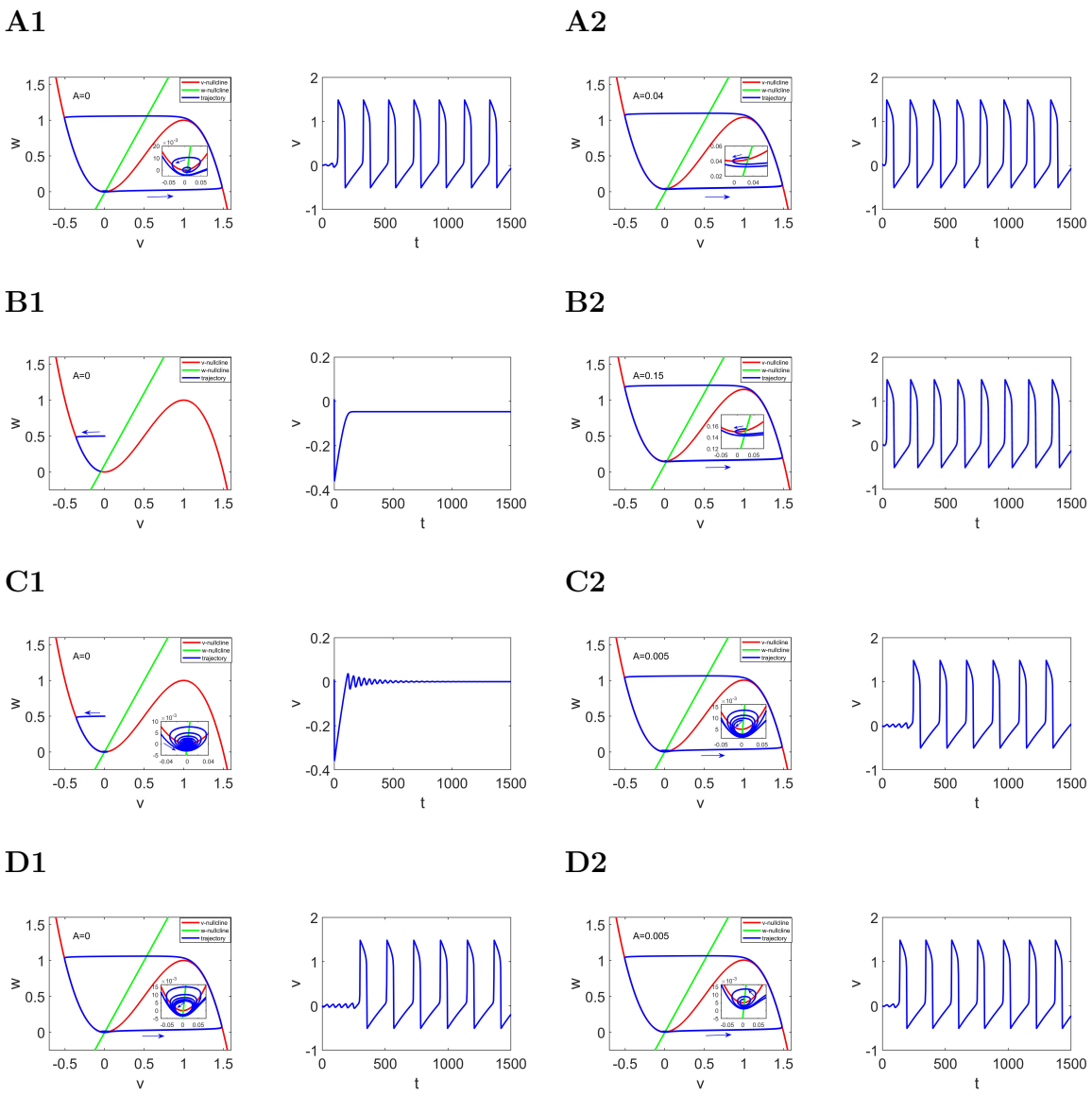

Figure 3.1 Representative phase-plane diagrams and v time course dynamics for the FHN model with constant forcing (A). **A.** $\lambda = 0.016$. The autonomous system ($A = 0$) shows intrinsic LAOs. **B.** $\lambda = -0.1$. The autonomous system ($A = 0$) has a stable focus. **C.** $\lambda = 0$. The autonomous system ($A = 0$) has a stable focus and shows damped oscillations (SAOs). **D.** $\lambda = 0.004$. The autonomous system ($A = 0$) shows intrinsic LAOs. The values of A are indicated in the graph. We used the following parameter values: $\alpha = 2$, $\epsilon = 0.01$.

Stable focus for an unforced system: entrainment of a strongly damped oscillator

Figure 3.1 B illustrates the behavior of the FHN model when the unforced system ($A = 0$) is a stable focus (with strongly damped SAOs) and the constantly forced system has an unstable focus (as in Figure 3.1 A2) and displays LAOs.

The entrainment of non-sustained oscillators has been significantly less studied than the entrainment of sustained oscillators. One important conceptual difference between the two protocols is the lack of a reference period in the cell that is being entrained. In the previous section, we argued that the entrainment can be understood as the abrupt transition between two oscillatory regimes and entrainment occurs when the time scales of the two regimes are compatible. Here, there is no oscillatory time scale associated to the unforced system. Furthermore, while the constantly forced system is able to show LAOs for large enough values of A (Figure 3.1 B2), for lower values of A the dynamics remains in a damped oscillatory regime without LAOs (not shown). Therefore, entrainment, when it occurs, cannot be explained simply in terms of time scale compatibility, but requires a deeper explanation in terms of dynamical systems ideas.

Figure 3.2 B1 and C1 show the 1:1 entrainment regions (green) for these two cases. Notably, they have a different shape than the standard Arnold tongues (e.g., Figure 3.2 A1). In particular, 1:1 entrainment is broken as A increases for constant values of T, but maintained as T increases for constant values of A below some critical value (dashed horizontal line). This critical value corresponds to the transition between two stability regimes for the constantly forced system: from unstable focus with LAOs (above, Figure 3.2 B1) to stable focus (below, Figure 3.2 C1).

A comparison between panels B3 and C3 of Figure 3.2 shows relatively similar patterns for the entrainment in the two regimes for the same oscillatory input. The

comparison between panels B4 and C4 of Figure 3.2 show the increased entrainment robustness as T increases in Figure 3.2 C4 is associated with the presence of MMOs in the forced system, reflecting the dynamic interaction between the forcing and the cell.

Stable node for an unforced system: entrainment of a non-oscillator The results for this scenario are similar to the entrainment results for a stable focus that is not in the vicinity of a Hopf bifurcation and are presented in the Appendix (Figure A.1). Another interesting feature of the stable node we observed is that, no matter how much we decrease λ, we still have a similar monoglot structure. Upon checking $\lambda = -1$, $\lambda = -5$ and $\lambda = -10$, we still see a similar structure.

The Breaking of 1:1 entrainment The 1:1 entrainment for the FHN model in the parameter regimes discussed above breaks in different ways depending on whether T is larger or smaller than its values in the 1:1 entrainment region, and whether the unforced system is in an LAO regime or a stable focus regime (Figure 3.2). In all cases, the N:M patterns have $N > M$ for smaller values of T and $N < M$ for larger values of T. In the first case, the breaking of 1:1 entrainment is due to a cycle skipping mechanism where the input turns off before the response (v) jumps up, and therefore the LAO fails to be generated. In the second case, the breaking of 1:1 entrainment is due to a cycle adding mechanism. In Figure 3.2 A3, in contrast to the previous case, v succeeds in jumping up in spite of the fact that the input turns off, indicating a more complex interaction of effective time scales and a seeming disconnect between the input and the response (e.g., v jumps down, while the input is up). In Figure 3.2 B3, the cycle adding mechanism results from the ability of the input to produce two output cycles per input cycle when it is on. Note that the inter-oscillations interval (IOI) is larger when the input is off than when it is on. None of these effects break 1:1 entrainment for larger values of T in Figure 3.2 C. In fact, Figure 3.2 C3 shows

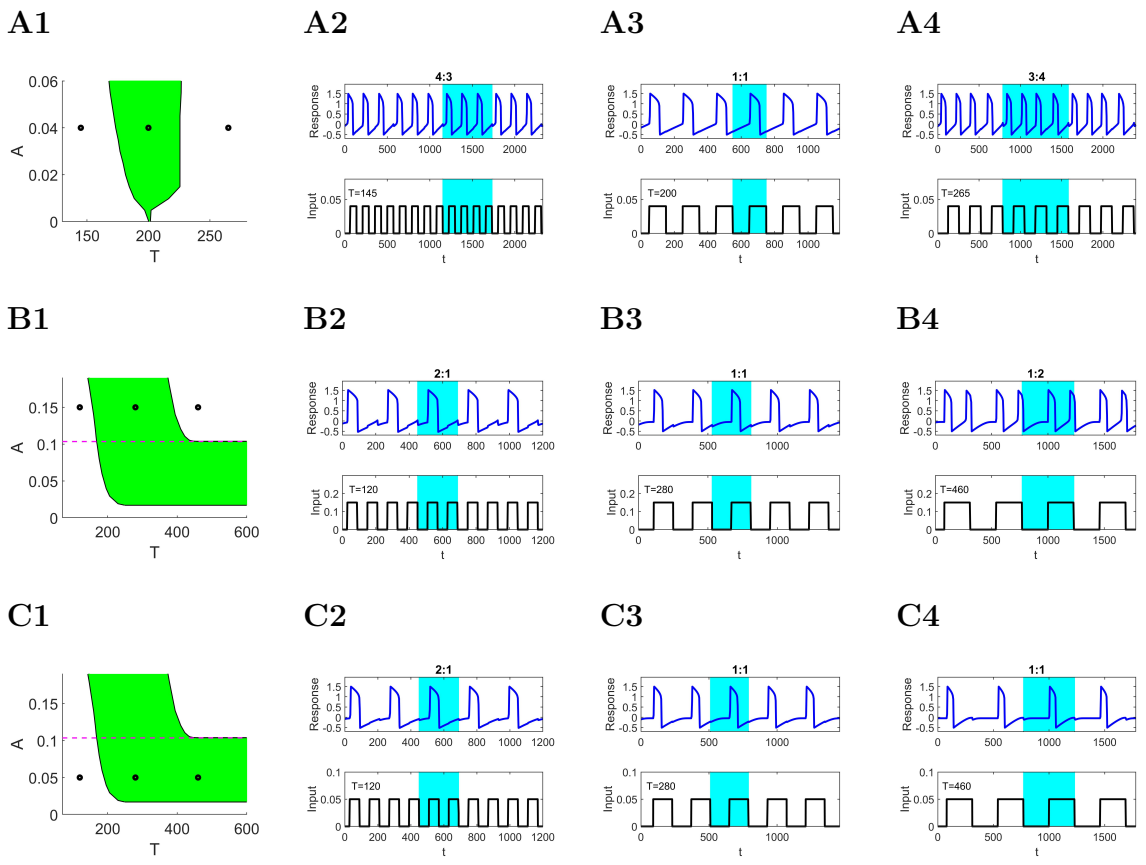

Figure 3.2 Representative entrainment patterns and Arnold tongues with monoglot structure in response to square-wave forcing. **A1, B1, & C1.** Arnold tongues showing 1:1 entrainment regions (highlighted in green). The dashed-magenta (horizontal) lines in panels B1 and C1 indicate the value of A for which the system with constant forcing A changes from a stable (below) to an unstable (above) focus. **Remaining panels.** Time courses for v and the forcing signal for the values of T and A indicated in A1, B1, and C1 (black markers). **A.** $\lambda = 0.016$ (Figure 3.1 A) and $A = 0.04$. **B.** $\lambda = -0.1$ (Figure 3.1 B) and $A = 0.15$. **C.** $\lambda = -0.1$ (Figure 3.1 B) and $A = 0.05$. We used the following parameter values: $\alpha = 2$, $\epsilon = 0.01$.

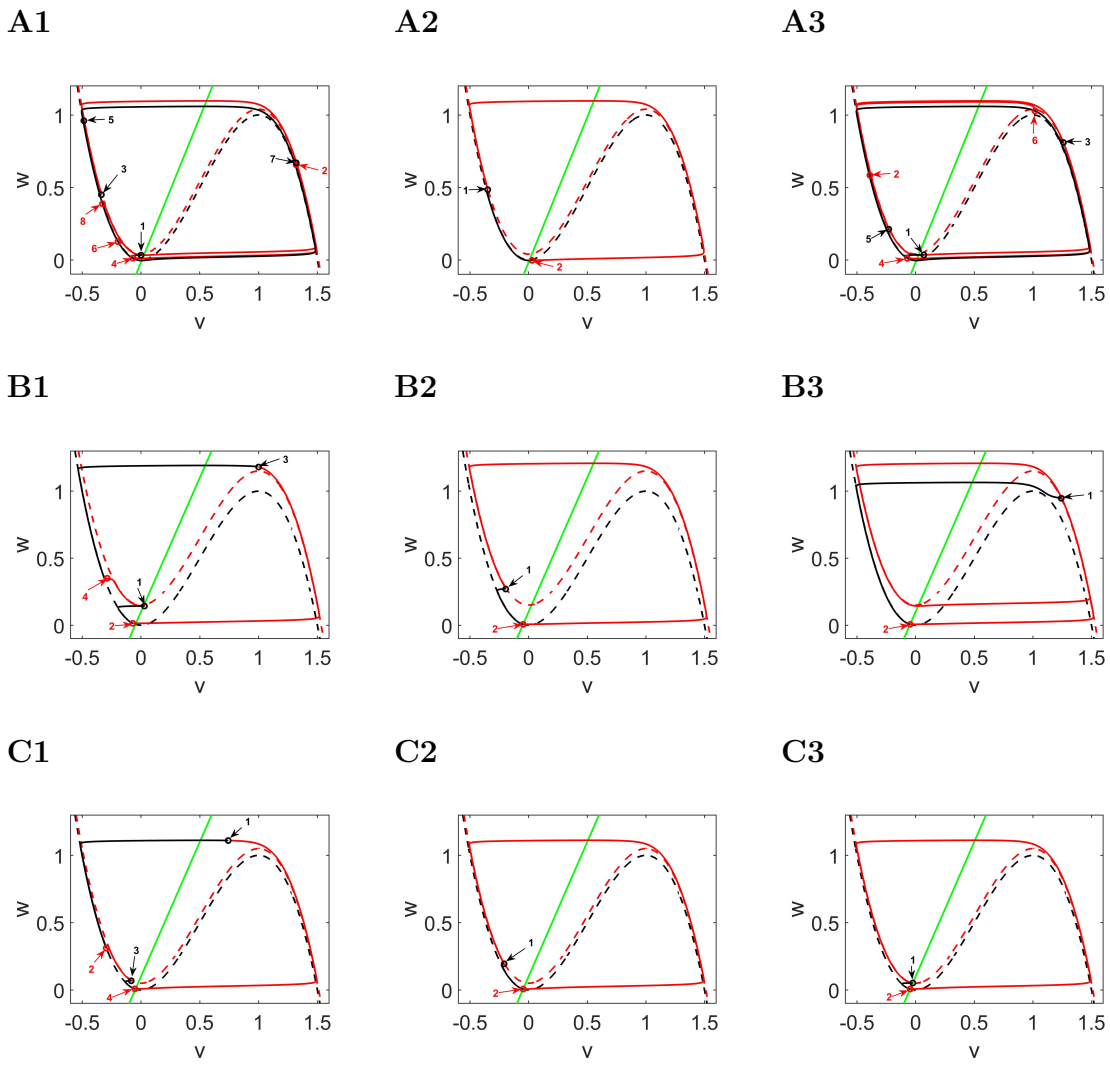

Figure 3.3 Phase-plane diagrams for the entrained responses shown in Figure 3.2 (square-wave input). The dashed curves are the v-nullclines for the unforced (black) and forced (red) systems, respectively. The green curve is the w-nullcline. The solid curves are the trajectories with the time intervals when the forcing is off and on shown in black and red, respectively. The numbers next to the arrows indicate the points in the phase-plane diagram at which the forcing turns off (black open circles) and on (red open circles). **A.** $\lambda = 0.016$ and $A = 0.04$ (Figure 3.2 A). **A1.** 4:3. **A2.** 1:1. **A3.** 3:4. **B.** $\lambda = -0.1$ and $A = 0.15$ (Figure 3.2 B). **B1.** 2:1. **B2.** 1:1. **B3.** 1:2. **C.** $\lambda = -0.1$ and $A = 0.05$ (Figure 3.2 C). **C1.** 2:1. **C2.** 1:1. **C3.** 1:1. We used the following parameter values: $\alpha = 2$, $\epsilon = 0.01$.

that 1:1 entrainment is maintained for values of T for which it is broken in the panels above as the result of v remaining roughly constant when the input turns off, instead of increasing as in all other panels.

Mechanisms of 1:1 entrainment and breaking of 1:1 entrainment Here we use dynamical systems tools (extended phase-plane analysis) to provide a more detailed explanation of the results discussed above. As we mentioned above, the dynamics of the forced system can be interpreted as the abrupt transition between two autonomous FHN systems, the off ($A = 0$) and on ($A > 0$) states. Dynamically, the evolution of the response trajectory is governed by an abrupt alternation between the phase-plane diagrams for the corresponding values of A. Figure 3.3 shows the superimposed phase-plane diagrams for $A = 0$ (black) and $A > 0$ (red). We use numbered arrows (in black and red) to denote the switching points between the unforced and forced systems.

Roughly speaking, the entrainability of the FHN system requires compatibility between its effective time scale and the time scale of the input (on phase). The former is primarily determined by the slow manifolds located in vicinities of the v-nullcline. In the unforced system ($A = 0$) the limit cycle trajectory evolves along these manifolds and jumps up and down towards the right and left branches of the v-nullcline, respectively, as time progresses (e.g. Figure 3.1 A). The interaction between the two time scales is interpreted as the v-nullcline rising and shifting down as the input turns on and off, respectively. This interaction process is affected by other factors, including the presence of fixed-points in one of the two regimes (e.g., Figure 3.1 B2 and B3) that may transiently create slower dynamics. In addition, the presence of nonlinearities may disrupt the evolution of the trajectory as the v-nullcline moves and may add additional time scales by creating small amplitude loops (SAOs), for example. These may favor or oppose the entrainability of the system. While oscillatory time scales

are usually associated with sustained oscillators, they are still present in damped oscillators and they become apparent and functional as they interact with the input. The presence of oscillatory time scales may also favor or oppose the entrainability of the FHN system.

Below we discuss a number of representative cases in detail, both to highlight the basic aspects of entrainability in the FHN system and to develop language for subsequent sections.

Mechanisms of 1:1 entrainment (Figure 3.3 A2, B2, C2, C3, corresponding to Figure 3.2 A3, B3, C3, C4, respectively).

When the forcing turns on (2), the v-nullcline raises and the trajectory, located further away from the lower knee, jumps up towards the right branch, moves up (slowly) along it, reaches the upper knee and jumps down towards the left branch. The trajectory then moves down (slowly) along the left branch until the forcing turns off (1). When this happens, the v-nullcline shifts down, affecting the direction of trajectory's motion. In Figure 3.3 A2, the trajectory is about halfway to the lower knee and is affected only slightly by the shift in the v-nullcline. In Figure 3.3 B2, the trajectory is affected significantly by the shift as it jumps to the left, and then moves down towards the lower knee at which point the forcing turns on (2). In Figure 3.3 C2, the size of the effect that the shift in the nullcline has on the trajectory is in between the two cases described above.

The dynamics in Figure 3.3 C3 is similar to those described above, except that the on-off transition of the forcing (1) occurs very close to the lower knee. The trajectory jumps to the left near the lower knee. Because of that, in contrast to the previous figures, the trajectory evolves on a much slower time scale than the ones at higher points of the slow manifold (in vicinities of the left branch). Therefore it does

not reach the lower knee while the forcing is off and only jumps up when the forcing turns on (2).

Breaking of 1:1 entrainment (Figure 3.3 B3, corresponding to Figure 3.2 B4).

When the forcing turns off (1), the v-nullcline shifts down and the trajectory is left closer to the upper knee, thus accelerating the jump down towards the left branch. The trajectory then evolves slowly along the left branch until it reaches the lower knee, at which point the forcing turns on (2). When this happens the v-nullcline raises. The trajectory evolves along the right branch, reaches the upper knee and jumps down. Because T is relatively large (and forcing relatively slow), the trajectory is able to jump up once more before the forcing turns off (1) and therefore can produce two LAOs per input cycle.

The very slow time scale operating in Figure 3.3 B3, where 1:1 entrainment is maintained, is due to the fact that the tonically forced system is in a stable focus regime. The switch to an unstable focus regime (for the tonically forced system) "destroys" this time scale and therefore the maintenance of 1:1 entrainment is no longer possible.

Breaking of 1:1 entrainment (Figure 3.3 A3, corresponding to Figure 3.2 A4). These dynamics are more complex than those for Figure 3.3 B3 since the first and third oscillations in the shadow region in Figure 3.2 A4 occur while the forcing is off. Starting from the beginning of the shadow region, when the forcing turns off (1) the v-nullcline shifts down, the trajectory jumps down, it moves slowly along the lower knee and jumps up towards the right branch creating an oscillation. This is induced by the forcing ceasing to be active rather than by the forcing turning on. A second oscillation is generated after the forcing turns on (2) and this oscillation

remains after the forcing turns off (3) since the trajectory needs to reach the upper knee in order for the oscillation to be terminated. In other words, the cell's intrinsic time scale dominates the forcing. The third oscillation is induced by the forcing (4). When the forcing turns off (5), the trajectory is very close to the lower knee, and therefore the trajectory jumps up well in advance of the forcing turning on (6). In fact, the trajectory is able to reach the upper knee when the forcing turns on and jumps down roughly when this happens.

Breaking of 1:1 entrainment (Figure 3.3 B1 and C1, corresponding to Figure 3.2 B2 and C2). The 2:1 patterns in both figures are generated by a cycle skipping mechanism. When the forcing turns on (2) the trajectory is approaching the stable focus. The v-nullcline raises and releases the trajectory that jumps up towards the right branch. The turning off of the forcing (3) roughly coincides with the passing of the trajectory of the upper knee. The trajectory jumps down towards the left branch (it would do so even in absence of the forcing remaining on, but the shifting down of the v-nullcline accelerates this process). The forcing turns on again (4) when the trajectory is evolving along the left branch. The ability of the cell in panel B1 to generate an oscillation in response to this process depends on the competition between two time scales that is determined by the slow manifold and the input period. Cycle skipping results because the forcing turns off (1) before the trajectory manages to pass through the lower knee and jump up. The trajectory then needs to wait for the forcing to turn on (2) in order to jump up. In the absence of the forcing the trajectory would converge to a stable focus. The dynamics in panel C1 is similar to those in panel B1, except the that the forcing turning off (1) does not prevent the trajectory from jumping up. Even if the forcing remained on the trajectory would not jump up, but converge to the stable focus. From that perspective, the successive forcing turning off (1) and on (2) are necessary to maintain the 2:1 pattern.

Breaking of 1:1 entrainment (Figure 3.3 A1, corresponding to Figure 3.2 A2). The mechanism of generation of 4:3 patterns is more complex than the ones for the 2:1 patterns described above, resulting from the fact that both the unforced and tonically forced systems are oscillators and have intrinsic oscillatory time scales that operate independently of the input. The trajectory jumps up towards the right branch even if the forcing is turned off (1) and is already moving along the left branch when the forcing turns off (3). Moreover, the forcing turning on (2) has little effect on the evolution of the trajectory, which is already moving along the right branch. The stronger effect an input has on the response oscillatory dynamics, and the one that determines the 4:3 pattern is the forcing turning off (1) that delays the jumping up of the trajectory's jumping up.

3.3.2 Polyglot Entrainment Responses

Both the standard and non-standard 1:1 Arnold tongues discussed in the previous section consisted of 1:1 entrainment regions where horizontal segments of 1:1 entrainment for constant values of A (as well as vertical segments for constant values of T) are connected. Here we discuss a more complex type of 1:1 entrainment region structure arising in the FHN model, consisting of disconnected horizontal segments for low values of A, while the segments remain connected for higher values of A (e.g., (Figures 3.4-A1 and -B1). These regions appear to have multiple 1:1 Arnold tongues. We refer to this phenomenon where 1:1 entrainment is interrupted as T changes (for constant values of A), and is restored when T changes further, as *polyglot entrainment*. We use the same values of $\alpha = 2$ and $\epsilon = 0.01$ as in the previous section as well as square-wave input with amplitude A (50% duty cycle).

We observed polyglot entrainment in two cases. The first case is when the unforced system has a stable focus and is a damped oscillator (Figure 3.4). Above the dashed magenta horizontal line, the forced system has an unstable focus and

sustained oscillations (Figure 3.4 A1) and below the horizontal line, the forced system has a stable focus and damped oscillations (Figure 3.4 B1). The second case in which we observed polyglot entrainment in two parameter regimes is when an unforced system has an unstable focus with sustained oscillations (Figure 3.7). We discuss these two cases below. The main differences between them and the ones described in the previous sections (monoglot entrainment) is the location of the fixed point, which is closer to the minimum of the v-nullcline in Figure 3.1-C1 than in Figure 3.1-B1. This creates a region of sensitivity to perturbations that is responsible for the generation of the multiple 1:1 tongues.

Stable focus for an unforced system: polyglot entrainment of a damped oscillator

When an unforced system in FHN has stable focus in the vicinity of Hopf bifurcation located near the lower knee of the cubic nullcline, we observed polyglot entrainment responses (Figure 3.4). Here, we take two representative cases. First, when the forced system has unstable focus (along with sustained oscillations) as shown in the Figure 3.4 A1. Figure 3.4-A3, -A5 and -A7 show representative traces for the 1:1 entrainment in the three tongues shown in Figure 3.4-A1 (above the horizontal line). They are generated by an MMO mechanism that controls the time scale by adding SAOs as the period increases and therefore the oscillatory output adapts to the input. The corresponding extended phase-plane diagrams are presented in Figure 3.5.

For the first (left) tongue (Figure 3.4-A3 and Figure 3.5-A) there are no MMOs and the entrainment is standard. The trajectory arrives at the lower knee of the v-nullcline and jumps up towards the right branch. The motion of the v-nullcline following the input does not interfere with this process.

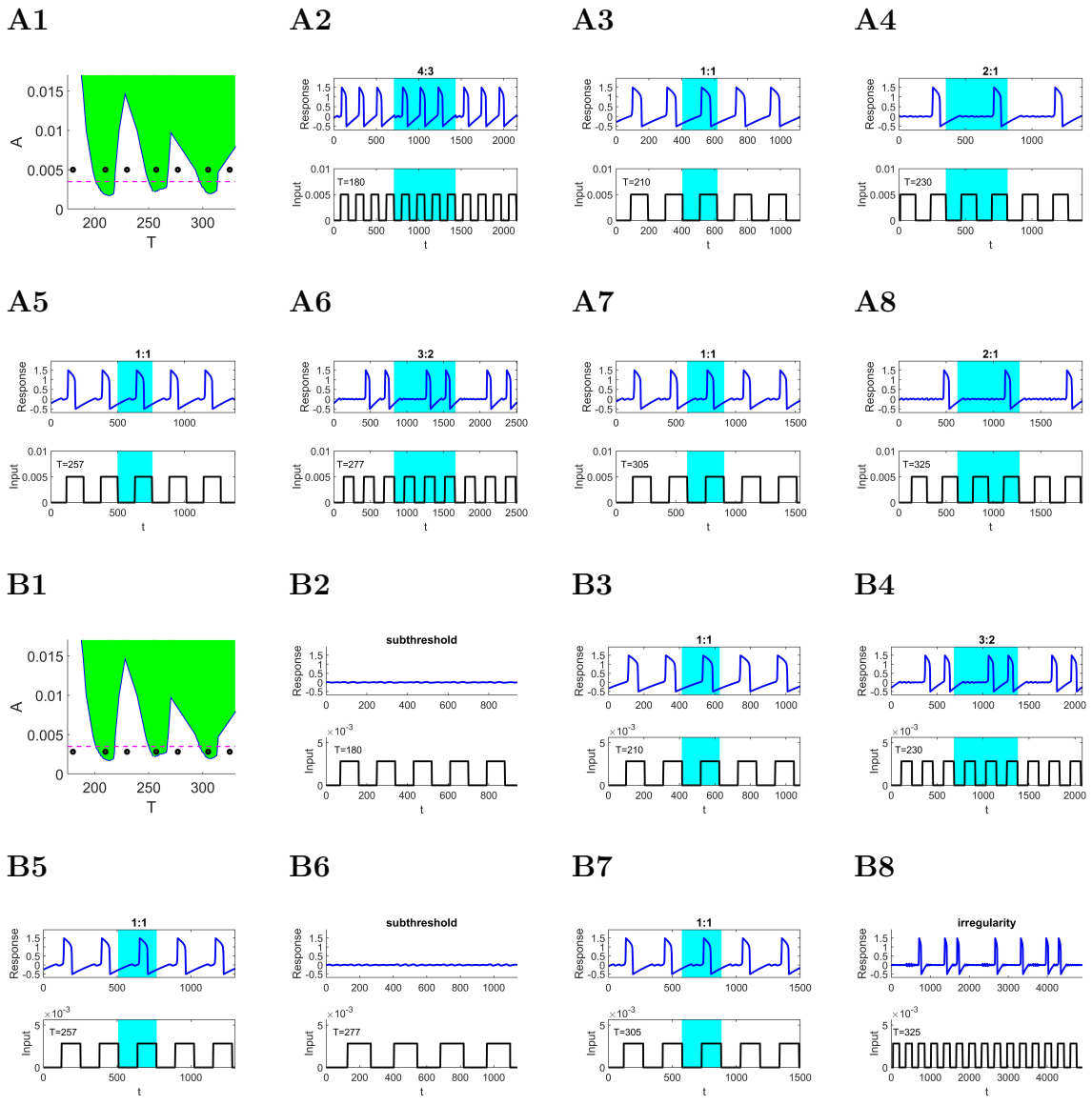

Figure 3.4 Representative entrainment patterns and Arnold tongues with polyglot structure in response to square-wave inputs. **A1 & B1.** Arnold tongues showing 1:1 entrainment regions (highlighted in green). **Remaining panels.** Time courses for v and the forcing for the values of T and A indicated in A1 and B1 (black markers). The dashed-magenta (horizontal) lines in panels A1 and B1 indicate the value of A for which the system with constant forcing A changes from a stable (below) to an unstable (above) focus. **A.** $A = 0.005$. **B.** $A = 0.00282$. The fixed point for the unforced system is a stable focus (Figure 3.1 C). We used the following parameter values: $\alpha = 2$, $\lambda = 0$ and $\epsilon = 0.01$.

For the second (middle) tongue (Figure 3.4-A5 and Figure 3.5-C), the trajectory crosses the v-nullcline in a vicinity of the lower knee, to the right, and turns back instead of jumping up towards the right branch. The forcing turns on when the trajectory is below the lower knee. This raises the v-nullcline leaving the trajectory in a region of fast fibers and therefore the trajectory jumps up. For the third (right) tongue (Figure 3.4-A7, the mechanism is similar, but the larger forcing period allows the trajectory to evolve around the lower knee twice before jumping up.

These mechanisms of 1:1 entrainment can be disrupted in different ways (Figure 3.4-A2, -A4, -A6 and -A8). In Figure 3.4-A2 the forcing is too fast, and activates the SAO mechanism only once every three cycles. In Figure 3.4-A4 (see Figure 3.5-B), when the forcing turns on (2), the v-nullcline rises and the fixed-point raises too. As a result, the trajectory spirals out around this (forced) unstable fixed point until the forcing turns off (3). When this happens the trajectory spirals into the (unforced) stable fixed-point until the forcing turns on again (4) and the trajectory is able to jump up towards the right branch as the result of the v-nullcline rising and leaving the trajectory in a region of fast fibers (below the knee). These additional oscillations disrupt the ability of the cell to follow the input. The disruption mechanisms in Figure 3.4-A6 and -A8 are similar to this one.

Second, when the forced system has a stable focus (and damped oscillations) as shown in the Figure 3.4 B1. Figure 3.4-B3, -B5 and -B7 show representative traces for the 1:1 entrainment in the three tongues shown in Figure 3.4-B1 (below the horizontal line). They are also generated by MMO mechanisms similar to the ones described above as illustrated in Figure 3.6-A and -C. The break of entrainment mechanisms are also similar to those discussed above, except that in some cases, the timing of the output is not good enough to cause the cell to jump up towards the right branch and produce oscillations (Figure 3.4-B2 and -B6). By the time the forcing is turned on,

the trajectory is "inside" the v-nullcline, and by the time the trajectory arrives in the region of fast fibers (below the v-nullcline), the forcing is off.

Unstable focus for an unforced system: polyglot entrainment of a sustained oscillator

Previously, we have observed polyglot entrainment responses when an unforced system has stable focus in the vicinity of Hopf bifurcation. Do we have polyglot entrainment when an unforced system has unstable focus and sustained oscillations? The answer is yes, we observed polyglot structure (Figure 3.7) when an unforced system has unstable focus and sustained oscillations. The idea of having polyglot here is roughly similar to the previous case. In this case, the trajectory shows SAOs before settling on the LAOs. In this case, the polyglot observed has disconnected structure, which means the multiple 1:1 tongues do not merge as we increase A. In the first tongue, there are no MMOs and entrainment is standard. For the second tongue, we have MMOs, which occurs as the forcing period is larger and evolves under the dynamics of an unstable focus for some time before it jumps to generate LAOs. Since in this case, for an unforced system, an unstable focus (with SAOs) is followed by LAOs, the amplitude of the forcing is relatively smaller for having polyglot entrainment. The reason is, as we increase A, the damping associated with the trajectory around an unstable fixed point decreases. As the damping of an unstable fixed point decreases, unforced and forced systems are far away from each other, and hence, have less of polyglot entrainment occuring.

The breaking of 1:1 entrainment is shown via phase-plane diagrams (Figure 3.8). For $T = 205$, we have 1:1 entrainment (Figure 3.8 A1-A3). When the forcing turns on, the switching point lies below the forced separatrix, hence trajectory goes into a spiking mode, traversing around the plane in a counterclockwise manner. When the forcing turns off, the switching point lies on the slow branch of the cubic, hence, the

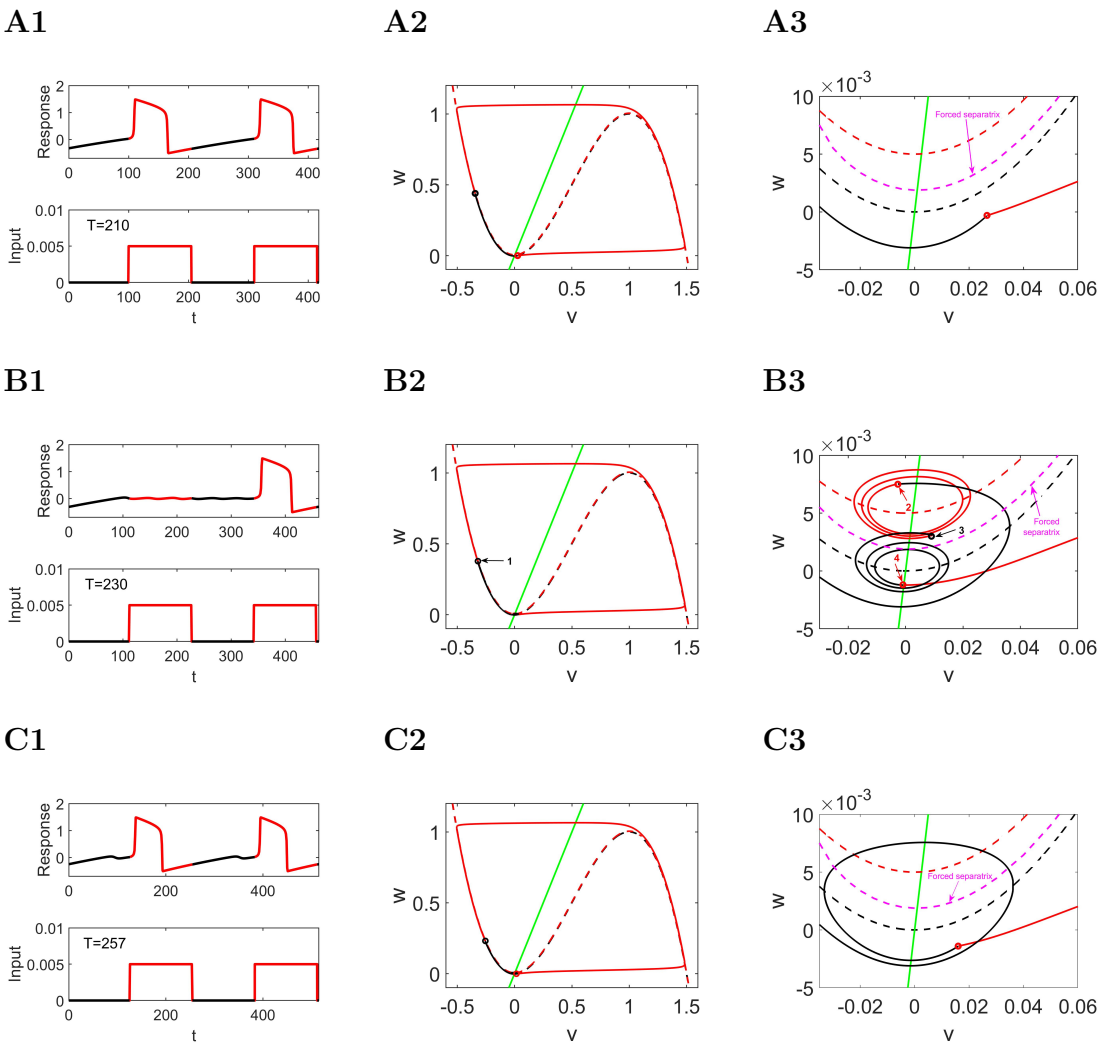

Figure 3.5 Representative examples of 1:1 polyglot entrainment dynamics and their breakdown (Figure 3.4 A). **Left column.** Time courses for v and the forcing. **Middle column.** Phase-plane diagrams. **Right column.** Phase-plane diagram magnification in vicinities of the knee of the v-nullclines. The black (red) portions of the v time courses and trajectories correspond to the forcing turned off (on). **A.** 1:1 entrainment for $T = 210$ (Figure 3.4 A3). **B.** 2:1 entrainment for $T = 230$ (Figure 3.4 A4). **C.** 1:1 entrainment for $T = 257$ (Figure 3.4 A5). We used the following parameter values $\alpha = 2$, $\lambda = 0$, $A = 0.005$ and $\epsilon = 0.01$.

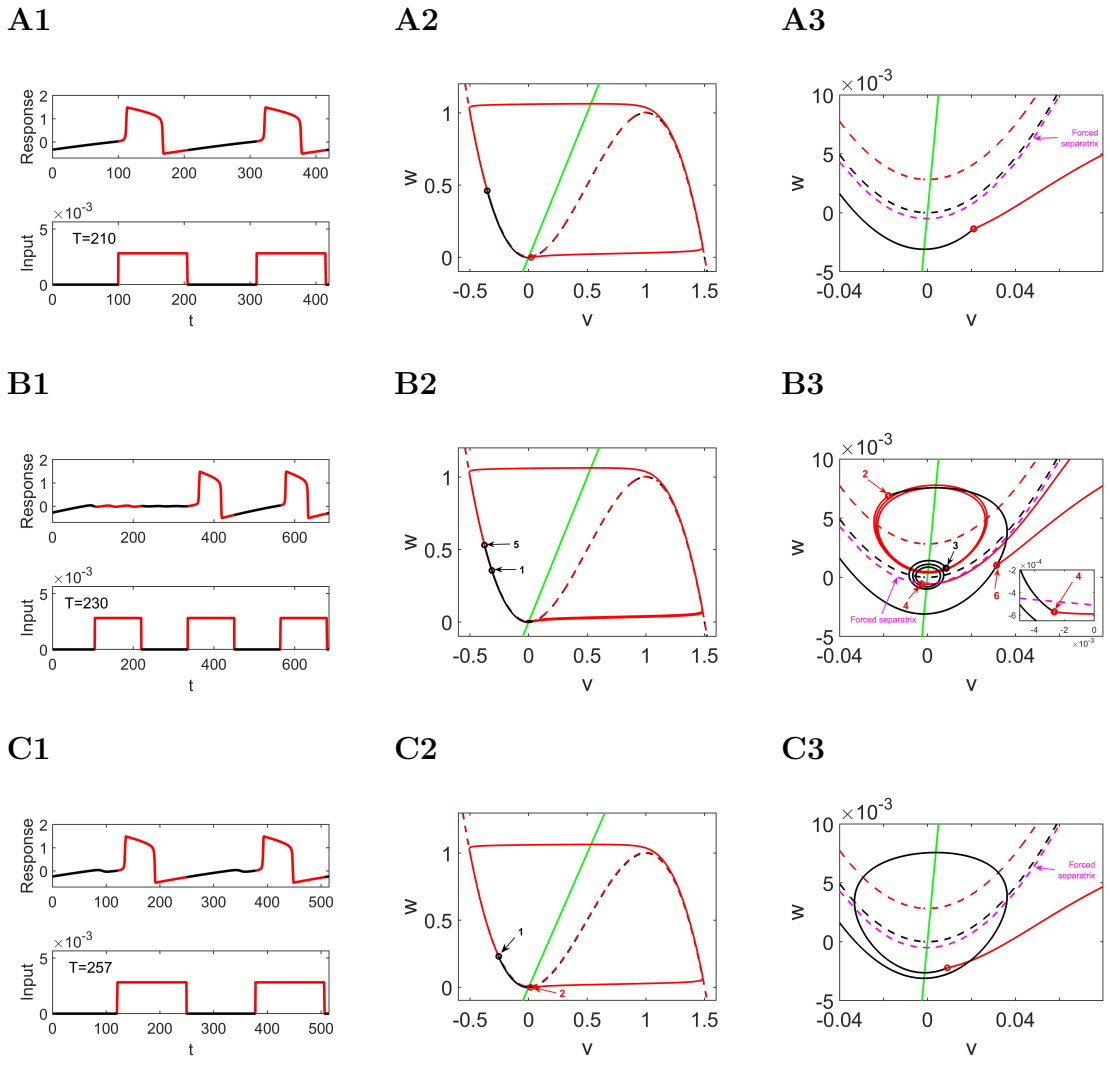

Figure 3.6 Representative examples of 1:1 polyglot entrainment dynamics and their breakdown. **Left column.** Time courses for v and the forcing. **Middle column.** Phase-plane diagrams. **Right column.** Phase-plane diagram magnification in vicinities of the knee of the v-nullclines. The black (red) portions of the v time courses and trajectories correspond to the forcing turned off (on). **A.** 1:1 entrainment responses for $T = 210$ (Figure 3.4 B2). **B.** 3:2 entrainment responses for $T = 230$ (Figure 3.4 B4). **C.** 1:1 entrainment responses for $T = 257$ (Figure 3.4 B5). We used the following parameter values $\alpha = 2$, $\lambda = 0$, $A = 0.00282$ and $\epsilon = 0.01$. (Figure 3.4 B).

trajectory asymptotically approaches towards the lower knee until the forcing turns on again.

Increasing T ($T = 267$) breaks 1:1 entrainment (Figure 3.8 B1-B3). In this case, $2:2$ responses have been observed. Two switching points (3 and 4) are shown in the full picture of the phase plane, while two switching points are shown in the magnified phase plane showing the important dynamics. We see that the switching point labelled as 1 give rise to SAOs followed by LAOs and the switching point labelled 3 gives LAOs only. Hence, for one input, we have damping followed by a spike and for the second input, we have a spike with no damping.

For $T = 398$, we get 1:1 entrainment (Figure 3.8 C1-C3). When the forcing turns off, the switching point in black in the magnified panel lies very close to an unstable fixed point (above the unforced separatrix), hence the trajectory takes longer to spiral away from it. When the forcing turns on, the switching point lies below the forced separatrix, hence a spike is created. Since T is long enough, the trajectory traverses around the phase plane and approaches the lower knee until the forcing turns off again and the cycle begins.

3.3.3 Regions of Monoglot and Polyglot Entrainment

Having the results of monoglot and polyglot entrainment, a question arises here: For what range of λ values do we have monolgot entrainment responses and polyglot entrainment responses?

Monoglot entrainment structure comes in two versions: standard and non-standard. Standard monoglot entrainment is like a typical Arnold tongue as shown in the Figure 3.2 A and is observed when an unforced system has sustained oscillations. In this case, bifurcation has occurred and the real part associated with the unstable fixed point is large in magnitude. Non-standard monoglot entrainment (shown in the Figure 3.2 B and C) is observed when λ is chosen far away from Hopf bifurcation. In

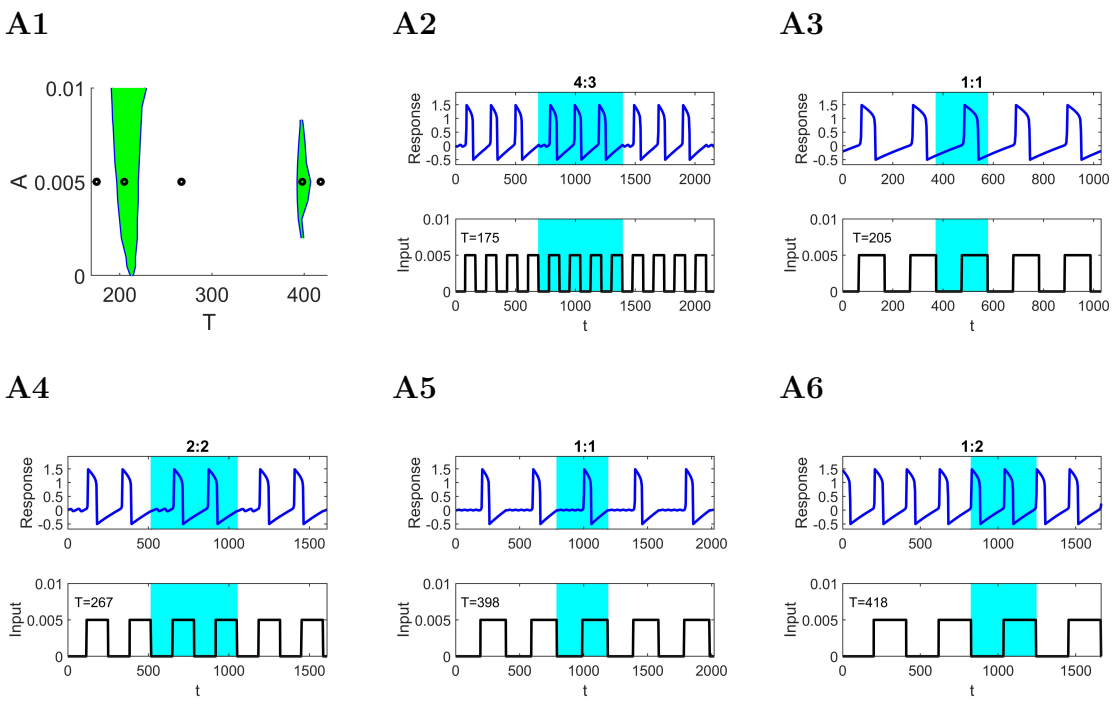

Figure 3.7 Representative entrainment patterns and Arnold tongue with polyglot structure in response to square-wave inputs. **A1.** Arnold tongue showing 1:1 entrainment regions (highlighted in green). **Remaining panels.** Time courses for v and the forcing for the values of T and A indicated in A1 (black markers). The fixed point for the unforced system is an unstable focus (Figure 3.1 D). We used the following parameter values: $\alpha = 2$, $A = 0.005$, $\lambda = 0.004$ and $\epsilon = 0.01$.

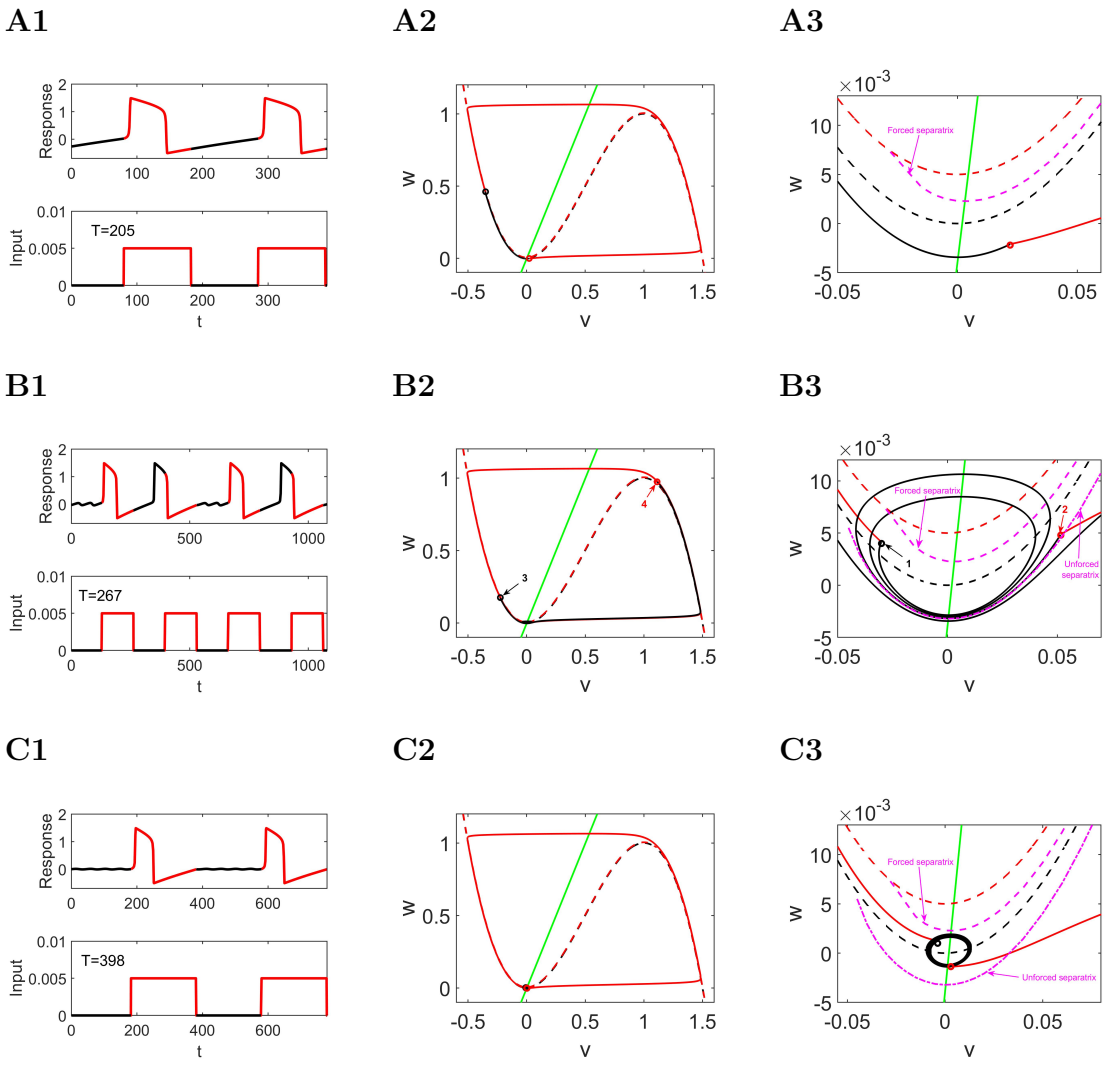

Figure 3.8 Representative examples of 1:1 polyglot entrainment dynamics and their breakdown (Figure 3.7). **Left column.** Time courses for v and the forcing. **Middle column.** Phase-plane diagrams. **Right column.** Phase-plane diagram magnification in vicinities of the knee of the v-nullclines. The black (red) portions of the v time courses and trajectories correspond to the forcing turned off (on). **A.** 1:1 entrainment for $T = 205$ (Figure 3.7 A3). **B.** 2:2 entrainment for $T = 267$ (Figure 3.7 A4). **C.** 1:1 entrainment for $T = 398$ (Figure 3.7 A5). We used the following parameter values $\alpha = 2$, $\lambda = 0.004$, $A = 0.005$ and $\epsilon = 0.01$.

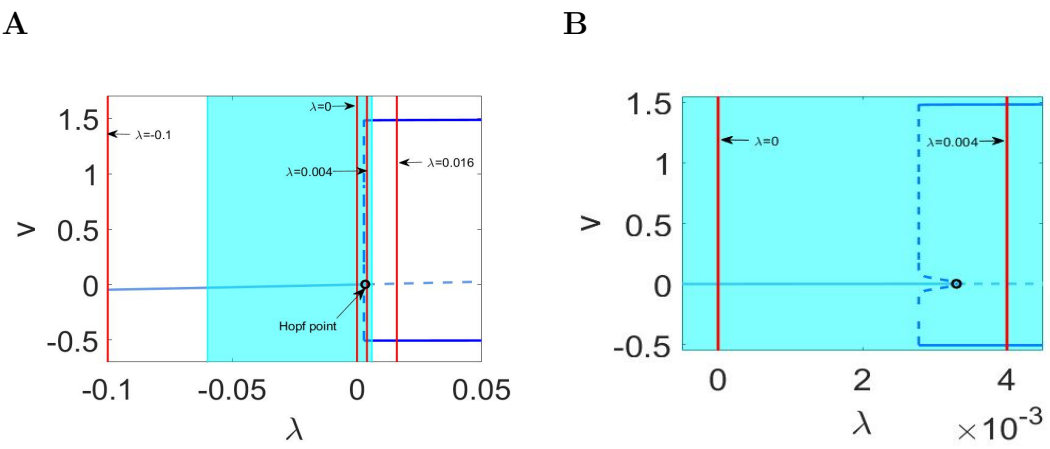

Figure 3.9 Bifurcation diagram as a function of the parameter λ for $\alpha = 2$. We have Hopf bifurcation at $\lambda = 0.0033$. **A.** The shaded region denote the λ values for the unforced system for which we have 1:1 polyglot entrainment. The red lines denote the representative λ values used in the previous figures for the unforced system. $\lambda = 0.016$ (Figure 3.2 A), $\lambda = -0.1$ (Figure 3.2 B and C), $\lambda = 0$ (Figure 3.4) and $\lambda = 0.004$ (Figure 3.7). **B.** Magnification of **A** around the Hopf point showing that Hopf bifurcation is subcritical.

this case, the resultant fixed point is either stable focus (with an eigenvalue whose real part is large) or a stable node. Polyglot entrainment is observed for λ values in the vicinity of Hopf bifurcation. In this case, the unforced system has either stable focus or unstable focus.

Bifurcation diagram for $\alpha = 2$ is shown in the Figure 3.9. Panel A shows the bifurcation diagram with the shaded region. The shaded region represents the λ values in which we have polyglot entrainment. For λ value outside the shaded region will give monoglot entrainment responses. Panel B shows the magnification of A showing that bifurcation is subcritical as an unstable limit cycle emanates from the Hopf point. Red lines in the bifurcation diagram denote the representative examples of monoglot and polyglot entrainment responses.

3.3.4 Monoglot and Polyglot Entrainment in other Parameter Regimes

In the above sections we have focused on a scenario in which the unforced system has some degree of time scale separation ($\epsilon = 0.01$), undergoes a subcritical Hopf bifurcation as λ is varied ($\alpha = 2$), and the periodic forcing $F(t)$ takes the form of a square wave. Since the location and criticality of the Hopf bifurcation depends on model parameters, we also explored other parameter regimes. We have observed monoglot entrainment in systems with less time scale separation ($\epsilon = 0.1$), a supercritical Hopf bifurcation as λ is varied ($\alpha = 4$), and sinusoidal forcing. Here, we briefly discuss the results in these other parameter regimes.

Effect of time scale separation - Monoglot and Polyglot entrainment As ϵ is increased, the slow-fast nature of the system decreases and trajectories may no longer leave the lower knee region along fast fibers. Nonetheless, with $\epsilon = 0.1$, we still observe both standard and nonstandard monoglot Arnold tongues similar to the case with $\epsilon = 0.01$ (cf. Figure 3.2 and Figure A.4). However, with $\epsilon = 1$, the forced system only exhibits subthreshold responses and thus we do not consider them to be entrained. This is due to fixed points along the middle branch of the cubic nullcline becoming stable at higher ϵ values. Polyglot entrainment responses are observed by increasing ϵ to 0.6. As it increases more, we lose polyglot entrainment responses as the trajectory doesnt go to the right branch of the cubic nullcline and in that case we do not call it a spike response. Polyglot entrainment for $\epsilon = 0.1$ is shown (Figure A.5).

Second, we consider the criticality of the Hopf bifurcation. When the unforced system undergoes a supercritical Hopf bifurcation ($\alpha = 4$), we see a monoglot entrainment structure with standard and nonstandard Arnold tongues similar to the subcritical Hopf case ($\alpha = 2$, cf. Fig. 3.2 and A.6). Finally, we consider the form of the periodic forcing. With sinusoidal forcing, we do observe standard monoglot

Arnold tongues but do not find the type of nonstandard monoglot Arnold tongues that were observed with square-wave forcing (cf. Fig. 3.2 and A.12).

Increasing α - Monoglot and Polyglot entrainment For $\alpha = 4$, we have supercritical Hopf bifurcation. Standard and non-standard monoglot entrainment responses (Figure A.6) were also observed for $\alpha = 4$ and happen in the similar way like $\alpha = 2$. Similarly, polyglot entrainment responses are also observed for $\alpha = 4$ in the vicinity of Hopf (Figures A.7 and A.8). The breaking and regaining of 1:1 entrainment is shown by representative phase plane diagrams (Figures A.9 and A.10). The difference we observed for $\alpha = 4$ is that, since for $\alpha = 4$, the region of focus type fixed increase as we vary λ, hence the region of polyglot entrainment is larger (Figure A.11).

Sinusoidal Forcing - Monoglot and Polyglot entrainment So far the results we presented were for the square-wave periodic forcing, which induces abrupt changes in the system. We also investigated sinusoidal periodic forcing, which induces gradual changes in the system. For sinusoidal forcing, we only observed standard monoglot structure (Figure A.12). Non-standard monoglot doesnt exist as decreasing λ always give polyglot entrainment responses. Representative polyglot entrainment responses for sinusoidal forcing are shown (Figures A.13 and A.14). The bifurcation diagram (Figure A.15) shows that for sinusoidal forcing, the polyglot entrainment region is much larger.

CHAPTER 4

ANALYSIS OF POST-TRANSLATIONAL CIRCADIAN CLOCK MODELS

4.1 Introduction

In chronobiology, biological rhythms are the periodic changes of activity which occur in living organisms. A well-known example of these rhythms is called circadian rhythms. A rhythm is said to be a 'circadian' if it meets three fundamental properties: it must be intrinsically rhythmic with an $\sim$24 hour period in constant conditions; it must maintain its rhythmic nature across certain temperature ranges; and it must be entrainable to environmental cues. These entraining agents (also called zeitgebers) include light, nutrition, temperature, and social interactions. Among these cues, light is considered to be the strongest zeitgeber. Most eukaryotic organisms, such as mammals, insects, plants, and fungi, use circadian clocks to synchronize (or entrain) to environmental cycles.

Disruption of circadian rhythms has severe consequences for metabolism and brain function [47]. Often, such circadian desynchrony leads to a broad spectrum of health problems, such as jet lag, delayed sleep phase syndrome, cardiovascular disease, and cancer.

Transcriptional/translational feedback loops (TTFLs) [9, 42, 43, 87] are a basis for circadian oscillations in many organisms. In mammalian circadian cells, the TTFL has the following structure: clock genes *per* and *cry* are transcribed into mRNA and then translated into the proteins PER and CRY. These proteins then inhibit their own transcription, forming a negative feedback loop.

Traditionally, TTFLs were considered to be required for generating circadian oscillations [9, 10, 22, 65]. However, we now know that in some cells and organisms circadian oscillations can also be generated without a TTFL through post-translational

modifications such as phosphorylation and dephosphorylation [69, 81, 90]. These modifications occur after the translation process with the help of enzymes such as kinases and phosphatases [31, 57, 64].

Circadian oscillations in cyanobacteria occur in an ordered manner [15,81]. The circadian clock of cyanobacteria is composed of three proteins: KaiA, KaiB and KaiC. KaiC protein has a hexameric shape which has two terminals called CI and CII, with CII having binding site for the protein KaiA called an A-loop. The CII terminal of KaiC has two residues for autophosphorylation, serine at position 431 (also called S431) and threonine at position 432 (also called T432).

At dawn, KaiC happens to be in an unphosphorylated state (U-KaiC) and the A-loops in CII terminal are exposed. KaiA binds to the A-loops stimulating KaiC autokinase activity, and hence KaiC at T432 becomes phosphorylated by attaching phosphate group to the T432 (ATP is converted into ADP). Phosphorylation of T432 is followed by phosphorylation of S431 hence both sites are phosphorylated. As dusk begins, conformational changes [15,44,89] also occur in KaiC and the A-loop of KaiC is then buried. At this stage, another process comes into play called dephosphorylation which requires autophosphatase activity in which the protein KaiB is involved. In order for KaiB to interact with KaiC at CI terminal, B-loop at CI should be exposed. As B-loop gets exposed, KaiB interact with it. As night time begins, KaiA cannot bind anymore to the A-loop as it is not active. KaiB in its active form interacts with KaiA, thereby sequestering KaiA so that KaiA can no longer bind to the A-loop on KaiC. Once autokinase activity has stopped, and autophosphatase activity starts, KaiC at threonine position dephosphorylates followed by dephosphorylation of KaiC at the serine position. At dawn, KaiC returns into its unphosphorylated state with A-loops exposed and the cycle begins anew.

In this chapter, we discuss circadian clock models which are based upon post-translational modifications. In cyanobacteria, although in vivo requires TTFL for

circadian oscillations, in contrast, in vitro, modification of the KaiC protein in a test tube with the help of proteins KaiA, KaiB and adenosine triphosphate (ATP) is sufficient to generate circadian oscillation [69, 81].

In Section 4.2.1, we take the mathematical model for circadian oscillation in cyanobacteria developed by Michael J. Rust. The reaction scheme is presented, from which the 3D model is formed using mass action kinetics. Limit cycle trajectory in phase space and time course is also shown. In Section 4.2.2, we present another mathematical model for circadian oscillations developed by Mark Byrne. The reaction schematic is also shown, which illustrates the essential features of the model. Equations are shown to demonstrate how the 4D model is reduced to 2D.

In this section, we analyze the mathematical modes presented in Section 4.2.1 and 4.2.2. Section 4.3 shows the results for the Rust model and Section 4.4 show the results for Byrne model. For analysis of the models, we use dynamical systems tools to understand how limit cycle oscillations are formed. Dynamical system tools include fixed points analysis, bifurcation diagrams, and linearization analysis. Dynamical systems tools presented here help us in understanding how limit cycle trajectory is formed and evolves across the switching manifold in both models. Results for both models show surprisingly similar results although both are different models in terms of dimensionality, structure and parameter values. In Section 4.5, we compare the period of oscillations in the Rust model and Byrne model with the experimental findings.

4.2 Cyanobacterial Circadian Clock Models

How in vitro oscillator of cyanobacteria works with the help of kai proteins and energy is well studied [53, 69, 70]. From a theoretical point of view, various mathematical models have also been developed to describe the circadian oscillations in cyanobacteria. David Lubensky and his colleagues constructed the model [74] which

incorporates how energy sources (ATP and ADP) interact with the different domains of KaiC hexamer and drives the circadian clock of cyanobacteria. Their work focuses on how conformational changes of KaiC hexamer occur between active and inactive states by ATP breakdown reaction to CI domain and its effect on phosphorylation at CII domain. Modeling conformational changes of KaiC hexamers, some of the work of Lubensky and his colleagues also presented a mathematical model which incorporates the allosteric regulation of KaiC phosphorylation [92]. They showed the synchronization phenomenon among KaiC hexamers. Lubensky et al. in another work showed the robustness of limit cycle oscillations in cyanobacteria to noise in the input signal [66]. They compared the performance of the limit cycle oscillator (from three proteins) with damped oscillator and an hourglass-like oscillator (i.e. an unforced system that is non-oscillatory shows oscillations when driven by forcing). They showed the effectiveness of limit cycle oscillators over damped and hourglass-like oscillators in response to different intensities of noise. Their findings showed that limit cycle oscillators are more robust to high noise. Cyanobacterial clock is also modeled by [97] in which they call it an hourglass model: sand fills the hourglass at day time (KaiC phosphorylation) and emptied at nigh time (KaiC dephosphorylation). Their model incorporates monomer exchange of KaiC hexamer and clustering of KaiC hexamers by interacting with other proteins at night time. Along similar lines, modeling work by Yoda et al. [100] also shows incorporating monomers exchange and allosteric regulation of KaiC. Modeling studies by Aihara et al. [56] highlighted the role of KaiA and KaiB in nonlinearities needed for circadian oscillations. They also showed relaxation type oscillations in their model. Mark Byrne discussed and compared a variety of the proposed mathematical models for the in vitro KaiABC oscillator in cyanobacteria [19] .

Michael Rust and his group have made significant contribution to the field in terms of modeling circadian oscillations in cyanobacterial clocks. Rust et al.

presented a model for circadian oscillations in cyanobacteria and highlighted that the model shows oscillations in forms of KaiC phosphorylation and dephosphorylation in a well-defined sequential way [81]. Yet this model does not shows the explicit effect of the protein KaiB. After developing the model which represents the unforced system, Rust et al. studied the effect of forcing on the cyanobacterial circadian clock [80] and explained the entrainment mechanism to light dark cycles. They showed that changes in the energy source (ATP/ADP) brings a phase-shift when KaiC phosphorylated during the oscillations. Rust and his group also presented the mathematical model showing the interaction of input signals with KaiC domains CI and CII, the robustness of the clock to environmental changes and the effect of ATPase activity for different KaiB and KaiC complexes [76]. In their work [13], they showed how the protein KaiB interacts explicitly with the clock components. Besides the work by Lubensky and his colleagues, stochastic effects have also been studied by Rust et al. [14] in the cyanobacterial circadian clock. They used stochastic modeling to study the circadian oscillations in cyanobacterial clock. Their work showed that a species of cyanobacteria lacking KaiA which acts like a hourglass system, performs better than a free running circadian clock in the presence of internal molecular noise. In contrast, when internal noise is low and external fluctuations are large, the free running circadian clock outperforms the hourglass like systems.

Though the Rust model [81] has been widely used, it has not been thoroughly analyzed from a dynamical systems perspective. Our aim is to analyze the Rust model from a dynamical point of view, namely, how circadian limit cycle oscillations are generated using dynamical system's tools.

4.2.1 Rust Model

In this section, we describe a three dimensional model of post-translational oscillations for the cyanobacteria developed by Rust et al. [81].

Model equations are:

$$\frac{dT}{dt} = k_{UT}(S)U + k_{DT}(S)D - k_{TU}(S)T - k_{TD}(S)T \tag{4.1}$$

$$\frac{dD}{dt} = k_{TD}(S)T + k_{SD}(S)S - k_{DT}(S)D - k_{DS}(S)D \tag{4.2}$$

$$\frac{dS}{dt} = k_{US}(S)U + k_{DS}(S)D - k_{SU}(S)S - k_{SD}(S)S \tag{4.3}$$

$$A = max\{0, [KaiA] - 2mS\} \tag{4.4}$$

$$k_{XY} = k^0_{XY} + \frac{k^A_{XY}A(S)}{K_{1/2} + A(S)} \tag{4.5}$$

Conservation equation:

$$U + T + D + S = [KaiC] \tag{4.6}$$

Figure 4.1 shows the reaction network of the Rust model. The variable U denotes the KaiC protein in an unphosphorylated state, variable T denotes phosphorylation of KaiC at the T site only, variable D denote KaiC phosphorylation at both T and D sites and variable S denote phosphorylation of KaiC at the S site only. Orange lines denote the phosphorylation processes. The rate constant for the transition from an unphosphorylated state U to phosphorylated state T is denoted by k_{UT} and similarly others. A is the concentration of active monomers of KaiA which depends on the KaiC at S site only. The role of KaiB is implicitly defined in the definition of active KaiA monomers (A). m is the stoichiometric coefficient chosen to be 1 (which mean that one S-KaiC monomer sequester one KaiA dimer via KaiB). The total rate (k_{XY}) is the sum of basal rates (denoted by k^0_{XY}) and maximal rates (denoted by k^A_{XY}). Each k_{XY} has Michaelis Menten kinetics. The parameter $K_{1/2}$ is taken from the hyperbolic fit to the experimental data on the dependence of rate from U to T state on KaiA. It is assumed to be same for all other rates.

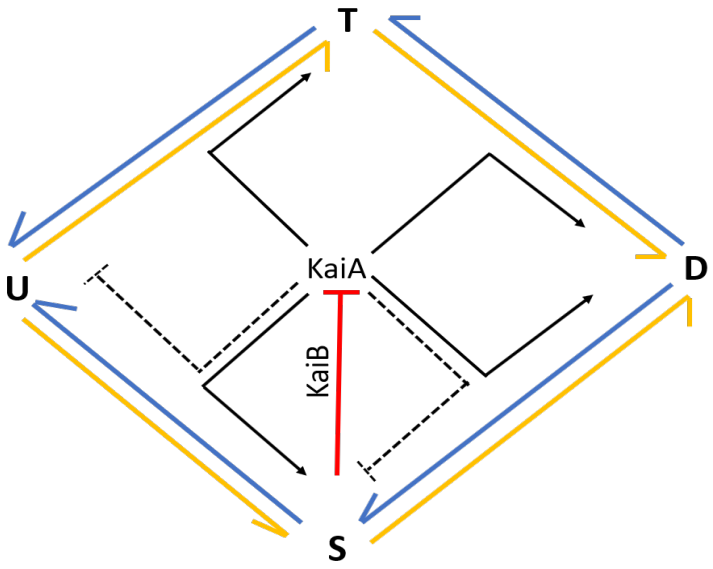

Figure 4.1 Biochemical schematic of three proteins clock [81]. Blue lines denote the dephosphorylation processes. Solid black lines originating from KaiA indicate that KaiA induces phosphorylation and dashed black lines originating from KaiA indicate that KaiA inhibits the indicated dephosphorylation processes. Red line going from S to KaiA describe the sequestration of KaiA via KaiB at S site of KaiC.

In this model, we see that the concentrations of three phosphorylated species are the only dynamical variables; the interconversion between phosphoforms are first order; rates are Hill function of KaiA and each S-KaiC monomer (together with KaiB) inactivates one KaiA dimer.

The parameters in Table 4.1 taken from [81] were obtained from partial experiments with and without KaiA. With the given parameter values and proteins concentration defined below, the model gives limit cycle oscillations with a period of ≈ 21 hours (Figure 4.2).

Each rate parameter has the unit of $1/h$. Others parameter values used: $K_{1/2} = 0.43\mu M$, $m = 1$, [KaiA] $= 1.3\mu M$, [KaiC] $= 3.4\mu M$.

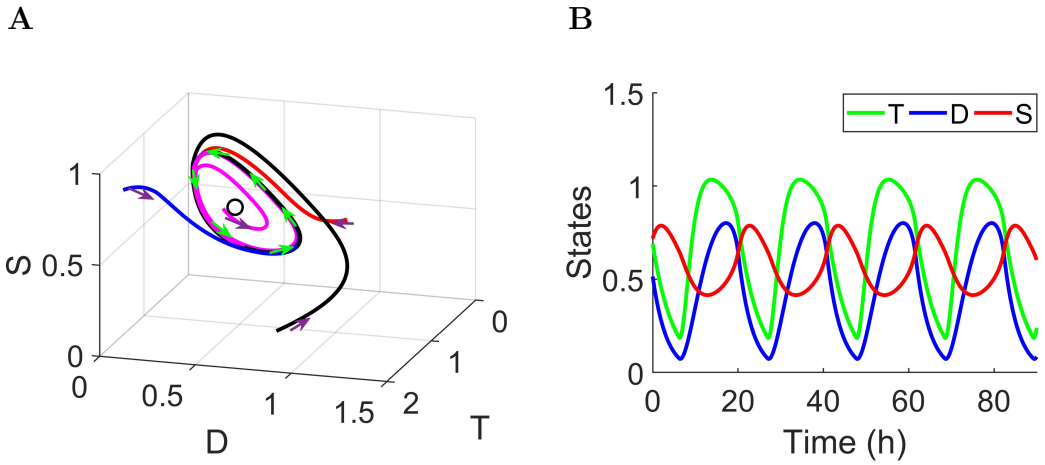

Figure 4.2 Limit cycle trajectory of the Rust model for KaiA = 1.3. **A** shows three dimensional view of different trajectories (in different colors) starting with various initial conditions converge towards the stable limit cycle trajectory indicated by green arrows. Dark blue arrows show the direction of the trajectories. Black dot denotes the unstable fixed point. **B** shows the time course oscillations of the Rust model.

Table 4.1 Rust Model Parameters

Basal Rates	Values	Maximal Rates	Values
k^0_{UT}	0	k^A_{UT}	0.479
k^0_{TD}	0	k^A_{TD}	0.213
k^0_{SD}	0	k^A_{SD}	0.506
k^0_{US}	0	k^A_{US}	0.053
k^0_{TU}	0.21	k^A_{TU}	0.079
k^0_{DT}	0	k^A_{DT}	0.173
k^0_{DS}	0.31	k^A_{DS}	-0.319
k^0_{SU}	0.11	k^A_{SU}	-0.133

4.2.2 Byrne Model

In this section, we discuss a two dimensional circadian model for post-translational oscillations developed by Mark Byrne [12]. The design model states that a protein with at least two modification sites which selectively sequesters an effector molecule (denoted by E in the model) and a time scale separation between the dynamical variables is sufficient to generate sustained circadian oscillations in the population occupancy of the regulatory sites [12]. As the Byrne model is two dimensional, phase plane analysis can be utilized to gain insight into the system's dynamics. Model equations are:

$$\frac{dx}{dt} = k_{+1}(x, y)(1 - x) - k_{-1}x \tag{4.7}$$

$$\frac{dy}{dt} = k_{+2}(x, y)(1 - y) - k_{-2}y \tag{4.8}$$

$$E = max\{0, E_0 - y(1 - x)\} \tag{4.9}$$

$$k_{+j} = k_{+j,max}\frac{E}{E + K} \tag{4.10}$$

The state x and y represents the fractional occupancy of each residue on some protein. Model equations are globally coupled via the effector concentration E. E_0 represents the initially available concentration of effector concentration. In the Byrne model, E and E_0 has similar role like A and KaiA in the Rust model.

Model parameter values are: $E_0 = 0.2$, $K = 0.04$, $k_{+1,max} = k_{-1} = 0.4$, $k_{+2,max} = k_{-2} = 0.03$. Each rate has the unit of $1/h$.

Nullclines: Since E is non-smooth function. We find nullclines based on different values E takes on. i-e for $E = 0$ and $E = E_0 - y(1 - x)$. x-nullcline is denoted by $N_x\left(\frac{dx}{dt} = 0\right)$ and y-nullcline is denoted by $N_y\left(\frac{dy}{dt} = 0\right)$.

- For $E = 0$, the x and y nullclines are the y-axis and x-axis respectively.

- For $E = E_0 - y(1-x)$, the x and y nullclines are:

  $N_x(x) = \dfrac{\big(E_0(1-x) - cx(K+E_0)\big)}{(1-x)(1-x-cx)}$ and $N_y(x) = \dfrac{-B - \sqrt{B^2 - 4AE_0}}{2A}$.

  where $b = \dfrac{k_{-2}}{k_{+2,max}}$, $c = \dfrac{k_{-1}}{k_{+1,max}}$, $A = (1+b)(1-x)$ and $B = x-1-bK-E_0(1+b)$.

We can also go from x, y to the 4 state system i-e $X^{(0,0)}$, $X^{(0,1)}$, $X^{(1,0)}$, $X^{(1,1)}$ using these equations:

$$X^{(0,0)} = (1-x_1)(1-x_2) \tag{4.11}$$

$$X^{(1,0)} = x_1(1-x_2) \tag{4.12}$$

$$X^{(0,1)} = x_2(1-x_1) \tag{4.13}$$

$$X^{(1,1)} = x_1 x_2 \tag{4.14}$$

The four states system becomes:

$$\frac{dX^{(0,0)}}{dt} = -(k_{+1} + k_{+2})X^{(0,0)} + k_{-1}X^{(1,0)} + k_{-2}X^{(0,1)} \tag{4.15}$$

$$\frac{dX^{(1,0)}}{dt} = -(k_{-1} + k_{+2})X^{(1,0)} + k_{+1}X^{(0,0)} + k_{-2}X^{(1,1)} \tag{4.16}$$

$$\frac{dX^{(1,1)}}{dt} = -(k_{-1} + k_{-2})X^{(1,1)} + k_{+1}X^{(0,1)} + k_{+2}X^{(1,0)} \tag{4.17}$$

$$\frac{dX^{(0,1)}}{dt} = -(k_{-2} + k_{+1})X^{(0,1)} + k_{-1}X^{(1,1)} + k_{+2}X^{(0,0)} \tag{4.18}$$

4.3 Dynamic Analysis of the Rust Model

To analyze the mechanism of oscillations generated in the Rust model, we use dynamical system tools such as fixed point analysis, time course, bifurcation diagram

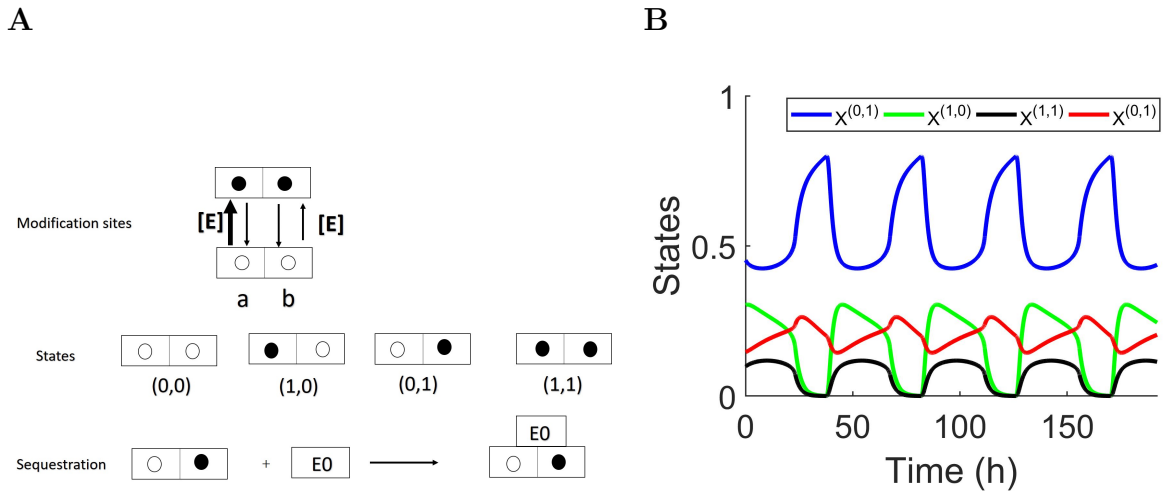

Figure 4.3 **A** shows the reaction schematic for the Byrne model [12]. **B** shows the time course for the four state system. Parameter values used are: $E_0 = 0.2$, $K = 0.04$, $k_{1,max} = k_{-1} = 0.4$, $k_{2,max} = k_{-2} = 0.03$.

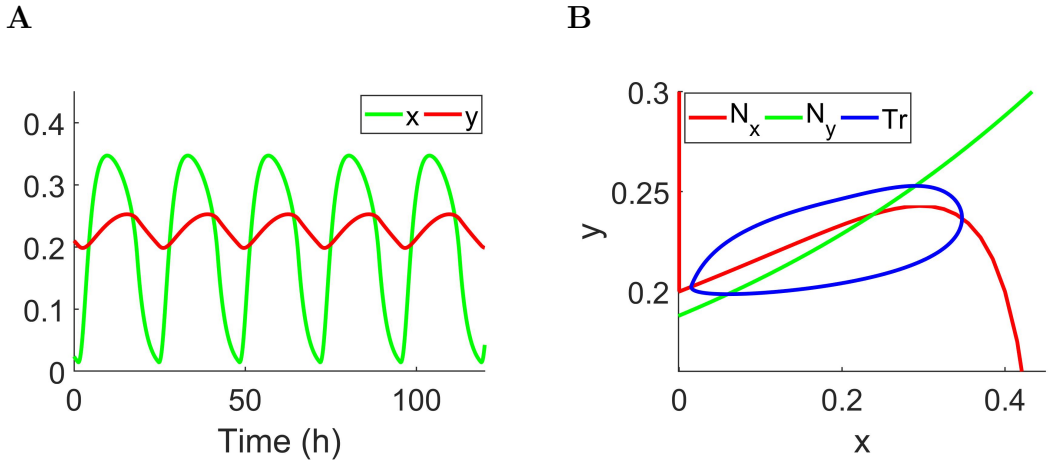

Figure 4.4 Representative time course dynamics in **A** and phase plane diagram in **B** for the 2D Byrne model. We used the following parameter values: $E_0 = 0.2$, $K = 0.04$, $k_{1,max} = k_{-1} = 0.4$, $k_{2,max} = k_{-2} = 0.03$.

and phase space/plane. The purpose of such dynamic analysis is to gain insight into the system's trajectories.

Fixed points Analysis

For fixed point analysis, we rewrite the Rust model in an alternative form (right-hand sides of the system as a sum of linear and nonlinear functions):

$$\frac{dT}{dt} = -0.21T + F(S)[1.6286 - 0.7718T - 0.306D - 0.479S] \tag{4.19}$$

$$\frac{dD}{dt} = -0.31D + F(S)[0.213T + 0.147D + 0.5057S] \tag{4.20}$$

$$\frac{dS}{dt} = 0.31D - 0.11S + F(S)[0.1809 - 0.0532T - 0.3732D - 0.4489S] \tag{4.21}$$

where

$$F(S) = \frac{A(S)}{K_{1/2} + A(S)} \tag{4.22}$$

and

$$A(S) = \max(0, \text{KaiA} - 2mS) \tag{4.23}$$

Fixed points have been calculated by using **fsolve** routine in MATLAB (The Mathworks, Natick, MA) using different initial conditions. The stability of the fixed points is calculated by finding the eigenvalues of the jacobian matrix evaluated at the fixed points.

Linear regime: In the Rust model, each rate constant has non-linearity which depends on S. Particularly, in the model, $A = max\{0, [\text{KaiA}] - 2mS\}$ is the source of linearity/nonlinearity. The model is in the linear regime when $A = 0$ (corresponds

to the case when $S \geq \frac{\text{KaiA}}{2m}$). This regime doesn't have a fixed point as it is located at $(T^*, D^*, S^*) = (0, 0, 0)$ which is located in the nonlinear regime, hence it is called virtual a fixed point. This fixed point is a stable node. The eigenvalues are $(-0.21, -0.31, -0.11)$.

Moreover, solving the system in a linear regime, for any state (T, D, S) at the initial time, there exists a unique time of exit τ_{exit} and unique location $(T, D, S)_{\tau_{exit}}$ which is the plane $P = \frac{\text{KaiA}}{2m}$ in the (T, D, S) space.

Non-linear regime: The system has nonlinear dynamics for $S < \frac{\text{KaiA}}{2m}$. In the non-linear regime, $A = [\text{KaiA}] - 2mS$. For KaiA = 1.3, two fixed points have been observed and both are unstable. At this value of KaiA, one of these fixed points has S coordinate to be $S < \frac{\text{KaiA}}{2m}$ and the other has $S > \frac{\text{KaiA}}{2m}$.

(a) First fixed point: The first fixed point is located at

$(T, D, S) = (0.7602, 0.4161, 0.5782)$ whose eigenvalues are $(\alpha_1, \alpha_2, \alpha_3)$, where $\alpha_1 = -0.4552$, $\alpha_2 = 0.1223 + 0.3691i$, and $\alpha_3 = 0.1223 - 0.3691i$. Thus, the fixed point is classified as a spiral saddle index 2, with a unstable spiral in two of the dimensions and stable behaviour in the dimension perpendicular to the spiral surface. The eigenvector matrix associated with these eigenvalues is: $V_1 = (v_1, v_2, \overline{v_2})$, where $v_1 = [0.9966, -0.076, 0.0322]^T$, $v_2 = [-0.6954, -0.6418 + 0.1794i, -0.6418 - 0.1794i]^T$ and $\overline{v_2}$ is the complex conjugate of v_2. Hence, the linearization predicts that near this fixed point, the trajectory is attracting in the T-direction and repelling along the DS-plane.

(b) Second fixed point: The second fixed point is located at

$(T, D, S) = (-3.6207, 0.2380, 0.6842)$, whose eigenvalues are $(\alpha_1^{'}, \alpha_2^{'}, \alpha_3^{'})$, where $\alpha_1^{'} = -0.6259 + 0.2003i$, $\alpha_2^{'} = -0.6259 - 0.2003i$, and $\alpha_3^{'} = 0.8728$. Thus, the fixed point is classified as a spiral saddle index 1, with a stable spiral in two of the dimensions and unstable behaviour in the dimension perpendicular to the spiral surface.

The eigenvector matrix associated with these eigenvalues is: $V_2 = (v_3, \overline{v_3}, v_4)$

where $v_3 = [-0.9978, -0.0584 + 0.0240i, 0.0211 - 0.0075i]^T$,

$v_4 = [-0.9978, 0.1056, 0.0355]^T$ and $\overline{v_3}$ is the complex conjugate of v_3. Hence, the linearization predicts that near this fixed point, the trajectory is repelling in the S-direction and attracting along the TD-plane.

This fixed point is not biologically reasonable as the T component (denotes a concentration) is negative.

Bifurcation Diagram

For low KaiA values of KaiA (less than ≈ 0.96), the system has a stable fixed point. At around KaiA = 0.96, the fixed point loses stability and a supercritical Hopf bifurcation occurs leading to oscillations. These oscillations persist as we increase KaiA. Subcritical Hopf bifurcation occurs at KaiA ≈ 1.63922. Near to the subcritical Hopf, saddle node bifurcation of periodic orbits occurs at KaiA ≈ 1.63925. The bifurcation diagram is shown in Figure 4.5.

Trajectory behaviour in the Rust model

In the Rust model, trajectory in the phase space is partitioned into two regimes, called 'linear' and 'nonlinear' regimes, where each regime has a qualitatively different vector field.

- In a onlinear regime, we need to know which trajectory stays in the first octant.

  At $S = 0$, T and D are non-negative, hence $S^{'} > 0$.

  At $D = 0$, T and S are non-negative, hence $D^{'} > 0$.

  At $T = 0$, D and S are non-negative, hence $T^{'} > 0$.

  Hence union of linear and nonlinear regimes is positive invariant.

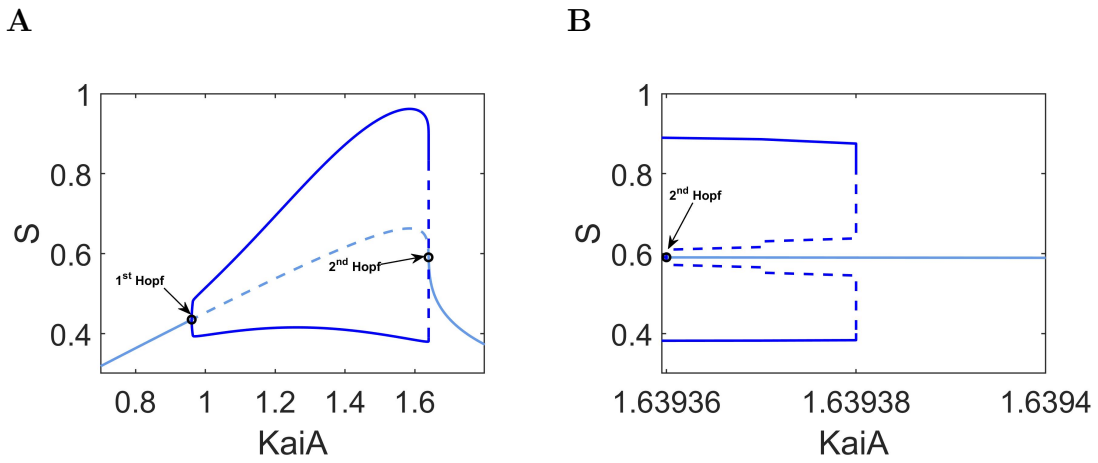

Figure 4.5 **A** Bifurcation diagram of the model with KaiA as a bifurcation parameter and **B** shows the magnification of **A** showing subcritical Hopf bifurcation and saddle node bifurcation of periodic orbits. For KaiA values less than ≈ 0.96, we have stable focus and the system evolves as a damped oscillator. Supercritical Hopf bifurcation occurs at KaiA ≈ 0.9606 giving rise to small amplitude stable oscillations. Subcritical Hopf bifurcation occurs at KaiA ≈ 1.63922. Global bifurcation (saddle node of periodic orbits) occurs at KaiA $= 1.63925$, where the stable and an unstable limit cycles become very closer to each other and annihilates the oscillations. Solid light blue denotes the stable fixed point, dashed light blue denotes an unstable fixed point, solid blue denotes stable limit cycle and dashed blue denotes an unstable limit cycle.

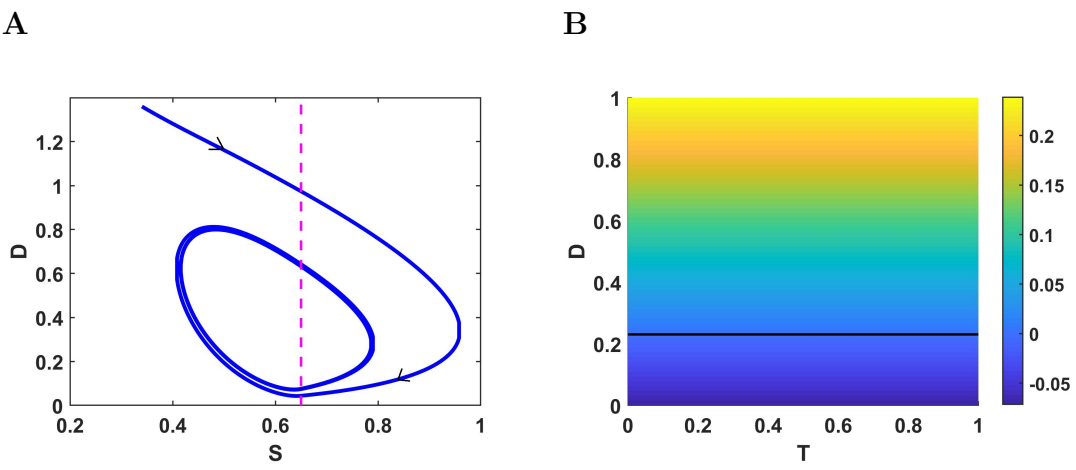

Figure 4.6 $S^{'}$ at $S = \dfrac{\text{KaiA}}{2m}$ for lower and higher D. **A** shows that for higher D, S is decreasing and for lower D, S is increasing. **B** Color map of $S^{'}$ in the TD plane. Horizontal line $D = 0.2306$ which corresponds to $S^{'} = 0$

- If a trajectory is in a nonlinear region, it can only leave through plane $P = \dfrac{[\text{KaiA}]}{2m}$.

Here we check $S^{'}$ at $S = \dfrac{[\text{KaiA}]}{2m} = 0.65$ ($[\text{KaiA}] = 1.3$, $m = 1$).

$$\frac{dS}{dt} = 0.31D - 0.0715 \tag{4.24}$$

In TD plane, $S^{'}$ doesnt depend upon T. For high D values, S is increasing and for lower D values, S is decreasing.

Mechanism of Oscillations

From the Rust point of view, the mechanism of having oscillations in the cyanobacterial clock model is the sequestration of KaiA by S-KaiC which promotes dephosphorylation and therefore increases the production of S-KaiC from ST-KaiC. S-KaiC is an autocatalytic as it increases its own production. This sequestration effect of KaiA by S-KaiC is the essential non-linearity in the RUST model and has been

determined to be sufficient enough, i.e. the switch between phosphorylation and dephosphorylation occurs over a sufficiently small range of active KaiA concentration [81]. Particularly, the source of nonlinearity is the parameter $K_{1/2}$ (the concentration of KaiA which causes a half-maximal effect on phosphorylation rates), which means the rates dependent on S. For $K_{1/2} = 0$, the rates are no more dependent on S, as the system becomes linear and the dynamics in this case approaches a stable steady state located at the origin. Range of $K_{1/2}$ for which oscillations have been observed is $0.092\mu M < K_{1/2} < 0.93\mu M$.

The mechanism of oscillations we hypothesize here is that, it constitites the switch between linear and nonlinear regimes (except for a very tiny region) and this switch has been observed as:

When $S < \frac{[KaiA]}{2m}$, we have $A = [KaiA] - 2mS$, the system settled into non-linear regime in which the system has an unstable fixed point and, as a result, the system approaches toward infinity until $S = \frac{[KaiA]}{2m}$.

As S crosses $\frac{[KaiA]}{2m}$, we have $A = 0$, and the system switches to the linear regime. In the linear regime, the system goes to zero steady-state until $S < \frac{[KaiA]}{2m}$.

So essentially, the oscillation mechanism in the Rust model is the switching of linear and nonlinear regimes except for a tiny range of KaiA (KaiA=0.961 to 0.9645) in which we have a small amplitude oscillation and the system remains in a nonlinear regime only. Figure 4.8 shows the tiny region where S stays below the threshold $\frac{[KaiA]}{2m}$.

Figure 4.7 shows how much time the limit cycle trajectory spends in the linear and nonlinear regimes for one period. It illustrates the three-dimensional trajectory (Figure 4.7) and its projection onto the D-S plane. Both figures show that during one cycle period, the trajectory spends more time in the nonlinear regime.

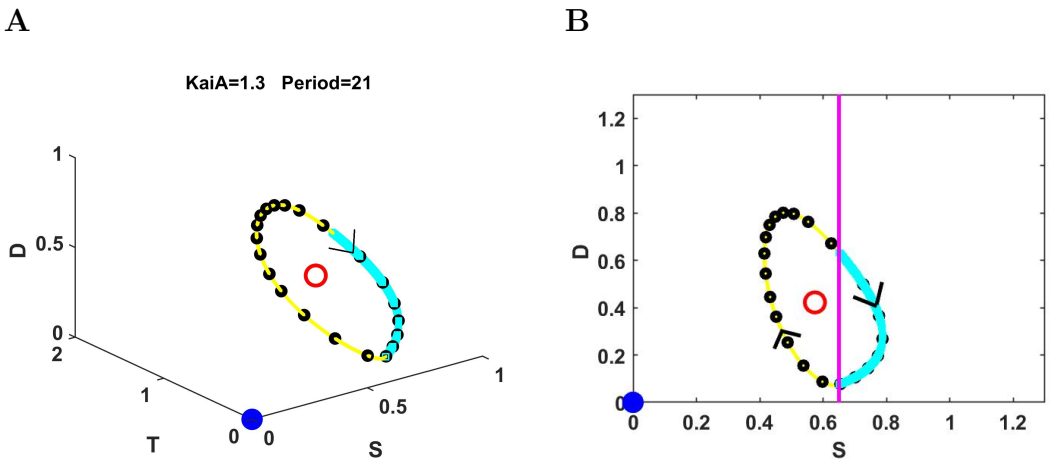

Figure 4.7 Three dimensional limit cycle trajectory in **A** with an hourly marked period in black. Yellow part of the trajectory corresponds to the nonlinear regime in which the system has unstable fixed point (red open) and cyan part is linear regime in which system goes to stable fixed point (blue filled). Besides this, trajectory spends more time in nonlinear regime. Two dimensional projection of trajectory in **B** on SD plane.

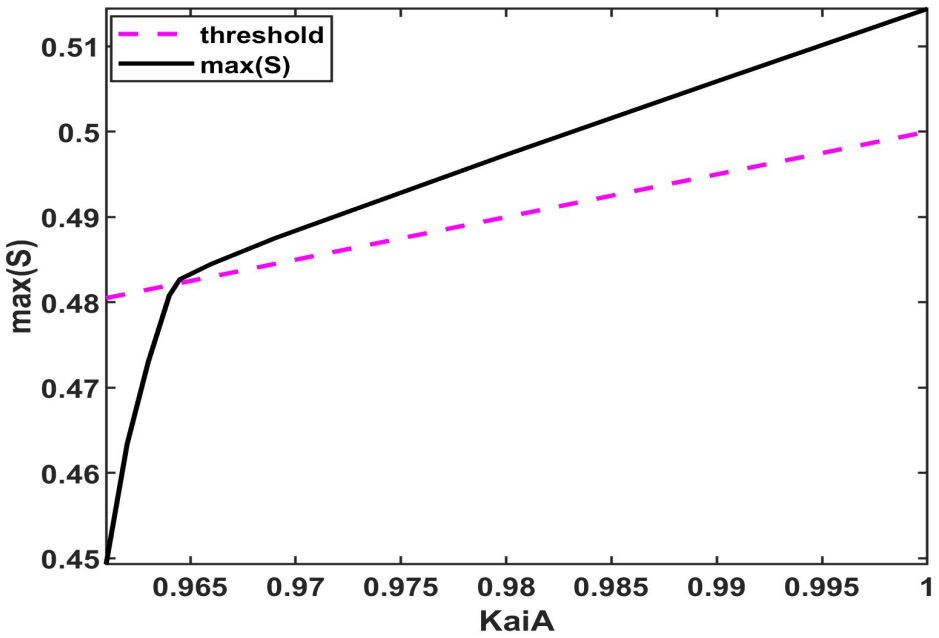

Figure 4.8 Tiny region (KaiA=0.961 to 0.9645) where oscillation occurs without switching into linear regime.

Switching Manifold: Figure 4.9 shows the switching manifold and how the trajectories move from one regime to another and give rise to limit cycle oscillations. To the right of switching manifold , the trajectories (in blue) approach toward the stable fixed point (a node) located at the origin, also called virtual fixed point. As the trajectory crosses the manifold, the system has an unstable fixed point (a saddle focus); hence, the trajectories (in red) move away from it along the unstable direction until it hits the switching manifold again and, as a result, an isolated periodic orbit (or limit cycle) is formed from the trajectories in the linear and nonlinear regimes. Figure 4.9 shows the formation of the 3D periodic orbit (left panel) and its 2D projection (right panel) obtained by the union of trajectories in linear and nonlinear regimes for various values of KaiA.

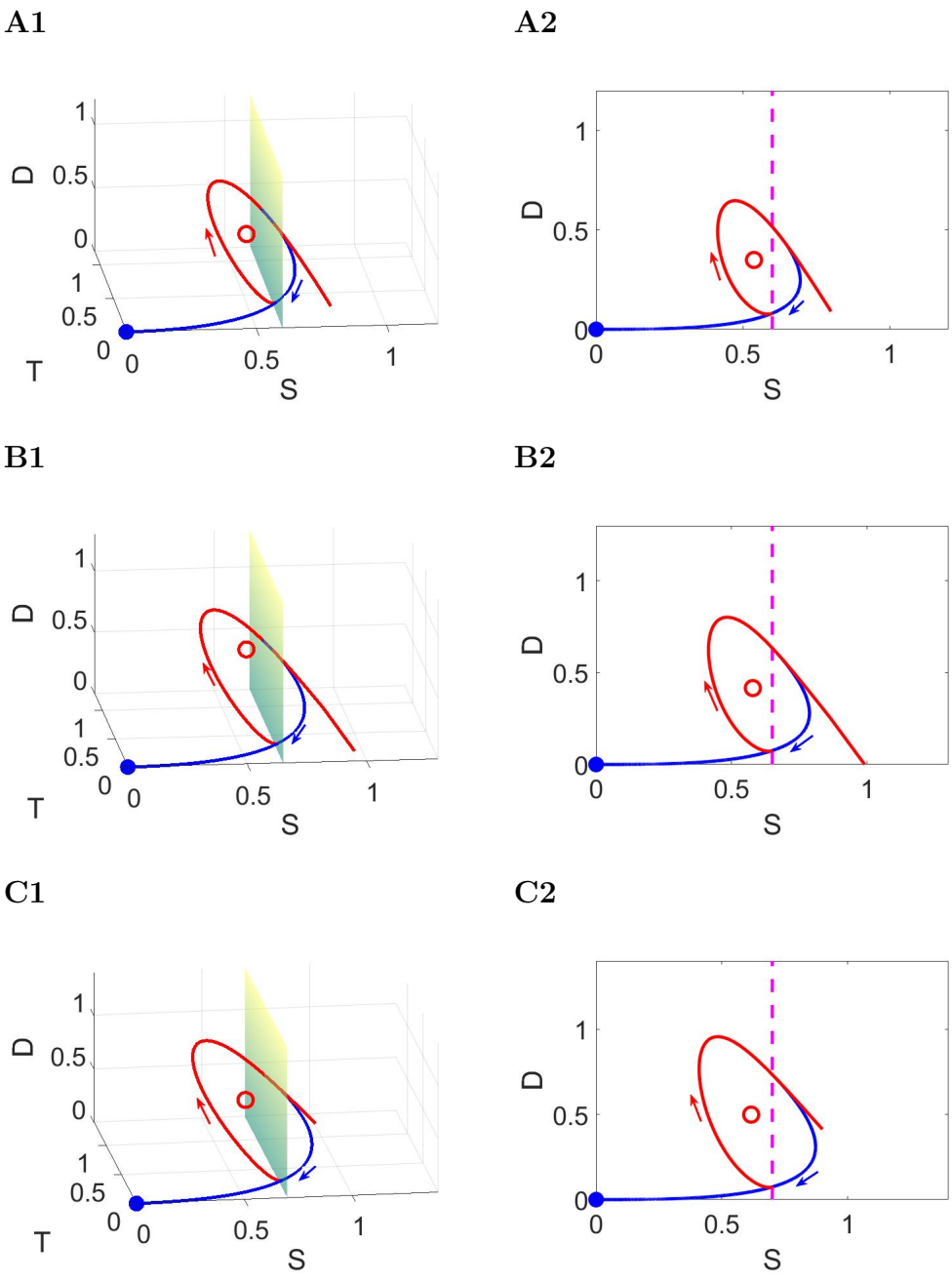

Figure 4.9 Top (KaiA=1.2), Middle (KaiA=1.3) and bottom (KaiA=1.4) panel switching between the linear regime and nonlinear regimes across the switching manifold (a plane) give birth to the limit cycle oscillations in S-T-D phase space (all left) and S-D plane (all right).

Linearized Dynamics in the Nonlinear Regime The Rust model produces an oscillation as a result of the interplay between linear and nonlinear dynamics. We would like to examine: if we linearize the nonlinear dynamics, can we get an oscillation? More specifically, can we have an oscillation as an interplay between two linear systems?

So in this section, we analyze the nonlinear regime in such a way that we linearize the system about an unstable fixed point in a nonlinear regime for some KaiA value and then check whether we obtain oscillations if we switch between two linear systems: one linear system corresponds to the linear regime and the second linear system obtained from the linearization process in nonlinear regime.

The Jacobian matrix for the nonlinear regime (as a function of KaiA and its corresponding fixed point) is given by:

$$\begin{bmatrix} R_{11} & R_{12} & R_{13} \\ \\ R_{21} & R_{22} & R_{23} \\ \\ R_{31} & R_{32} & R_{33} \end{bmatrix}$$

Entries of the Jacobian matrix are:

$$R_{11} = \frac{-0.7718A}{C} - 0.21,\ R_{12} = \frac{-0.3060A}{C},$$
$$R_{13} = \frac{-239500KaiA^2+(958000KaiA)S-102985KaiA-958000S^2+411940S+131580D+331874T-700298}{50B},$$
$$R_{21} = \frac{0.2130A}{B},\ R_{22} = \frac{0.1460A}{B} - 0.31,$$
$$R_{23} = \frac{-(-25300KaiA^2+(101200KaiA)S-10879KaiA-101200S^2+43516S+6278D+9159T)}{5B},$$
$$R_{31} = \frac{-0.0530A}{B},\ R_{32} = 0.31 - \frac{0.3720A}{B},$$
$$R_{33} = \frac{-53600KaiA^2+(2144000KaiA)S-277780KaiA-2144000S^2+921920S+319920D+45580T-175311}{100B}$$
and $A = KaiA - 2S$, $B = (100KaiA - 200S + 43)^2$, $C = KaiA - 2S + \dfrac{43}{100}$.

For example when KaiA=1.3, the fixed point is located at $(T, D, S) = (0.7602, 0.4161, 0.5782)$, the linear system in nonlinear regime is:

$$\frac{dT}{dt} = -0.4032(T - 0.7602) - 0.07661(D - 0.4161) - 1.786(S - 0.5782) \quad (4.25)$$

$$\frac{dD}{dt} = 0.05332(T - 0.7602) - 0.2734(D - 0.4161) - 1.22(S - 0.5782) \quad (4.26)$$

$$\frac{dS}{dt} = -0.01327(T - 0.7602) + 0.2169(D - 0.4161) + 0.4661(S - 0.5782) \quad (4.27)$$

The linear system (independent of KaiA) that corresponds to the linear regime is:

$$\frac{dT}{dt} = -0.21T \quad (4.28)$$

$$\frac{dD}{dt} = -0.31D \quad (4.29)$$

$$\frac{dS}{dt} = 0.31D - 0.11S \quad (4.30)$$

We simulate both linear systems in such way that we take linear system (Equations 19 to 21) when $S > \frac{KaiA}{2m}$ and linear system (Equations 16 to 18) when $S < \frac{KaiA}{2m}$.

We do get oscillations (Figure 4.10) as a result of an interplay between two linear systems with period ≈ 22.65 hours.

4.4 Dynamic Analysis of the Byrne Model

To understand the mechanism of oscillations in 2D, we also hypothesize as we did in the last section (for the 3D model) that the mechanism of oscillations in the 2D is generated by the transition between linear and nonlinear regimes of the model. To

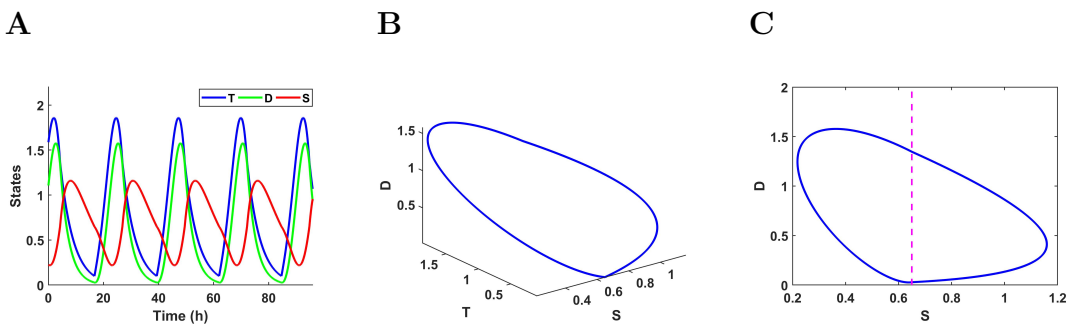

Figure 4.10 Oscillation from system of two linear systems: one linear system corresponds to linear regime and second is a linearized system corresponding to nonlinear regime. For KaiA=1.3: **A** Time course dynamics. **B** Trajectory in the phase space. **C** Projection of trajectory on SD plane.

analyze the mechanism of oscillations, we use dynamical system tools such as fixed point analysis, time course, bifurcation diagram and phase plane.

Fixed points Analysis

For fixed point analysis, we can rewrite the Byrne model in an alternative form (right-hand sides of the system as a sum of linear and nonlinear functions)

$$\frac{dx}{dt} = -k_{-1}x + k_{+1}(x,y)(1-x) \tag{4.31}$$

$$\frac{dy}{dt} = -k_{-2}y + k_{+2}(x,y)(1-y) \tag{4.32}$$

where

$$k_{+j} = k_{+j,max}\frac{E}{E+K} \tag{4.33}$$

and

$$E = max\{0, E_0 - y(1-x)\} \tag{4.34}$$

Fixed points have been calculated by using **fsolve** routine in MATLAB using different initial conditions and stability of the fixed points have been found by finding the eigenvalues of the Jacobin matrix evaluated at the fixed points.

Linear regime:

The model is in the linear regime when $E = 0$ (i-e when $y > \frac{E_0}{1-x}$). This regime doesnt have a fixed point as it is located at $(x^*, y^*) = (0, 0)$ which is located in the nonlinear regime, hence it is called a virtual fixed point. This fixed point is a stable node. The eigenvalues are $(-0.4, -0.78)$. The corresponding eigenvectors are: $v_1 = [1, 0]^T$ and $v_2 = [0.99, 0.04]^T$.

Non-linear regime:

The system has nonlinear dynamics for $y < \frac{E_0}{(1-x)}$. For $E_0 = 0.2$, two fixed points have been observed and both are unstable. At this value of KaiA, one of these fixed points has S coordinate to be $S < \frac{KaiA}{2m}$ and the other has $S > \frac{KaiA}{2m}$.

(a) First fixed point: This fixed point is located at $(x, y) = (0.23871, 0.23871)$ whose eigenvalues are (β_1, β_2), where $\beta_1 = 0.043315 + 0.30447i$ and $\beta_2 = 0.043315 - 0.30447i$. Thus, the fixed point is an unstable focus. We call this an actual fixed point as it is located in this regime.

The eigenvector matrix associated with these eigenvalues is :

$V_1 = (v_1, \overline{v_1})$ where $v_1 = [0.98844, 0.10408 - 0.1102i]^T$ and $\overline{v_1}$ is the complex conjugate of v_1.

(b) Second fixed point: This fixed point is located at $(x, y) = (0.6272, 0.79771)$ whose eigenvalues are $(\beta_1^{'}, \beta_2^{'})$, where $\beta_1^{'} = 0.2583$ and $\beta_2^{'} = 0$.

The eigenvector matrix associated with these eigenvalues is :

$V_2 = (v_2, v_3)$ where $v_2 = [0.9874, 0.1584]^T$ and $v_3 = [0.8789, 0.4771]^T$.

This fixed point is a virtual fixed point as it is located in the linear regime. Fixed points in the linear and nonlinear regimes describing the oscillation dynamics are shown in Figure 4.11.

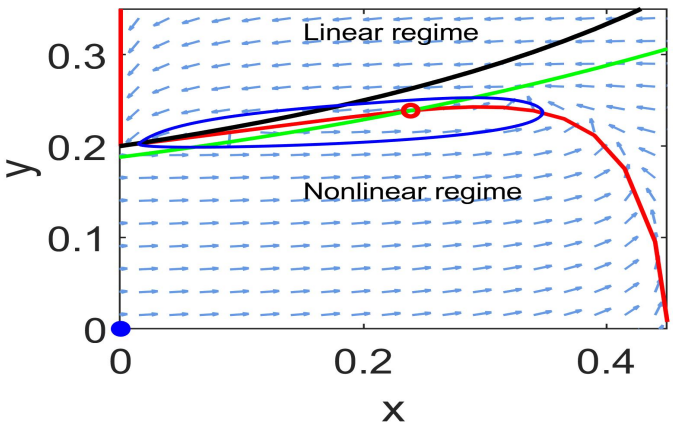

Figure 4.11 Phase plane showing virtual fixed point for the linear regime (blue filled dot) and actual fixed for the nonlinear regime (red open dot). The curve in black is the switching manifold above which the system has linear dynamics and below it has nonlinear dynamics. The curve in blue is a limit cycle trajectory. x-nullcline is the red curve and green curve is the y-nullcline.

Bifurcation diagram

For low E_0 values (less than ≈ 0.138), the system has stable fixed point. At around $E_0 = 0.1381$, the fixed point loses stability and subcritical Hopf bifurcation occurs. Another subcritical Hopf bifurcation occurs at $E_0 \approx 0.2295$. Near to the first Hopf, saddle node bifurcation of periodic orbits occurs at $E_0 \approx 0.137$. Near to second Hopf, saddle node bifurcation of periodic orbits occurs at $E_0 \approx 0.2376$. The bifurcation diagram is shown in Figure 4.12.

Trajectory behaviour in the Byrne model

If a trajectory is in a nonlinear region, it can only leave through curve $y = \dfrac{E_0}{1-x}$. We see in the Figure 4.13 that for higher values of y, x is increasing and for low values of y, x is increasing.

Mechanism of Oscillations

The mechanism of oscillations we hypothesize here is that it switches between linear and nonlinear regimes. This switch has been observed as the following:

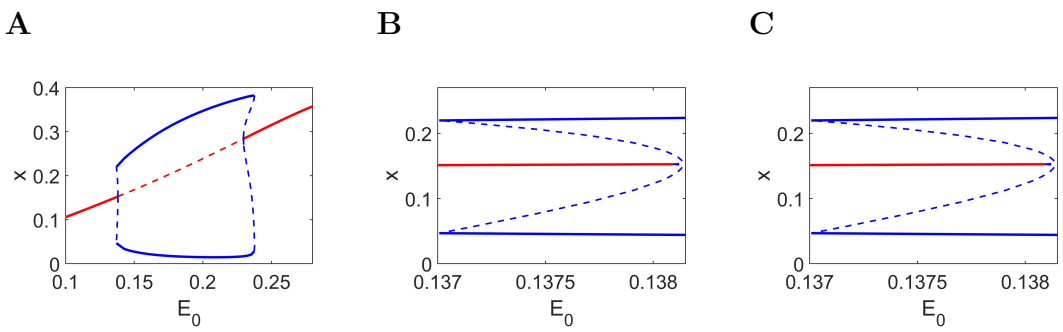

Figure 4.12 Bifurcation diagram of the model with E_0 as a bifurcation parameter in **A**. 1st Hopf subcritical bifurcation occurs at $E_0 \approx 0.1381$) and 2nd Hopf subcritical bifurcation occurs at $E_0 \approx 0.2295$). **B** and **C** shows the bistability regions which are the magnifications of near first Hopf and second Hopf point, respectively. Solid red lines represent the stable fixed point, dashed red line denotes the unstable fixed point, solid blue lines the maximum and minimum of stable limit cycle, dashed blue lines represent the maximum and minimum unstable limit cycle.

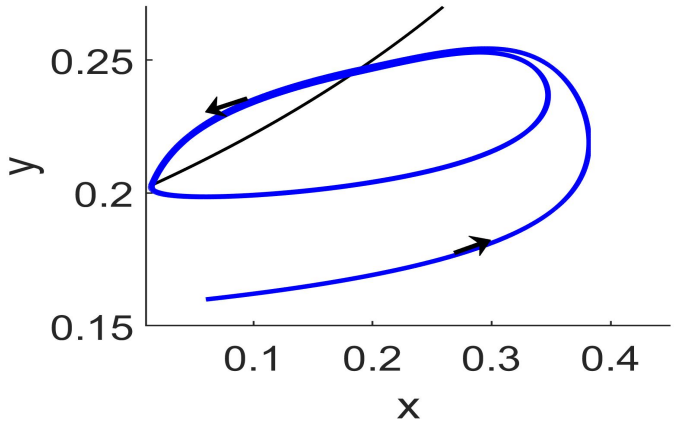

Figure 4.13 Trajectory in phase plane showing that for higher y, x is decreasing and for low y values, x is increasing.

when $y < \dfrac{E_0}{1-x}$, we have $E = E_0 - y(1-x)$, the system settled into a non-linear regime in which the system has an unstable fixed point; as a result, the system approaches toward infinity until it hits the switching curve.

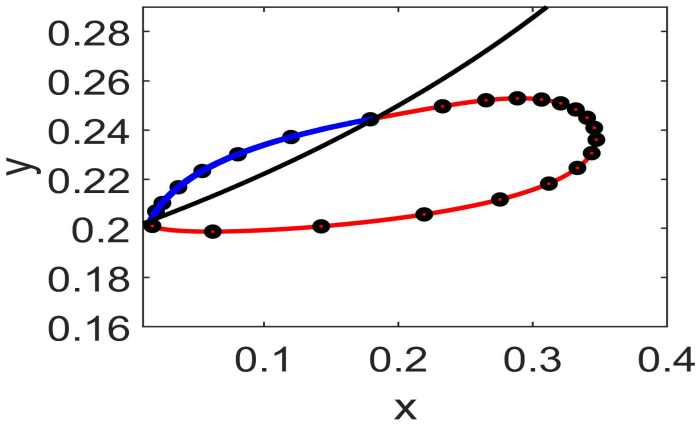

Figure 4.14 Limit cycle trajectory for $E_0 = 0.2$ with an hourly time period marked in black dots. Red part of the trajectory corresponds to the nonlinear regime (the system has unstable fixed point) and blue part corresponds to the linear regime (the system goes to stable fixed point). The trajectory spends more time in nonlinear regime. In linear regime, trajectory spends $\approx$ 7 h and in nonlinear regime, the trajectory spends $\approx$ 17 h.

As y crosses the switching curve, we have $E = 0$, and the system switches to the linear regime. In the linear regime, the system goes to zero steady-state until it hits the switching curve.

Figure 4.14 shows how much time the limit cycle trajectory spends in linear and nonlinear regimes for one period. We see that the trajectory spends more time in the nonlinear regime.

Linearized Dynamics in the Nonlinear Regime

In this section, we would like to see if we get oscillations if we have two linear systems: one is in the linear regime and the second one is the linearized system in a nonlinear regime about an unstable fixed point.

The Jacobian matrix for the nonlinear regime (as a function of E_0 and its corresponding fixed point) is given by:

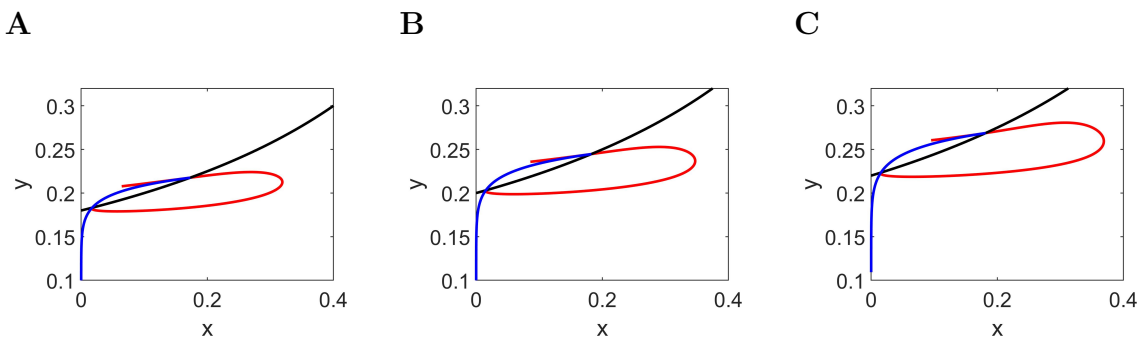

Figure 4.15 Limit cycle trajectory formation from the trajectory switching across linear and nonlinear regimes for different values of E_0. Trajectory in blue corresponds to the linear regime and trajectory in red corresponds to the nonlinear regime. Curve in black is the switching manifold. **A** $E_0 = 0.18$, **B** $E_0 = 0.2$ and **C** $E_0 = 0.22$.

$$\begin{bmatrix} B_{11} & B_{12} \\ \\ B_{21} & B_{22} \end{bmatrix}$$

Entries of the Jacobian matrix are:

$$B_{11} = \frac{-2(1250E_0^2+2500E_0xy-2500E_0y+75E_0+\beta-\gamma+1250y^2+100xy-100y+1)}{5\alpha},$$
$$B_{12} = \frac{-10(x-1)^2}{\alpha},\ B_{21} = \frac{-3y(y-1)}{4\alpha},$$
$$B_{22} = \frac{-3(1250E_0^2+2500E_0xy-2500E_0y+75E_0+\beta-\gamma+1250y^2+100xy-100y-25x+26}{100\alpha}$$

and $\alpha = (25E_0 - 25y + 25xy + 1)^2$, $\beta = 1250x^2y^2$, $\gamma = 2500xy^2$.

For example, for $E_0 = 0.2$, the fixed point is located at $(x, y) = (0.23871, 0.23871)$, the linear system in nonlinear regime is:

$$\frac{dx}{dt} = 0.3308(x - 0.23871) - 2.731(y - 0.23871) \tag{4.35}$$

$$\frac{dy}{dt} = 0.06422(x - 0.23871) - 0.2442(y - 0.23871) \tag{4.36}$$

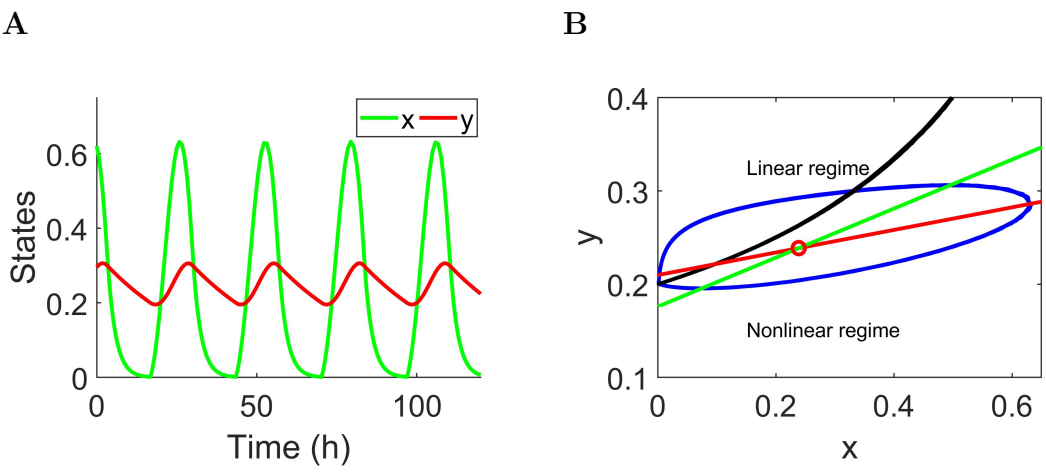

Figure 4.16 Oscillation from two linear systems: One corresponds to the linear regime and second is the linearised system related to nonlinear regime. Time course dynamics in **A** and phase plane dynamics in **B** for $E_0 = 0.2$. Period is ≈ 26 h. In **B**, x-nullcline is shown in the red, y-nullcline in green, trajectory in blue. Threshold is shown in black and fixed point located at $(0.23871, 0.23871)$ denoted by red open dot.

The linear system (independent of E_0) that corresponds to the linear regime is:

$$\frac{dx}{dt} = -0.4x \tag{4.37}$$

$$\frac{dy}{dt} = -0.03y \tag{4.38}$$

We simulate both linear systems in such a way that we take linear system (Equations 29 and 30) when $y > \dfrac{E_0}{1-x}$ and linear system (Equations 27 and 28) when $y < \dfrac{E_0}{1-x}$.

We do get oscillations as a result of an interplay between two linear systems (Figure 4.16) with a period of ≈ 22.65 hours.

4.5 Period of Oscillations in Rust/Byrne Models Versus Experiments

In the Rust model, increasing KaiA concentration lengthens the period of oscillations (Figure 4.17 A). In the Byrne model, by increasing E_0, the period also increases (Figure 4.17 B). So, in both models, the period increases as the protein concentration (KaiA in Rust and E_0 in Byrne) increases. However, Kageyama [46] reported experimental data on the behaviour of the oscillator which shows that increasing KaiA concentration shortens the period of oscillations. Experiments by Yong-Ick Kim also showed that reducing the KaiA concentration lengthens the period of oscillations (Figure 4.17 C).

Figure 4.17 A and B shows that the period increases as KaiA (Rust model) and E_0 (Byrne model) increase. In the linear regime, control parameters KaiA and E_0 have no apparent effect on the period. The period increase effect comes from the nonlinear regimes. Also, in previous sections, we have observed that in both Rust and Byrne model, we also get oscillations if we have two linear systems: one linear system corresponds to the linear regime and the second linear system corresponds to the linearized system in the nonlinear regime. With this, we investigate the effect of KaiA and E_0 on the eigenvalues in nonlinear regimes. We would like to see if eigenvalues could tell us something about the period increase in these models. In this regard, we would like to see the KaiA effect on eigenvalues in the Rust model and E_0 effect on eigenvalues in the Byrne model.

KaiA Effect on Eigenvalues in the Rust Model

Since KaiA doesn't affect the linear dynamics (as A=0), so virtual fixed point is not affected by the change in KaiA concentration. However, KaiA does affects the nonlinear dynamics.

In the nonlinear regime, we analyze the eigenvalues of an unstable fixed point as we increase KaiA concentration in the range for which we have oscillatory behaviour.

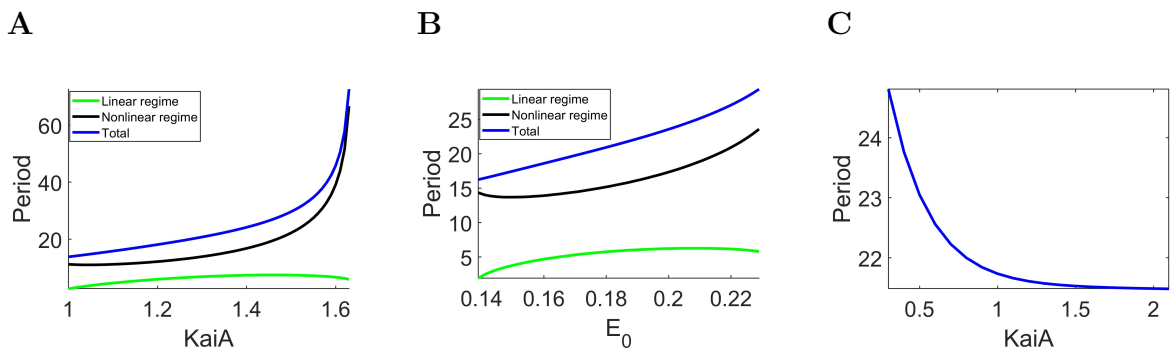

Figure 4.17 **A** shows the period of oscillations in the Rust model in linear regime (green), nonlinear regime (black) and total (blue). **B** shows the period of oscillations in the Byrne model in linear regime (green), nonlinear regime (black) and total (blue). **C** Period fit to experimental data from Yong-Ick's Lab.

As we increase KaiA concentration, the real eigenvalues (which are negative) becomes more negative (Figure 4.18 A). On the other hand, as we increase KaiA, the imaginary part of eigenvalues decreases (Figure 4.18 B).

By looking at the real and imaginary parts of an unstable fixed point, can we get insight into what role they play in the period increase as we increase KaiA? By looking at Figure 4.18 A, we see that for two different KaiA values (say KaiA=1.2 and KaiA=1.6), the real parts are almost the same. Hence, the real parts do not play any role in the period increase as KaiA increases. It is, therefore, the imaginary part of an eigenvalue which plays the role in the period increase as KaiA increases.

E_0 effect on Eigenvalues in the Byrne Model

Figure 4.19 shows the effect of E_0 on the real and imaginary parts of the fixed point in nonlinear regime. We have seen both in the Rust and Byrne models that when we increase KaiA in Rust and E_0 in the Byrne model, the period increases. So what makes the period increase as we increase $KaiA$ in Rust or E_0 in the Byrne model? If we look at Figure 4.19, it shows that for two different E_0 values, their corresponding

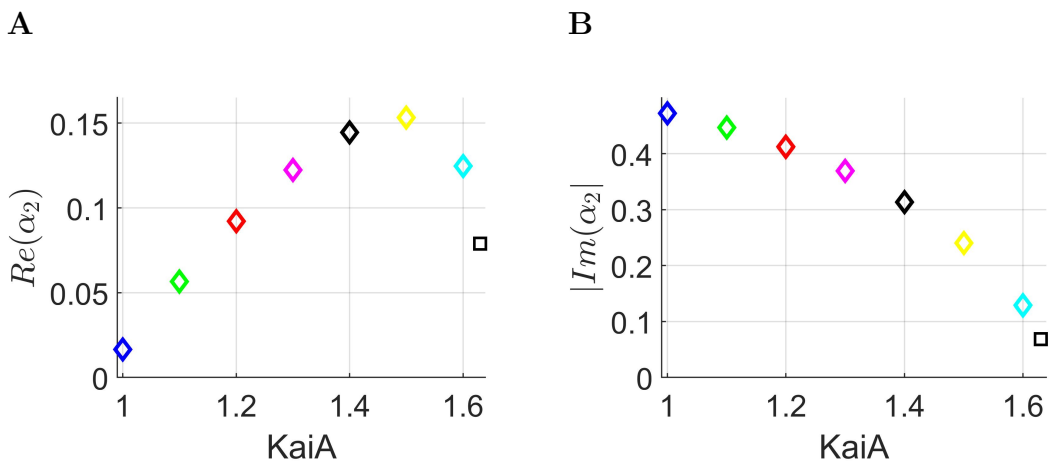

Figure 4.18 Real (**A**) and imaginary part (**B**) of an unstable fixed point during the course of oscillations versus the parameter KaiA.

real parts are approximately equal, while their imaginary parts are quite different. Hence, it must be the imaginary part of the fixed point which plays the role. As we increase E_0, the imaginary part decreases, which means that the frequency of oscillations decreases, or, equivalently, the period of oscillations increases.

From the Figures 4.18 and 4.19 describing the results of KaiA and E_0 on the eigenvalues of the unstable fixed point in nonlinear regime of the Rust and Byrne models, we observed that the imaginary part of the eigenvalues has a noticeable effect on the period behavior. For both models, the imaginary part decreases as we increase the control parameters. Decrease in the imaginary part means a decrease in the frequency of oscillations, which is equivalent to an increase in the period of oscillations.

Future work: To obtain the right period behavior as observed in experimental findings, modifications in the Rust or Byrne could be made such that imaginary part of eigenvalues for an unstable fixed point in nonlinear regime increases as we increase KaiA (in Rust's model) or E_0 (in Byrne's model).

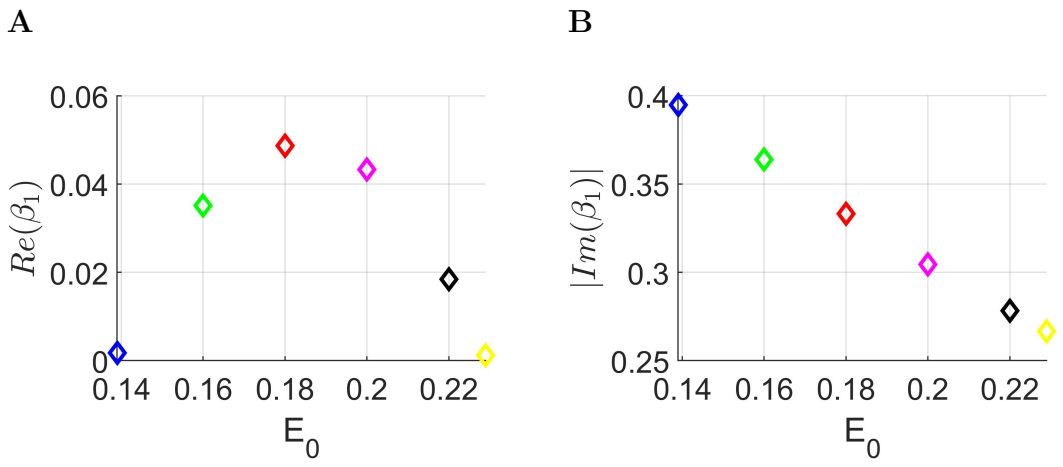

Figure 4.19 Effect of E_0 on the real (**A**) and imaginary part (**B**) of an unstable fixed point during the course of oscillations.

CHAPTER 5

ENTRAINMENT RESPONSES IN CIRCADIAN CLOCK MODELS

5.1 Introduction

In this Chapter, we show how time dependent period forcing is incorporated in the Rust and Byrne Models. Section 5.2.1 shows a periodically forced Rust Model. Forcing has affect on the phosphorylation rates. Section 5.2.2 presents a periodically forced Byrne Model which shows that forcing affect fast reaction kinetics.

In this section, results for the Rust and Byrne Models focuses on two directions. One direction focuses on the system's intrinsic dynamics (the effect of forcing on fixed point(s) of the system) when the forcing turns on and the second direction focuses on the entrainment results. In section 5.3, for a cycle of forcing, we use fixed points analysis when the forcing turns on. Section 5.3 shows entrainment results when an unforced system has different qualitative behaviours. Section 5.4 shows dynamic analysis of the forced Byrne Model. Section 5.4 shows the entrainment results and the corresponding phase plane pictures for the Byrne Model.

5.2 Circadian Clock Models with Periodic Forcing

5.2.1 Periodically Forced Rust Model

In the cyanobacterial circadian clock model, the KaiABC proteins that comprise the core oscillator [75] are directly sensitive to metabolites (acting as zeitgebers). Two important signals which cause clock phase shifts are ATP/ADP ratios and oxidized quinones, and both serve as a proxy for darkness [51].

Light-dark pulses brings a phase shift in the cyanobacterial clock [51, 80]. In subsection 3.1, we explored the dynamics of cyanobacteria with no forcing (constant light conditions) where decomposition has already been studied in linear and nonlinear

regimes and how the switch dynamics between linear and nonlinear regimes result in oscillations.

In this section, we would like to investigate the dynamics of cyanobacteria in response to light-dark cycles, in particular, when subject to one of the metabolic processes, here ATP/ADP. We used square-wave with a fixed photoperiod to represent ATP/ADP.

The Rust version of forcing is described by the following differential equations:

$$\frac{dT}{dt} = k_{UT}(S)U + k_{DT}(S)D - k_{TU}(S)T - k_{TD}(S)T$$

$$\frac{dD}{dt} = k_{TD}(S)T + k_{SD}(S)S - k_{DT}(S)D - k_{DS}(S)D$$

$$\frac{dS}{dt} = k_{US}(S)U + k_{DS}(S)D - k_{SU}(S)S - k_{SD}(S)S$$

$$k_{phos}(S) = k^0_{phos} + \frac{[ATP]}{[ATP]+[ADP]}\frac{k^A_{phos}A(S)}{K_{1/2}+A(S)}$$

$$k_{dephos}(S) = k^0_{dephos} + \frac{k^A_{phos}A(S)}{K_{1/2}+A(S)}$$

$$A = max\{0, [KaiA] - 2mS\}$$

For $[ADP] = 0$, this corresponds to the unforced model (i.e. in constant light conditions.). We study the effect of time dependent forcing on the model dynamics, thereby modifying the above model by incorporating the time-dependent forcing as:

$$\frac{dT}{dt} = k_{UT}(S)U + k_{DT}(S)D - k_{TU}(S)T - k_{TD}(S)T$$

$$\frac{dD}{dt} = k_{TD}(S)T + k_{SD}(S)S - k_{DT}(S)D - k_{DS}(S)D$$

$$\frac{dS}{dt} = k_{US}(S)U + k_{DS}(S)D - k_{SU}(S)S - k_{SD}(S)S$$

$$A = max\{0, [KaiA] - 2mS\}$$

$$k_{phosph} = k^0_{phosph} + (1 - \alpha f(t)) \frac{k^A_{phosph} A(S)}{K_{1/2} + A(S)}$$

$$k_{dephos} = k^0_{dephos} + \frac{k^A_{dephos} A(S)}{K_{1/2} + A(S)}$$

$$k^0_{phosph} = [k^0_{UT} \;\; k^0_{TD} \;\; k^0_{SD} \;\; k^0_{US}] \;, \qquad k^A_{phosph} = [k^A_{UT} \;\; k^A_{TD} \;\; k^A_{SD} \;\; k^A_{US}]$$
$$k^0_{dephosph} = [k^0_{TU} \;\; k^0_{DT} \;\; k^0_{DS} \;\; k^0_{SU}] \;, \qquad k^A_{dephosph} = [k^A_{TU} \;\; k^A_{DT} \;\; k^A_{DS} \;\; k^A_{SU}].$$

f(t): square-wave (with fixed duty cycle and 24-hour period) with $f = 0$ is lights on and $f = 1$ is lights off. $\alpha = 1/3$ is the amplitude of forcing, corresponds to ADP=0.5.

5.2.2 Periodically Forced Byrne Model

In the Byrne Model, the external perturbation (light-dark pulses, temperature etc) interacts with the fast component dynamics (e.g., k_{+1}) [12].

With this, the periodically forced Byrne Model is:

$$\frac{dx}{dt} = (1 - \alpha f(t))\, k_{+1}(x, y)(1 - x) - k_{-1}x \tag{5.1}$$

$$\frac{dy}{dt} = k_{+2}(x, y)(1 - y) - k_{-2}y \tag{5.2}$$

$$E = max\{0, E_0 - y(1 - x)\} \tag{5.3}$$

$$k_{+j} = k_{+j,max} \frac{E}{E + K} \tag{5.4}$$

f(t): square wave (with fixed duty cycle and 24-hour period).

5.3 Entrainment Analysis of the Forced Rust Model

First, we analyze the linear and nonlinear regimes of the model without periodic forcing where the forcing is constantly off or constantly on.

Dynamics with Forcing Constantly Off ($\alpha = 0$)

This corresponds to the model in constant light conditions (forcing is off) which is the original mode about which analysis has been done in the previous chapter. Just to recall that for this case, we have two fixed points: a stable fixed point in the linear regime and an unstable fixed point in the nonlinear regime.

Dynamics with Forcing Constantly On ($\alpha = 1/3$)

Now we take the case when forcing is on. We consider the case when the ratio ATP/ADP is lowered to 50%. For 50% ADP, the strength of the dark pulse would be $\alpha = 1/3$. In this case the system takes this form:

$$\frac{dT}{dt} = k_{UT}(S)U + k_{DT}(S)D - k_{TU}(S)T - k_{TD}(S)T$$

$$\frac{dD}{dt} = k_{TD}(S)T + k_{SD}(S)S - k_{DT}(S)D - k_{DS}(S)D$$

$$\frac{dS}{dt} = k_{US}(S)U + k_{DS}(S)D - k_{SU}(S)S - k_{SD}(S)S$$

$$A = max\{0, [KaiA] - 2mS\}$$

$$k_{phosph} = k^0_{phosph} + \frac{2}{3}\frac{k^A_{phosph}A(S)}{K_{1/2} + A(S)}$$

$$k_{dephos} = k^0_{dephos} + \frac{k^A_{dephos}A(S)}{K_{1/2} + A(S)}$$

Linear Regime: The above model is in the linear regime when $A = 0$, which corresponds to the case when $S \geq 0.65$. In the linear regime, the fixed point is located at $(T^*, D^*, S^*) = (0, 0, 0)$ and it is stable node. The eigenvalues are $(-0.21, -0.31, -0.11)$.

Non-Linear Regime: In the non-linear regime, the system has two fixed points for $KaiA = 1.3$. The first fixed point (T_1^*, D_1^*, S_1^*) is located at $(T, D, S) = (0.7432, 0.3770, 0.5385)$ whose eigenvalues are $(-0.4437, -0.0314+0.27441i, -0.0314-0.27441i)$. This fixed point is classified as a stable focus. The second fixed point (T_2^*, D_2^*, S_2^*) is located at $(T, D, S) = (-3.8606, 0.2486, 0.6968)$ whose eigenvalues are $(0.7840, -0.6242+0.1718i, -0.6242-0.1718i)$. This fixed point is classified as a spiral index 1, with a stable spiral in two of the dimensions and unstable in the dimension perpendicular to the spiral surface. This second fixed is biologically not reasonable as the T component is negative.

Figure 5.1 showing the forced trajectory in phase plane. It also shows the time it takes for the trajectory into linear and nonlinear regimes when lights are on and off. It shows that the trajectory spends more time in nonlinear regime when lights are on or off while spends less time in linear regime when lights are on or off. Another important dynamics we observed is that, when the forcing turns on, the unstable fixed point stabilizes. The arrows (black when forcing is off and red when forcing is on) denote the orientation of the trajectory as it is evolving.

Note: It would be interesting to see whether forcing in the Byrne Model also has similar dynamics (stabilization of fixed point when forcing turns on) as we see here for the Rust Model, or not.

Periodic Forcing

For the square-wave periodic forcing, we investigate entrainment properties (monoglot and polyglot entrainment responses) for different KaiA values corresponding to

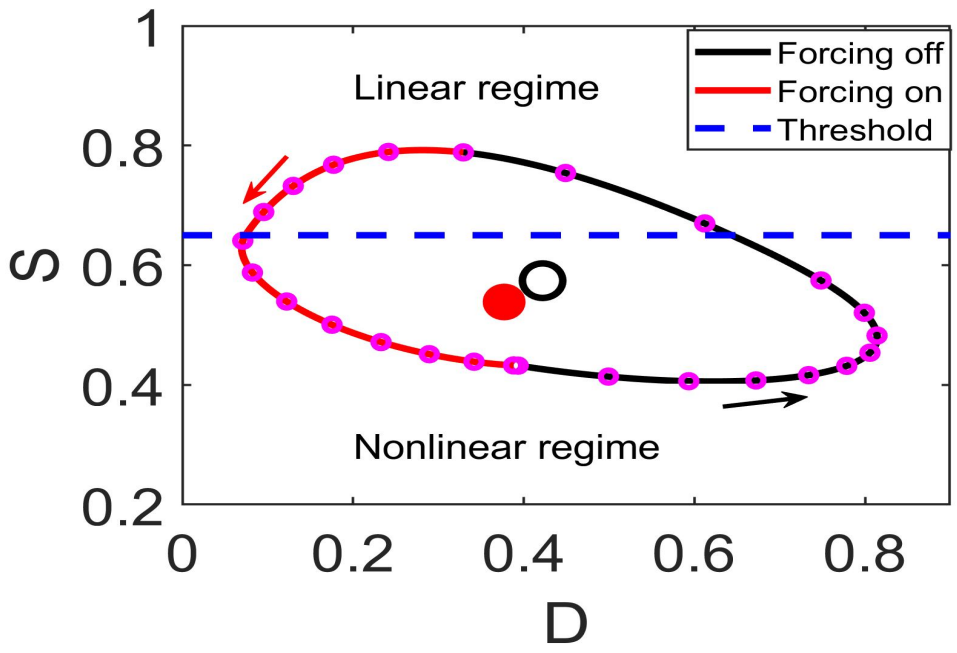

Figure 5.1 For the forced Rust Model, trajectory under the forcing in linear and nonlinear regimes which shows the unstable fixed point in linear regime stabilizes when forcing is on.

different fixed point behaviour. In the Rust Model, taking the periodic forcing for different KaiA values in the unforced system corresponding to different dynamics, we only observed monoglot structure. We show three cases of KaiA vales: KaiA value for which we have sustained oscillations, KaiA value for which we have damped oscillations and fixed point lies in the vicinity of supercritical Hopf bifurcation and KaiA value, for which we have damped oscillations and the fixed point lies in the vicinity of subcritical Hopf bifurcation. We term oscillations as subthreshold if the difference of peak and trough of the wave is smaller than 0.001.

Unstable Focus-Node with sustained oscillations for an unforced System

In this case, we take KaiA = 1.395, for which we have sustained oscillations with a period of 24 hours. The fixed point is a saddle focus of index 2. In this case, a typical Arnold tongue is observed as shown in the Figure 5.2 A1. Inside the tongue, we have

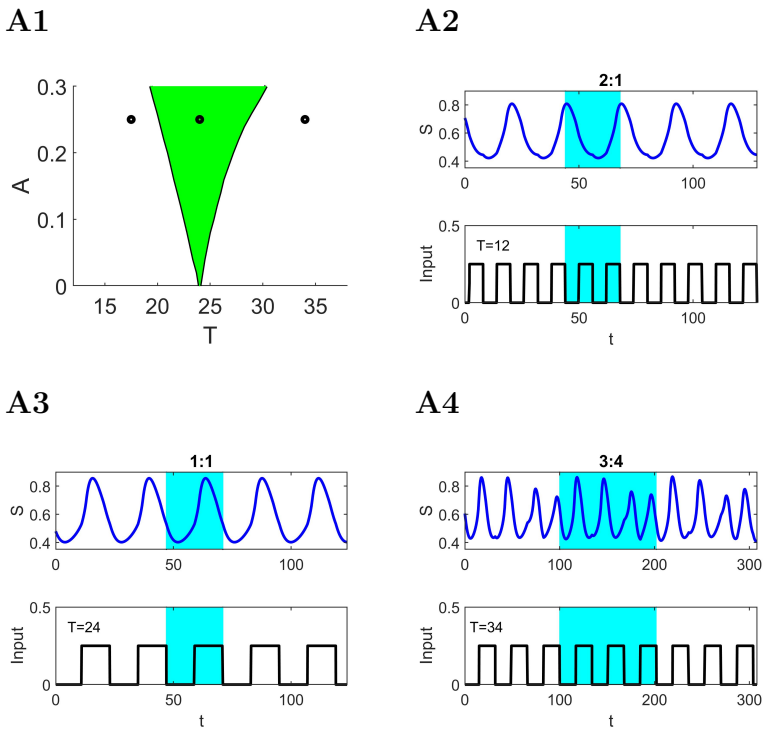

Figure 5.2 Representative entrainment patterns and Arnold tongue with monoglot structure for the Rust Model in response to square-wave forcing when an unforced system has sustained oscillations of period 24 h (KaiA = 1.395). **A1.** Arnold tongue showing 1:1 entrainment regions (highlighted in green). **Remaining panels.** Time courses for the state variable S and the forcing signal for the values of T and A indicated in A1 (black markers).

1:1 entrainment and outside entrainment breaks down. The black markers denote the values of the forcing parameters A and T for which the time course dynamics are shown in the remaining panels showing $2:1$ responses for $T = 12$, $1:1$ responses for $T = 24$ and $3:4$ responses for $T = 34$. The width of the Arnold tongue increases as A increases, which means that for a higher A, responses are entrained easily.

Stable Focus for an unforced System in the vicinity of Hopf bifurcation

In this case, we take KaiA $= 0.94$, for which the fixed point is located in the vicinity of Hopf bifurcation and we have damped oscillations. We didn't find polyglot entrainment responses even in this case, although unforced system has weakly damped oscillations. For fixed $A = 0.15$, and different T, entrainment responses are shown

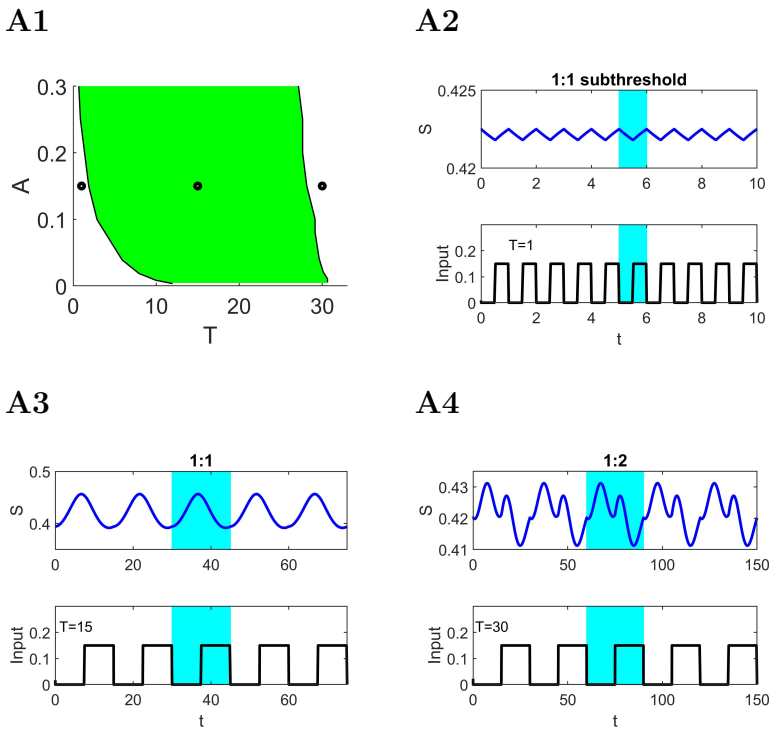

Figure 5.3 Representative entrainment patterns and Arnold tongue with monoglot structure for the Rust Model in response to square-wave forcing when an unforced system has stable focus in the vicinity of supercritical hopf bifurcation (KaiA = 0.94). **A1.** Arnold tongue showing 1:1 entrainment regions (highlighted in green). **Remaining panels.** Time courses for the state variable S and the forcing signal for the values of T and A indicated in A1 (black markers).

in the Figure 5.3. We call a wave an oscillation if threshold=0.001 from the peak of a wave to the trough. For very low T values, such as $T = 1$, we see low amplitude 1:1 oscillations, which we term as 1:1 subthreshold. For intermediate T values, such as $T = 15$, we see a rapid increase in the amplitude of oscillations and they are 1:1. For $T = 20$, the amplitude of oscillations is lowered and we have 1:1 responses. Increasing further T create some wiggle. These wiggles intensify upon further increase in T and multiple-peaked waveforms are observed for higher T as shown in Figure 5.3 A4 ($T = 30$), resulting in the breaking of 1:1 entrainment.

Stable Node for an unforced System In this case, we consider KaiA = 2, for which we have a stable node. The fixed point lies to the right of the subcritical Hopf

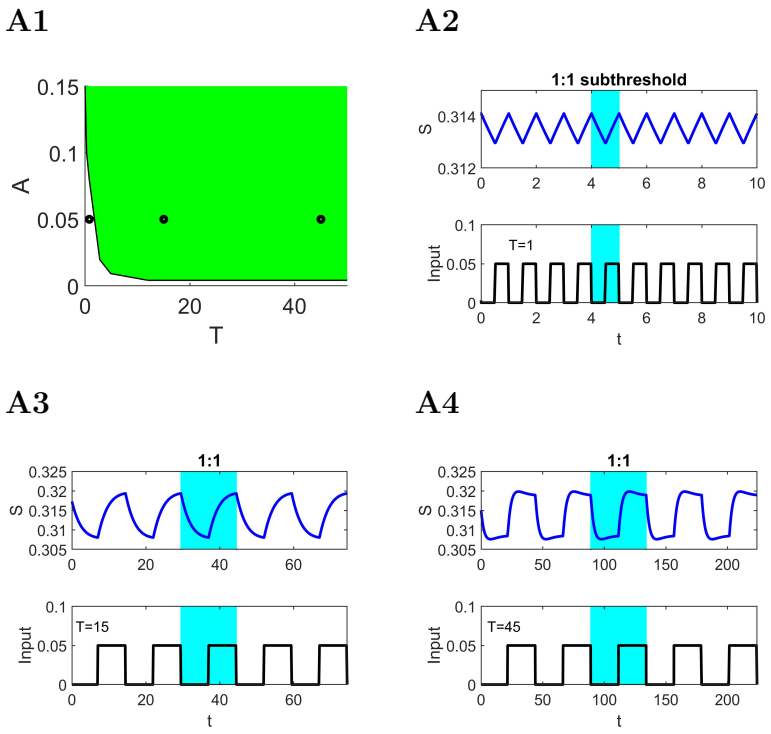

Figure 5.4 Representative entrainment patterns and Arnold tongue with monoglot structure for the Rust Model in response to square-wave forcing when an unforced system has stable node (KaiA = 2). **A1.** Arnold tongue showing 1:1 entrainment regions (highlighted in green). **Remaining panels.** Time courses for the state variable S and the forcing signal for the values of T and A indicated in A1 (black markers).

bifurcation. For a stable node, entrainment properties are more robust as entrainment does not break for higher period values shown in the Figure 5.4. In the stable node case, robust oscillations are formed by two stable steady states. Particularly, when forcing turns off, the trajectory settled on one stable steady state. When forcing turns on, trajectory settled on second stable steady state. These two stable steady states become the falling and rise phases of oscillations.

5.4 Entrainment Analysis of the Forced Byrne Model

First, we analyze the linear and nonlinear regimes of the Byrne Model without periodic forcing, but where the forcing is constantly off or constantly on.

Dynamics with Forcing Constantly Off ($\alpha = 0$) This corresponds to the model in constant light conditions (forcing is off) which is the unforced Byrne mode about which analysis has been done. Just to recall that for this case, we have three fixed points: one fixed point in the linear regime which is stable, and two unstable fixed points in the nonlinear regime in which one is hyperbolic and the second is non-hyperbolic.

Dynamics with Forcing Constantly On ($\alpha = 1/3$) Now we take the case when forcing is on. We take the case when the ratio ATP/ADP is lowered to 50% just like we did in the periodically forced Rust Model. For 50% ADP, the strength of the dark pulse would be $\alpha = 1/3$. In this case the system takes this form:

$$\frac{dx}{dt} = \frac{2}{3}k_{+1}(x, y)(1 - x) - k_{-1}x \tag{5.5}$$

$$\frac{dy}{dt} = k_{+2}(x, y)(1 - y) - k_{-2}y \tag{5.6}$$

$$E = max\{0, E_0 - y(1 - x)\} \tag{5.7}$$

$$k_{+j} = k_{+j,max}\frac{E}{E + K} \tag{5.8}$$

Linear Regime: The above model is in the linear regime when $A = 0$ which corresponds to the case when $y \geq \dfrac{E_0}{1 - x}$. In the linear regime, the fixed point is located at $(x^*, y^*) = (0, 0)$ and it is stable node. The eigenvalues are $(-0.4, -0.78)$.

Non-Linear Regime: In the non-linear regime when forcing is on, the system has two fixed points. The first fixed point (x^*, y^*) is located at $(x, y) = (0.1574, 0.2188)$ whose eigenvalues are $(-0.0659 + 0.3329i, -0.0659 - 0.3329i)$. This fixed point is classified as a stable focus.

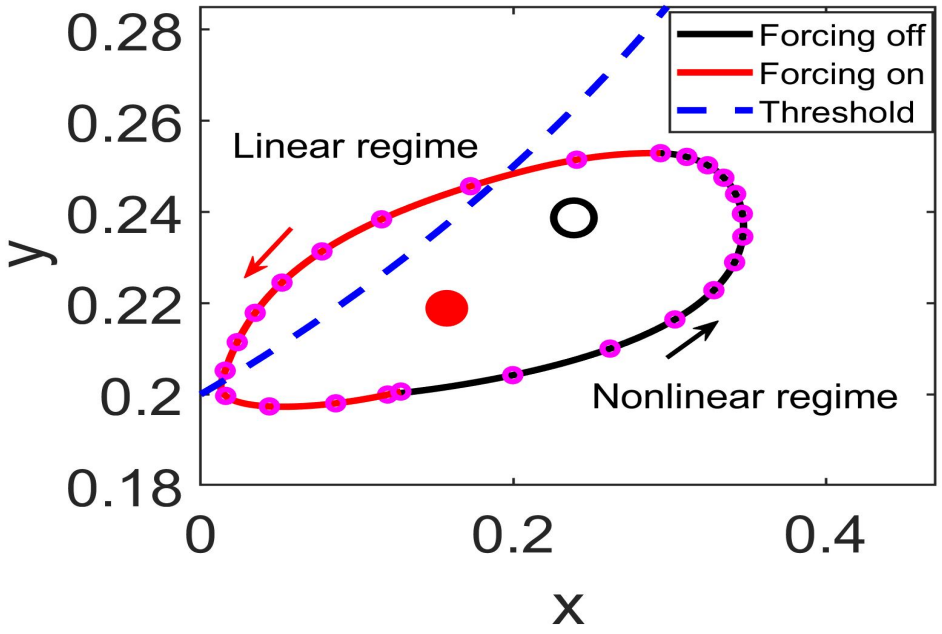

Figure 5.5 Byrne's Model trajectory under the forcing in linear and nonlinear regimes which shows the unstable fixed point in linear regime stabilizes when forcing is on.

The second fixed point (T_2^*, D_2^*, S_2^*) is located at $(x, y) = (0.53722, 0.63521)$ whose eigenvalues are $(0.0303+0.2043i, 0.0303-0.2043i)$. This fixed point is classified as a unstable focus.

Figure 5.5 showing the forced trajectory in phase plane. It also shows the time it takes for the trajectory into linear and nonlinear regimes when lights are on and off. It shows that the trajectory spends more time in nonlinear regime when forcing is off while it spends less time in a linear regime when forcing is on. Similar to the forced dynamics of the Rust Model, in the Byrne Model, we observed that, when the forcing turns on, the unstable fixed point (denoted by black open circle) becomes a stable fixed point (denoted by the red filled circle).

Periodic Forcing

In this section, we explore the entrainment properties (monoglot and polyglot entrainment responses) for the Byrne Model when applying the square-wave periodic effect on the fast rate. As the Byrne Model is two dimensional, we have an advantage of using phase plane analysis for different entrainment responses. For the Byrne Model, it turns out that we have both monoglot and polyglot entrainment responses. We term oscillations as subthreshold if the difference of peak and trough of the wave is smaller than 0.001.

Unstable Focus with sustained oscillations for an unforced system Similar to the Rust Model, in the Byrne Model, Monoglot entrainment responses are also observed when an unforced system has unstable focus with sustained oscillations. In the Rust Model, we did not find polyglot entrainment responses when we had damped oscillations for an unforced system. However, in the Byrne Model, we did find polyglot entrainment when we have stable focus (and hence damped oscillations) lies in the vicinity of second Hopf bifurcation. If a stable focus lies in the vicinity of the first Hopf bifurcation, we have do not have polyglot entrainment responses. The reason for getting polyglot in the vicinity of second Hopf, and not in first Hopf is because, second Hopf is located near the knee.

For an unforced system having unstable focus with sustained oscillations, the Arnold tongue observed has a similar structure (Figure 5.6 A1) as the one we observed for the Rust Model. In the Arnold tongue, the black markers denote the representative values of the forcing parameters A and T for which the time course dynamics have been shown in the remaining panels.

For an unforced system with stable focus, which lies in the vicinity of the first Hopf bifurcation also gives monoglot entrainment responses (Figure B.2). Interestingly, these time course dynamics have some similarities with entrainment

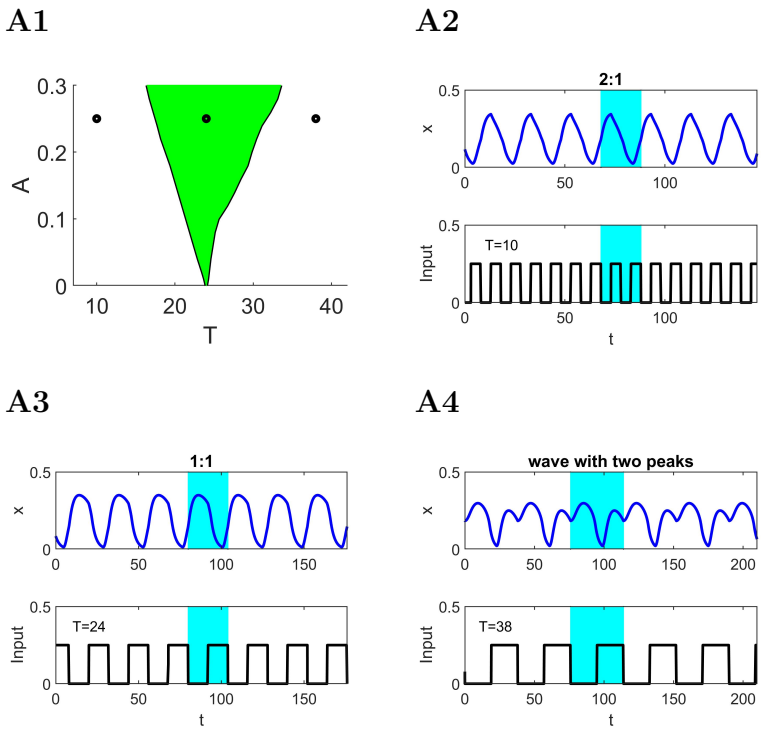

Figure 5.6 Representative entrainment patterns and Arnold tongue with monoglot structure for the Byrne Model in response to square-wave forcing. An unforced system has unstable fixed point with sustained oscillations of period 24 h ($E_0 = 0.203$). **A1.** Arnold tongue showing 1:1 entrainment regions (highlighted in green). **Remaining panels.** Time courses for the state variable x and the forcing signal for the values of T and A indicated in A1 (black markers).

responses for the Rust Model when an unforced system has a stable fixed point in the vicinity of first Hopf bifurcation (Figure 5.3). These similarities include low amplitude wave 1:1 oscillations for lower T, rapid increase in the amplitude of 1:1 oscillations for intermediate T, decrease in the amplitude of $1:1$ oscillations and then the emergence of a multi-peaked wave as T increases more.

Figure 5.7 shows the phase plane pictures for the representative responses in the monoglot structure (Figure 5.6). In each panel, when forcing is on, the trajectory is shown in red and when forcing is off, the trajectory is shown in black. Small open black and red dots denote the switching points (numbers labelled) when forcing is off and on, respectively. Large open black dot represents the unstable fixed point and a large filled red dot represents the stable fixed point. A magenta curve denotes the switching manifold, above which we have nonlinear regime and below we have linear regime. Dashed black and red curves denote the unforced and forced x-nullclines, respectively. Green curve denotes the y-nullcline which is unaffected by the forcing.

For $T = 10$, we have 2:1 responses for which the phase plane is shown in the Figure 5.7 A1. When the forcing turns off, denoted by switching point 1, the trajectory is in the fast regime (i.e., the trajectory moves faster away from right branch of the x-nullcline) and it approaches toward the right branch (dashed black) until the forcing turns on. When the forcing turns on, denoted by the switching point 2, we know that the forced system stabilizes the fixed point. Hence, the trajectory approaches toward the large red filled dot (the stable fixed point) and while approaching, the forcing turns off, denoted by the switching point 3. At this stage, the trajectory is again away from the right branch of the dashed black curve, hence it evolves on a faster time scale and moves away from an unstable fixed point. The forcing turns on at switching point 4, making the trajectory evolve towards the stable fixed point. While evolving towards the stable fixed point, forcing turns off

again and the cycle begins again. Hence, for two cycles of the forcing, we have one response.

For $T = 24$, we have 1:1 entrainment responses for which the phase plane is shown in the Figure 5.7 A2. For one cycle of the forcing comprising of two switching points denoted by 1 and 2, we have one response. Since T is longer, when forcing turn off, the trajectory moves further evolving under the dynamics of the unstable fixed point. When forcing turns off above the unforced x-nullcline at point 2, the trajectory moves faster, and enters the linear regime in which the trajectory evolves under the dynamics of a virtual fixed point located at the origin (not shown). As the forced trajectory enters the nonlinear regime, it approaches toward the stable fixed point and turns off before it gets there.

For $T = 38$, 1:1 entrainment breaks down as a wave with two peaks are observed. The forcing turns off right on the unforced x-nullcline, so that the trajectory evolves under the dynamics of an unstable fixed point and travels in the phase plane for longer as T is large. The forcing turns on in a linear regime, hence it approaches toward the virtual stable fixed point located at the origin (not shown). As it crosses the switching threshold, the trajectory evolves under the dynamics of a stable fixed point. Hence, it reaches the vicinity of a stable fixed point until the forcing turns off again. While the forcing is on, approaching towards closely the stable fixed point results in the first peak. The second peak occurs when forcing turns off and the trajectory has to go to the right branch of an unforced x-nullcline.

Stable Focus for an unforced system in the vicinity of Hopf bifurcation When the value of E_0 for an unforced system is chosen in the vicinity of the second Hopf bifurcation, we observed polyglot entrainment responses. For the range of E_0 values, for which we have polyglot entrainment, we have damped oscillations. For $E_0 = 0.25$, for which we have damped oscillations, polyglot structure is shown in the

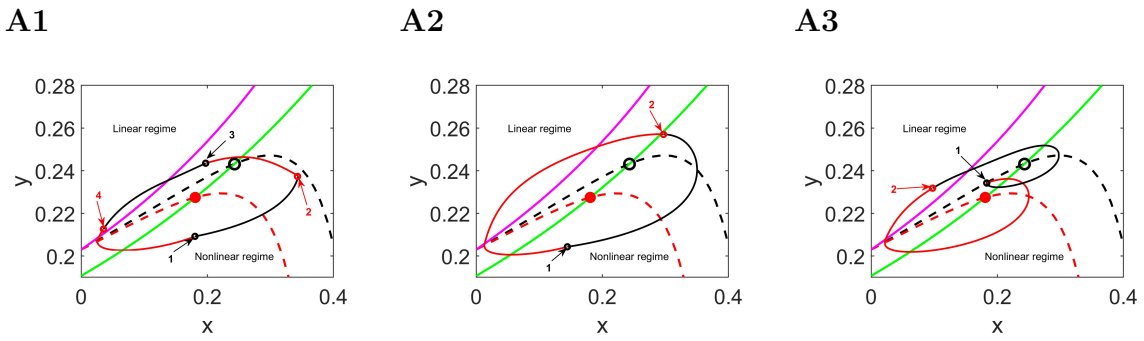

Figure 5.7 Phase-plane diagrams for the entrained and non-entrained responses shown in Figure 5.6 (square-wave input). The dashed curves are the x-nullclines for the unforced (black) and forced (red) systems, respectively. The green curve is the y-nullcline. The solid curves are the trajectories with the time intervals when the forcing is off and on shown in black and red, respectively. The numbers next to the arrows indicate the points in the phase-plane diagram at which the forcing turns off (small black open circles) and on (small red open circles). Black open large circle and red filled large circle denote unstable fixed point and stable fixed point for the unforced and forced system, respectively. **A1.** 2:1. **A2.** 1:1. **A3.** wave with two peaks.

Figure 5.8 A1. The polyglot structure observed here has a different structure. Unlike polyglot structure in FHN, different 1:1 tongues do not merge as we increase A. The first tongue in the shaded narrows as we increase A, while the second tongue in the shaded region widens as we increase A. The black markers are the representative amplitude and period values for which the time course dynamics are shown in the remaining panels.

Figure 5.9 shows the dynamical phase plane explanation of how we get polyglot entrainment. When forcing turns off or on, the corresponding systems has a stable fixed point. We look at four different representative values of T, for which we have different entrainment responses.

For $T = 19$, we see that for two inputs, we have one response, hence $2:1$ behaviour. The switching points when forcing turns off and on are located across the phase plane. When the forcing turns off, the switching point 1 is located in the linear regime and in the flow of fast movement of trajectory, hence the trajectory

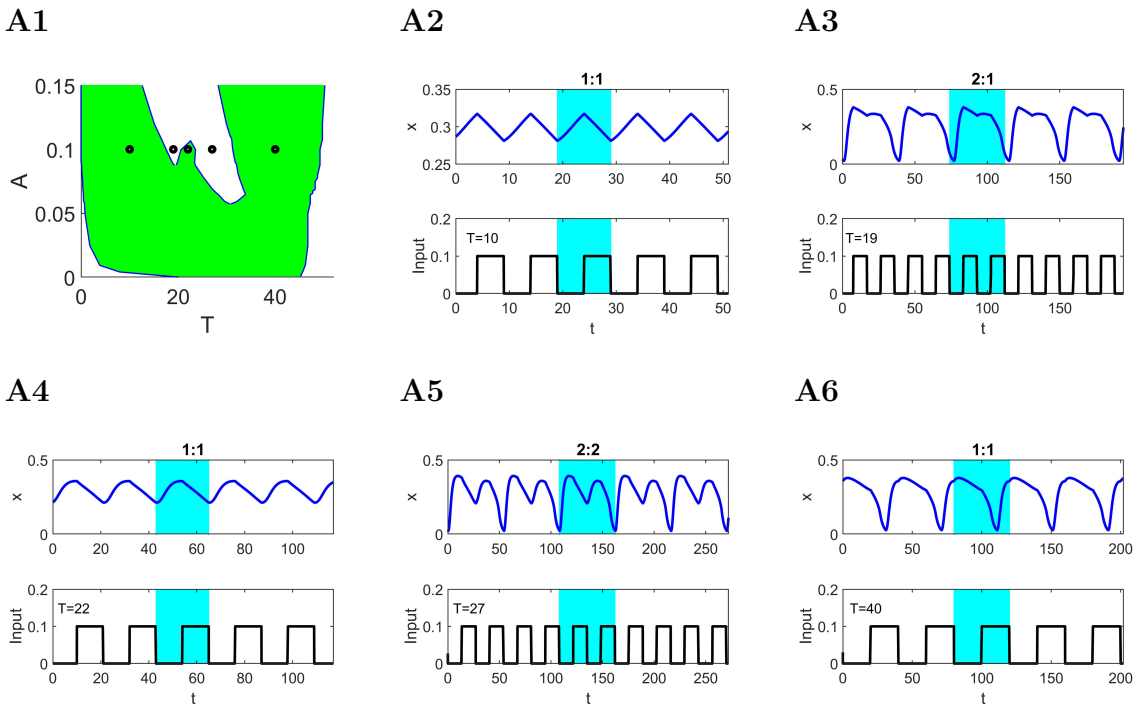

Figure 5.8 Representative entrainment patterns and Arnold tongue with polyglot structure for the Byrne Model in response to square-wave inputs. **A1.** Arnold tongue showing 1:1 entrainment regions (highlighted in green). **Remaining panels.** Time courses for the state variable x and the forcing for the values of T and A indicated in A1 (black markers). The fixed point for an unforced system is a stable focus ($E_0 = 0.25$).

approaches toward the virtual fixed point, it crosses the threshold and enters the nonlinear regime. When the forcing turns on labelled as 2, the trajectory approaches towards the right branch of forced $x-$ nullcline approaching towards the stable fixed (focus), it slows down as the dynamics along this branch are slow. The forcing turns off at switching point 3. At this point, the trajectory evolves considerably slower due to two facts: one is that is along the slow segment of $x-$ nullcline and the second is that is in the vicinity of stable fixed point (focus), so the trajectory evolves under the dynamics of stable focus. The forcing then turns on at 4. At this point, it is far from slow dynamics, hence it evolves on a fast time scale although the underlying system's fixed point is stable. Forcing turns off at 1, and hence, the trajectory is completed one round. Thus, we have $2:1$ responses.

For $T = 22$, we have $1:1$ responses though the amplitude of oscillations is suppressed. When the forcing turns off at 1, the trajectory is in the vicinity of an unstable region and it has to jump to the nearby attracting region, which is the right segment of the $x-$ nullcline, hence it jumps there. There, the forcing turns on, the trajectory evolution is slow as it is near to a stable fixed point although it is little away from the slower branch. Forcing turns off again at the same point 1. We count this low amplitude wave form as a 1:1 responses for these reasons: first, the trajectory spends more time in a non-linear regime (a feature of sustained oscillations), and second, the trajectory almost touched the right branch of the $x-$ nullcline.

For $T = 27$, we observe a multi-peaked wave (we call it $2:2$). We see that for one input, we have a large amplitude wave (forcing turns off at 1 and gives a large increase in amplitude) and for the second input, we have a small amplitude wave form (forcing turns off at 3).

Finally, for $T = 40$, we see $1:1$ responses. When forcing turns off, the trajectory slows down as it moves toward the stable slow branch and approaches toward the stable fixed point along this branch. When the forcing turns on, the fast dynamics

dominate the asymptotic approaching towards the stable fixed dynamics, hence the trajectory moves faster, enters the linear regime, then enters the nonlinear regime and forcing then turns off again at the same point 1.

Stable Node for an unforced system Similar to the Rust Model, the Byrne Model also shows robust entrainment properties when an unforced system has a stable node fixed point as shown in the Figure 5.10. We take $E_0 = 0.35$, for which we have stable node. The fixed point lies to the right of the second Hopf bifurcation.

Bifurcation diagram and the region of monoglot and polyglot entrainment Figure 5.11 is the bifurcation diagram as a function of parameter E_0 showing the region of E_0 values for the unforced system for which we have monoglot entrainment and polyglot entrainment (shaded). Red lines denote the representative E_0 values taken in Figure 5.6 (monoglot) and Figure 5.8 (polyglot). Polyglot entrainment occurs only for damped oscillations in the vicinity of second Hopf bifurcation. For the damped oscillations in the vicinity of first Hop bifurcation, we observed monoglot (not shown).

5

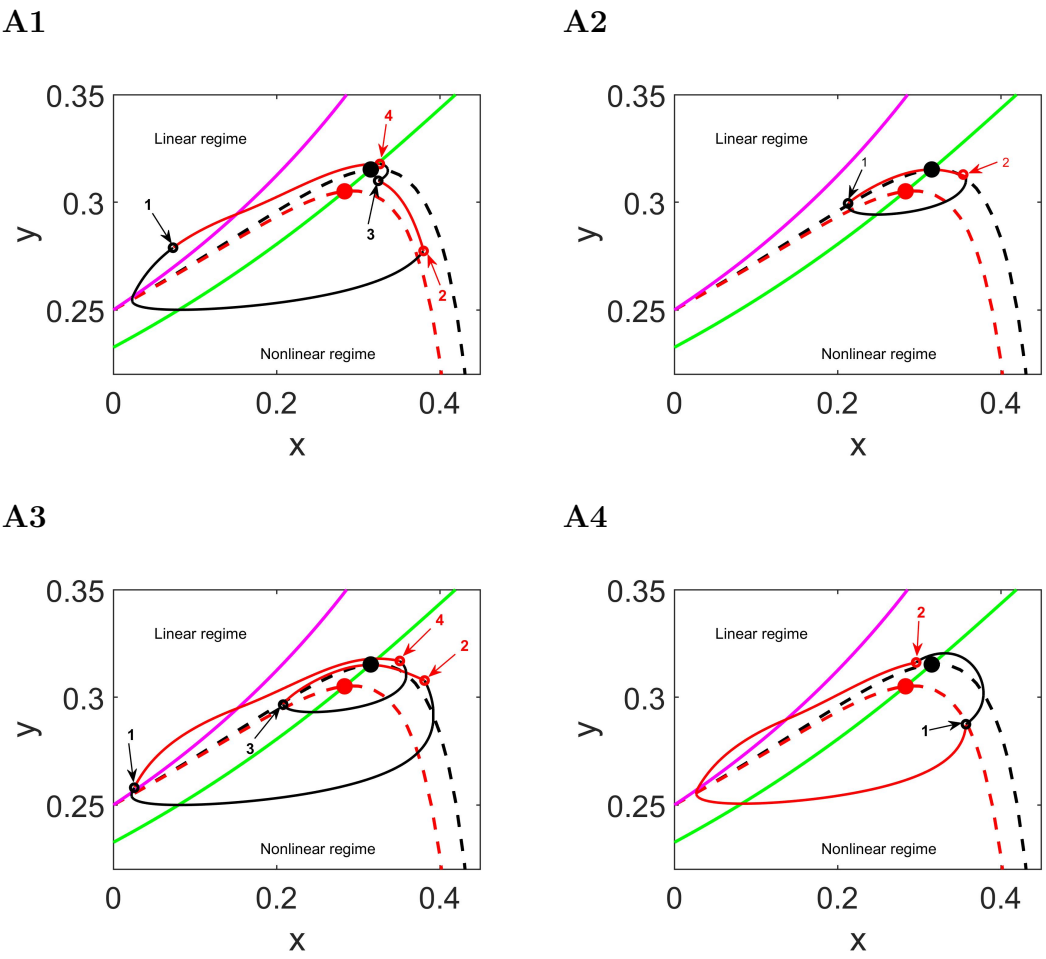

Figure 5.9 Phase-plane diagrams for the entrained responses shown in Figure 5.8 (square-wave input). The dashed curves are the x-nullclines for the unforced (black) and forced (red) systems, respectively. The green curve is the y-nullcline. The solid curves are the trajectories with the time intervals when the forcing is off and on shown in black and red, respectively. The numbers next to the arrows indicate the points in the phase-plane diagram at which the forcing turns off (small black open circles) and on (small red open circles). Black and red large circles denote stable fixed points for the unforced and forced system, respectively. **A1.** 2:1. **A2.** 1:1. **A3.** 2:2. **A2.** 1:1.

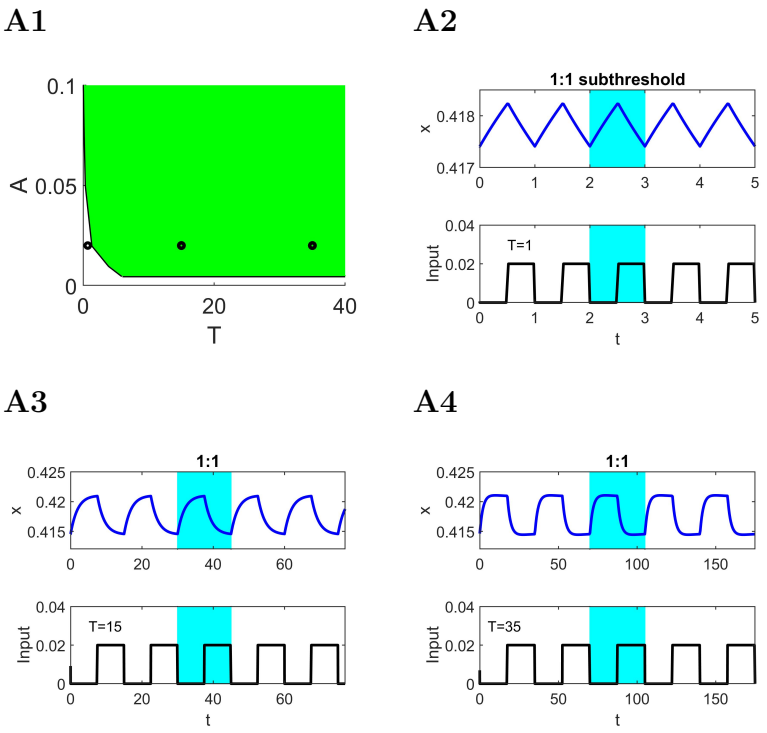

Figure 5.10 Representative entrainment patterns and Arnold tongue with monoglot structure for the Byrne Model in response to square-wave forcing when an unforced system has stable node ($E_0 = 0.35$). **A1.** Arnold tongue showing 1:1 entrainment regions (highlighted in green). **Remaining panels.** Time courses for the state variable S and the forcing signal for the values of T and A indicated in A1 (black markers).

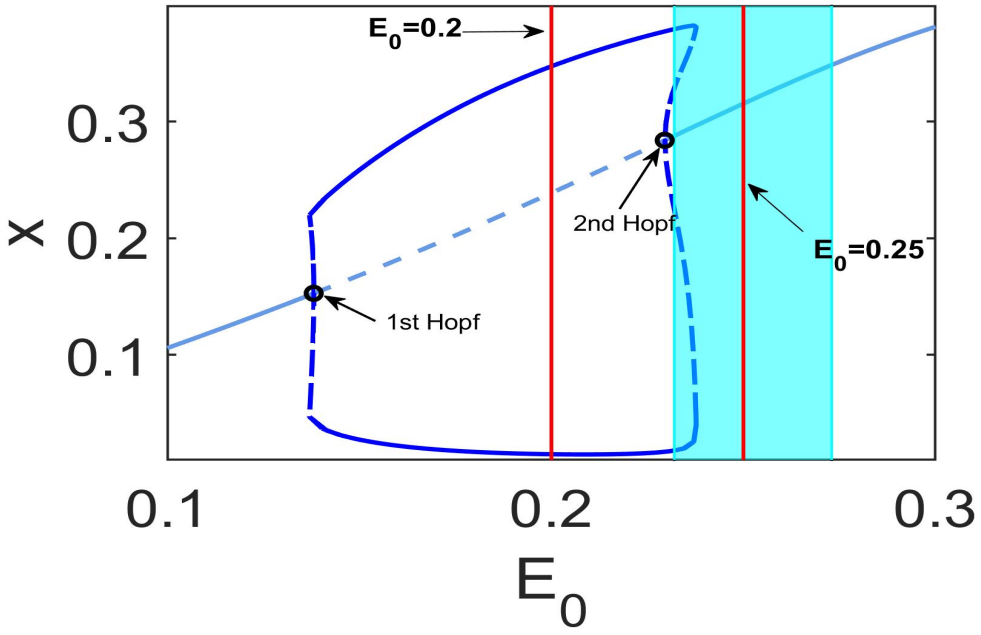

Figure 5.11 Bifurcation diagram as a function of the parameter E_0. The shaded region denote the E_0 values for the unforced system for which we have 1:1 polyglot entrainment. The red lines denote the representative E_0 values used in the previous figures for the unforced system. $E_0 = 0.203$ (monoglot entrainment in Figure 5.6-A1), and $E_0 = 0.25$ (polyglot entrainment in Figure 5.8).

CHAPTER 6

HOPF BIFURCATION - A NECESSARY BUT NOT SUFFICIENT CONDITION FOR POLYGLOT ENTRAINMENT

6.1 Polyglot Entrainment Requires a Hopf Bifurcation

In Chapter 3, the FHN model was explored for polyglot entrainment responses. We found that polyglot entrainment occurs in the vicinity of a Hopf bifurcation. In Chapter 5, we analyzed polyglot entrainment responses for the Byrne model and we again found that polyglot entrainment occurs near a Hopf bifurcation. In this Chapter, we explore other models for polyglot entrainment responses. As discussed below, from the results of these models we conclude that for polyglot entrainment, Hopf bifurcation is a necessary but not sufficient condition.

Polyglot entrainment in Morris-Lecar model

The Morris-Lecar neuronal model is a model of oscillations in the barnacle giant muscle fiber [67]. We investigated polyglot entrainment responses in both Type I (SNIC) and Type II (Hopf) bifurcation structures (Figure 6.2). For Type I, a SNIC bifurcation occurs at a lower I_{app} value and a Hopf bifurcation occurs at a higher I_{app} value, near the upper knee of the $v-$ nullcline. In the vicinity of the Hopf bifurcation, we found polyglot entrainment responses. We did not observe polyglot entrainment near the SNIC bifurcation. For Type II, we have two Hopf bifurcations which occur near the lower knee and upper knee. In the vicinity of both Hopf bifurcations, we found polyglot entrainment (Figure 6.1 A).

Polyglot entrainment in the Oregonator 2D model

The Oregonator is a model of chemical oscillations in the Belousov-Zhabotinsky (BZ) reaction [27, 101]. In the 2D Oregonator model, a Hopf bifurcation occurs and is

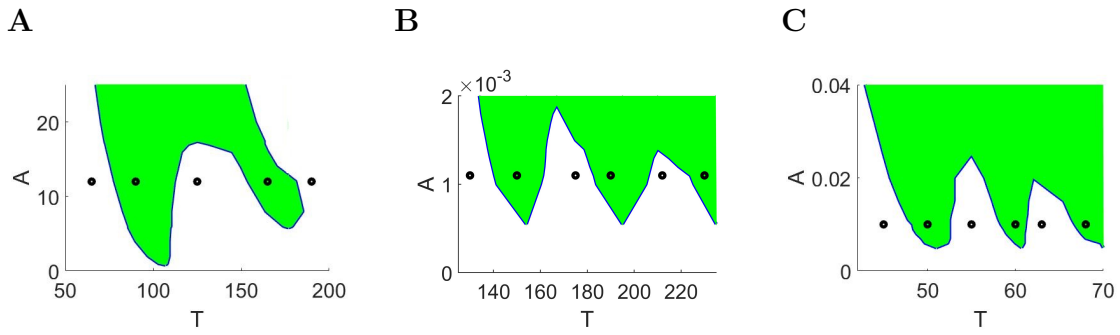

Figure 6.1 Polyglot entrainment in other models in response to square-wave periodic forcing. **A** Morris-Lecar model. We used the following parameters for the unforced system. $C = 20$, $E_l = -60$, $E_{Ca} = 120$, $Ek = -84$, $G_l = 2$, $G_k = 8$, $G_{Ca} = 4$, $\phi = 0.04$, $V_1 = -1.2$, $V_2 = 18$, $V_3 = 2$, $V_4 = 30$, $I_{app} = 95$. For the unforced system, we have stable focus. **B** Oregonator 2D model. We used the following parameters for the unforced system. $\eta = 2.28$ (fixed point is a stable focus), $q = 0.01$ and $\epsilon = 0.025$. **C** Novak-Tyson model. We used the following parameters for the unforced system. $v_m = 1$, $k_m = 0.1$,$v_p = 0.5$, $k_{p_1} = 10$, $k_{p_2} = 0.03$, $k_{p_3} = 0.1$, $K_{eq} = 3.3$, $P_{crit} = 0.1$, $J_p = 0.05$.

located in the vicinity of a cubic nullcline. We found polyglot entrainment in the 2D Oregonator (Figure 6.1 B and Figure 6.4).

Polyglot entrainment in the Novak–Tyson model

The Novak–Tyson model [72, 91], which is a model of circadian oscillations in *Drosophila*, was investigated for polyglot entrainment responses. The Novak–Tyson model has a Hopf bifurcation, and in the vicinity of the Hopf point, we found polyglot entrainment responses (Figure 6.1 C).

6.2 Hopf Bifurcation is not Sufficient for Polyglot Entrainment

So far we have observed that polyglot entrainment requires a Hopf bifurcation. A question arises here: *Do we always obtain polyglot entrainment responses in the vicinity of a Hopf bifurcation?* The answer is no!

We have found a counter example in which we have a Hopf bifurcation, but we do not have polyglot entrainment responses. The Lengyel-Epstein (LE) system [59,60]

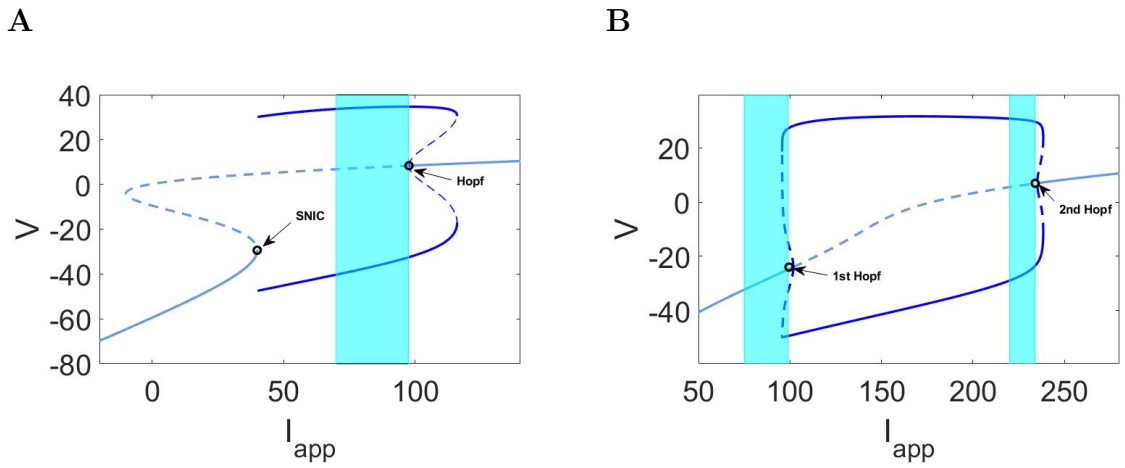

Figure 6.2 Different bifurcation structures in Morris-Lecar model showing polyglot entrainment in the vicinity of Hopf bifurcation. **A.** Type-I bifurcation in which we have SNIC for lower I_{app} and a Hopf bifurcation for higher I_{app}. **B.** Type-II bifurcation in which we two Hopf bifurcations, one for lower I_{app} and one for higher I_{app}. We used the following parameters $C = 20$, $E_l = -60$, $E_{Ca} = 120$, $Ek = -84$, $G_l = 2$, $G_k = 8$, $G_{Ca} = 4$, $V_1 = -1.2$, $V_2 = 18$. For Type-I, we used $\phi = 0.067$, $V_3 = 12$, $V_4 = 17.4$. For Type-II, we used $\phi = 0.04$, $V_3 = 2$, $V_4 = 30$.

is a model for chemical oscillations which has a Hopf bifurcation but we do not have polyglot entrainment (Figure 6.6 A4) in the vicinity of the Hopf. The Hopf bifurcation in the LE system is located far from the knee of the cubic-like nullcline (Figure 6.6 A1 & A2). Thus, in the vicinity of the Hopf bifurcation, the nullcline is not parabolic-like.

If we have a parabolic structure for a nullcline in the vicinity of a Hopf bifurcation, then we have polyglot entrainment. The presence of Hopf bifurcation alone does not ensure polyglot entrainment. A Hopf bifurcation with certain local structure (i.e. a parabolic-like nullcline) is needed for polyglot entrainment.

6.3 Do we have Polyglot Entrainment in 3D Models?

For 2D models, we have polyglot entrainment responses if a model has a nullcline with a knee and a Hopf bifurcation occurs near the knee. We also investigated some 3D models to see if they have polyglot entrainment responses or not. We checked for polyglot entrainment responses in four different 3D models: the Goodwin model

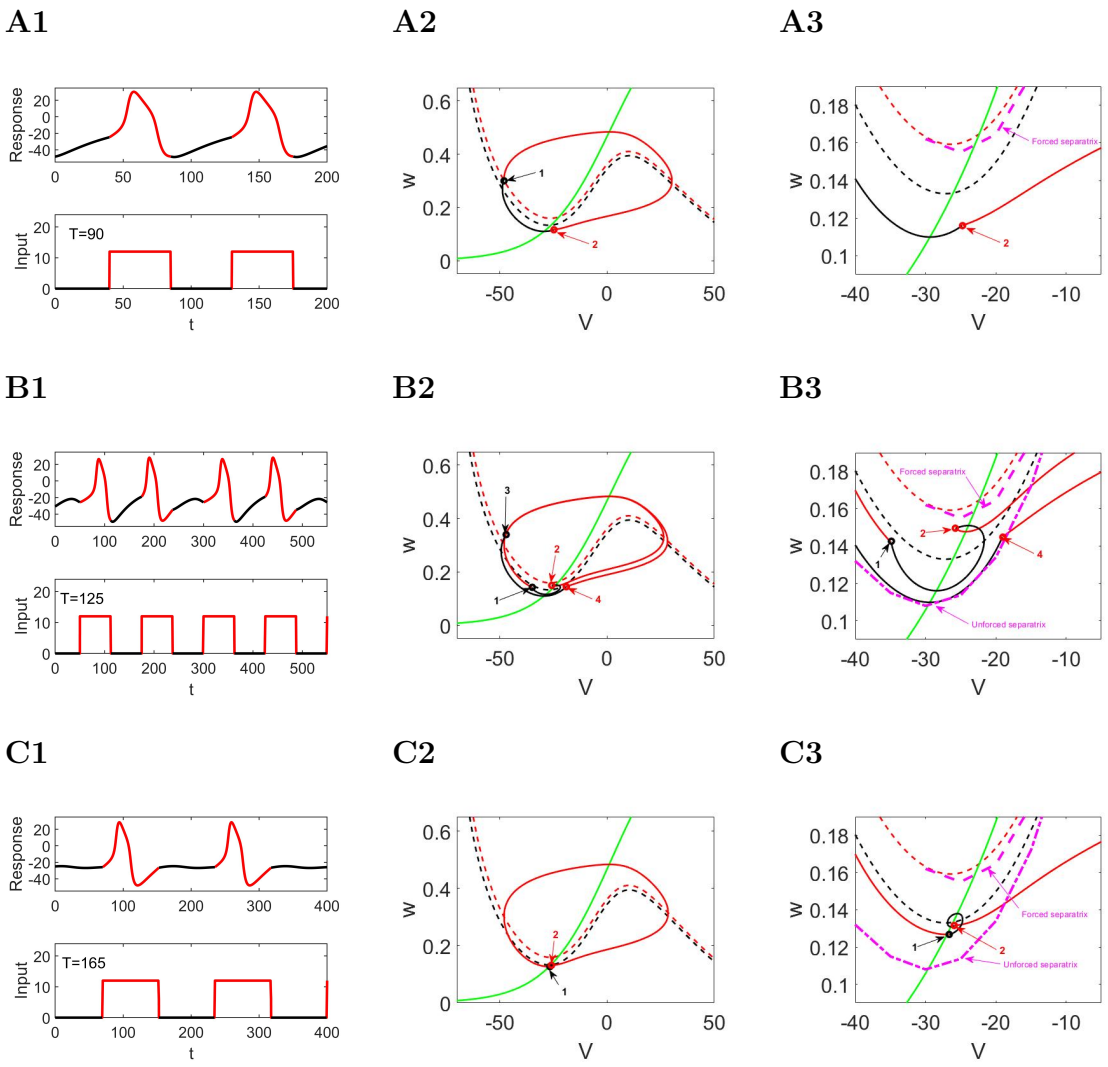

Figure 6.3 Representative examples of 1:1 polyglot entrainment dynamics and their break-down in Fig 6.1 **A**. **Left column.** Time courses for v and the forcing. **Middle column.** Phase-plane diagrams. **Right column.** Phase-plane diagram magnification in vicinities of the knee of the $v-$nullcline. **A.** 1:1 entrainment for $T = 90$. **B.** 2:2 entrainment for $T = 125$. **C.** 1:1 entrainment for $T = 165$. We used the following parameters for the unforced system. $C = 20$, $E_l = -60$, $E_{Ca} = 120$, $Ek = -84$, $G_l = 2$, $G_k = 8$, $G_{Ca} = 4$, $\phi = 0.04$, $V_1 = -1.2$, $V_2 = 18$, $V_3 = 2$, $V_4 = 30$.

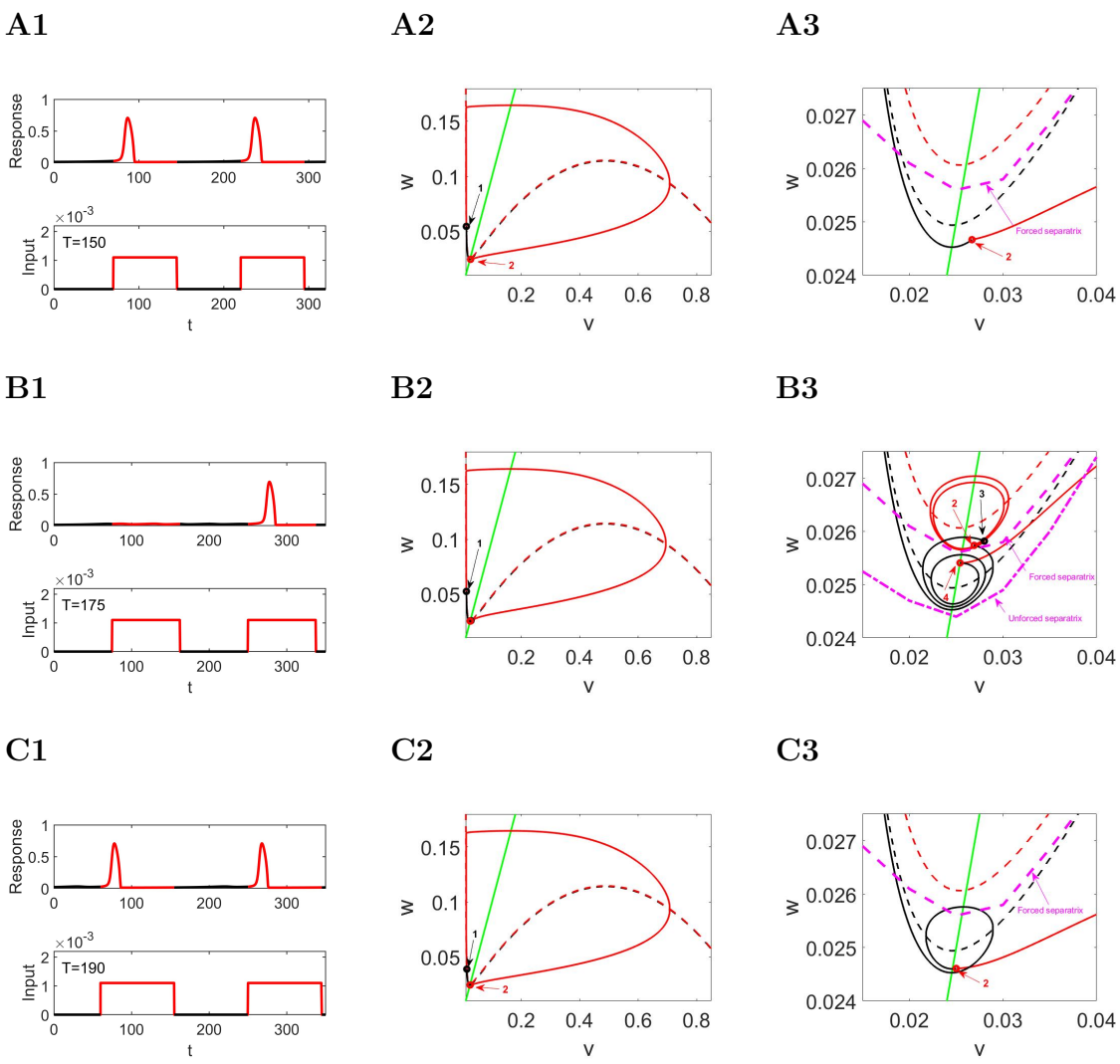

Figure 6.4 Representative examples of 1:1 polyglot entrainment dynamics and their break-down in Fig 6.1 **B**. **Left column.** Time courses for v and the forcing. **Middle column.** Phase-plane diagrams. **Right column.** Phase-plane diagram magnification in vicinities of the knee of the cubic nullcline. **A.** 1:1 entrainment for $T = 150$. **B.** 2:1 entrainment for $T = 175$. **C.** 1:1 entrainment for $T = 190$. We used the following parameter values: $\eta = 2.28$, $q = 0.1$ and $\epsilon = 0.025$.

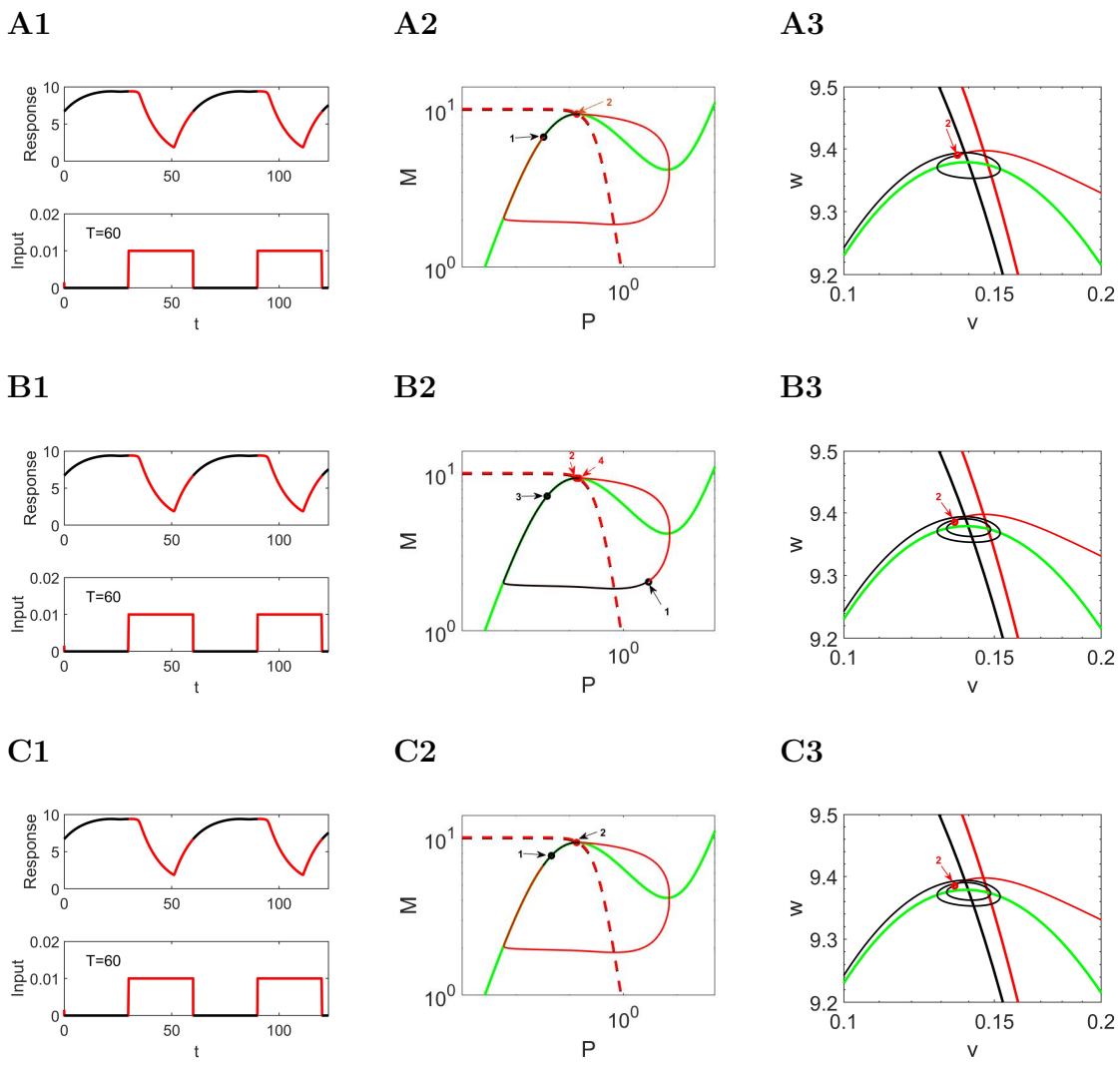

Figure 6.5 Representative examples of 1:1 polyglot entrainment dynamics and their break-down in Fig 6.1 **C**. **Left column.** Time courses for M and the forcing. **Middle column.** Phase-plane diagrams. **Right column.** Phase-plane diagram magnification in vicinities of the knee of the P-nullcline. **A.** 1:1 entrainment for $T = 60$. **B.** 2:2 entrainment for $T = 63$. **C.** 1:1 entrainment for $T = 68$. We used the following parameter values: $v_m = 1$, $k_m = 0.1$,$v_p = 0.5$, $k_{p_1} = 10$, $k_{p_2} = 0.03$, $k_{p_3} = 0.1$, $K_{eq} = 3.3$, $P_{crit} = 0.1$, $J_p = 0.05$.

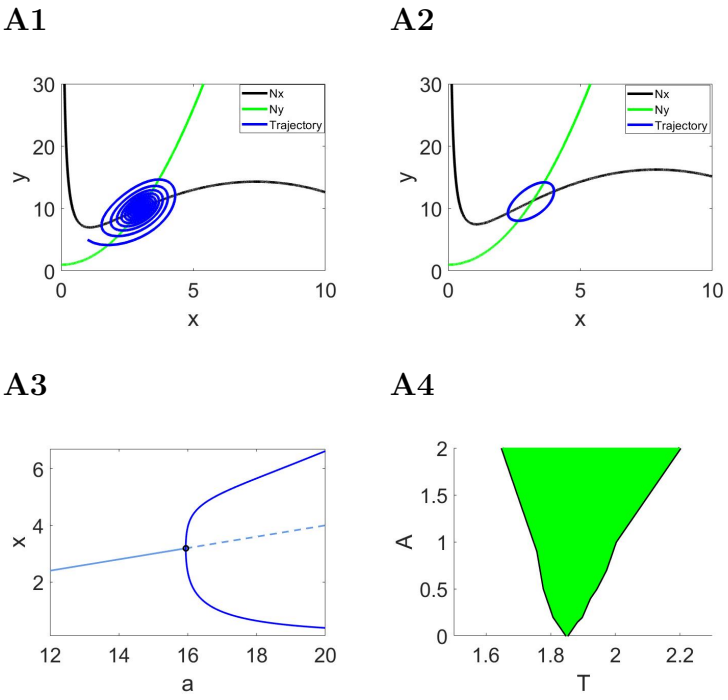

Figure 6.6 Phase plane, bifurcation and entrainment responses for Lengyel-Epstein model. **A1.** Trajectory in phase plane before bifurcation ($a = 15$). **A2.** Trajectory in phase plane after bifurcation ($a = 16$). **A3.** Bifurcation diagram for parameter a. **A4.** Monoglot structure in the vicinity of Hopf.

[33, 35], the Kim protein sequestration (PS) [50] model, the Jolley model [45] and the Oregonator model [27, 101]. In these 3D models we did not observe polyglot entrainment responses even in the vicinity of Hopf bifurcation. We have not yet attempted to compute null surfaces or analyze the phase space of these models as doing so is more involved than computing nullclines and performing phase plane analysis for 2D models. Also, there are many other 3D models of biological oscillators that could be considered. If polyglot entrainment is found in a 3D model, it would be interesting to see what dynamical structures are present analogous to the knee of cubic nullclines in 2D models.

CHAPTER 7

DISCUSSION

Entrainment is a hallmark phenomenon in oscillatory systems or a network of oscillatory systems. Understanding entrainment gives insight into the system [78]. We investigated entrainment properties when an unforced system has self-sustained oscillations, damped oscillations or non-oscillatory solutions. To explore entrainment properties, we studied neuronal and circadian models. For neuronal models, we focused on the FitzHugh-Nagumo model and in Chapter 2 explored different qualitative properties of the unforced model by varying parameters. Having identified a sustained oscillatory regime, a damped oscillatory regime and a non-oscillatory regime, we set the stage for Chapter 3 in which we explored entrainment properties under the periodic forcing.

In Chapter 3, we found that in the vicinity of a Hopf bifurcation (where the unforced system has either a stable focus and exhibits damped oscillations or an unstable focus and exhibits sustained oscillations) the entrainment region has a nonstandard structure when depicted by an Arnold tongue diagram. Polyglot entrainment (disconnected multiple 1:1 tongues) is observed when periodic forcing is applied to a system with a weakly stable or weakly unstable focus. Further away from the vicinity of the Hopf bifurcation, applying periodic forcing to a system with a strongly unstable focus and sustained oscillations gives monoglot entrainment responses like a standard Arnold tongue. Further away from the Hopf bifurcation in the other direction, applying periodic forcing to a non-oscillatory system with a stable node gives monoglot entrainment responses that are quite robust (i.e. they do not break for higher period values of the forcing).

In Chapter 4, we studied circadian clock models based on post-translational modifications. In these models, phosphorylation and dephosphorylation of proteins occur on a circadian time scale. The Rust model and Byrne model are studied. The former is a three dimensional model for circadian oscillations in cyanobacteria, while the latter is a two dimensional model of post-translational oscillations (PTOs). These two PTO based models have non-smooth dynamics [17, 58, 62]. In these models, we used dynamical systems tools to analyze how limit cycle oscillations are formed. We found that in these two models, which are of different dimension and have different formulations and dynamics, nonetheless share a similar mechanism of oscillations since in both systems they are generated by the system's trajectory crossing a switching manifold.

In Chapter 5, we investigated the entrainment properties of the Rust model and Byrne model. For the Rust model, we only observed monoglot entrainment responses both in the vicinity and far away from the Hopf bifurcation. For the Byrne model, we observed both monoglot and polyglot entrainment responses. Polyglot entrainment responses were observed in the vicinity of one Hopf bifurcation, but not in the vicinity of the other Hopf bifurcation. Observing polyglot entrainment responses in the vicinity of one Hopf but not the other motivated us to explore more models.

In Chapter 6, we tested entrainment responses for other models of neuronal, circadian and glycolytic oscillations. From the models tested in this chapter, we found two results which also hold for entrainment studies in previous chapters. First, polyglot entrainment requires a Hopf bifurcation. If we do not have a Hopf bifurcation, we do not observe polyglot entrainment. Second, simply having a Hopf bifurcation does not guarantee there will be polyglot entrainment. For having polyglot entrainment, in the vicinity of the Hopf bifurcation there needs to be a parabolic-like

nullcline structure. Our entrainment analysis is not exhaustive or universal, and as we tested only a few models in this study our conclusions are still tentative.

7.1 Implications of Polyglot Entrainment

Polyglot entrainment has been investigated in neuronal and circadian models. What could be the impact of polyglot entrainment on circadian and neuronal systems?

In the neuroscience context, having a polyglot entrainment phenomenon could be related to entrainment of different neurons (or populations of neurons) in different parts of the brain to different signals. For example, these signals could be brain waves [5, 94] which maintain a variety of states of consciousness ranging from deep sleep to active thinking and reactions. These brains waves have different frequencies: alpha waves ($8-13$ Hz), beta waves ($13-32$ Hz), or gamma waves ($32-100$ Hz). If a neuron or a network of neurons has the polyglot entrainment property, then perhaps they can be entrained 1:1 to multiple different brain waves with different frequencies.

In the context of the circadian clock, the period of external forcing is fixed at 24 hours (due to the Earth's rotation) but intrinsic periods of the circadian clock vary across individuals in a population. If the intrinsic period is closer to 24 hours, which is the period of forcing, then one may expect 1:1 entrainment. As the intrinsic period gets further away from 24 hours, we expect to lose 1:1 entrainment. However, if we have polyglot entrainment responses for a population of circadian clocks, then as the intrinsic period gets even further from 24 then 1:1 entrainment may be regained.

7.2 Future Work

Within complex organisms as well as simple ones, cellular oscillators interact with each other to form systems of coupled oscillators [39]. For example, coupled circadian oscillations exist in multicellular cyanobacteria [2]. In mammals, central circadian oscillators located in the hypothalamic suprachiasmatic nucleus receive

direct information about light-dark cycles via photic input pathways. These central oscillators in turn interact with circadian oscillators in peripheral tissues located throughout the body. Such systems are described as hierarchical coupled oscillators and are studied in terms of how such systems are entrained to light-dark cycles [61]. It would be interesting to see if we have polyglot entrainment in hierarchical coupled systems.

Working along similar lines, one can also investigate polyglot entrainment responses in a network consisting of different types of oscillators such as self-sustained oscillators, damped oscillators, and non-oscillators. For example, do we get polyglot entrainment in two coupled oscillators when one is a damped oscillator and the second is a self-sustained oscillator, or when one is a self-sustained oscillator and the second is non-oscillatory?

APPENDIX A

MONOGLOT AND POLYGLOT ENTRAINMENT RESPONSES FOR OTHER PARAMETER REGIMES IN FHN MODEL

In Chapter 3, we showed monolgot and polyglot entrainment responses for the FHN Model under square-wave periodic forcing, fix value of α and fix value of ϵ. Here, we show entrainment results for other possibilities like sinusoidal forcing, increasing ϵ, and increasing α.

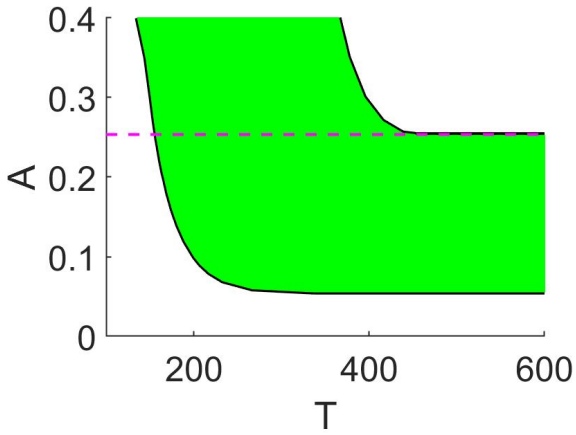

Figure A.1 Arnold tongue with monoglot structure in response to square-wave forcing. We used the following parameters for the unforced system: $\lambda = -0.25$ (fixed point is a stable node), $\alpha = 2$ and $\epsilon = 0.01$.

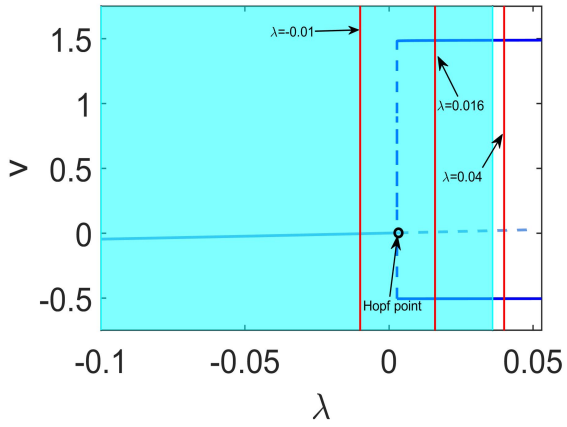

Figure A.2 Bifurcation diagram as a function of the parameter λ for $\alpha = 2$ and entrainment region for sinusoidal forcing. The shaded region denote the λ values for the unforced system for which we have 1:1 polyglot entrainment. The red lines denote the representative λ values used in the previous figures for the unforced system and sinusoidal forcing. $\lambda = 0.04$ (Figure A.12 A), $\lambda = 0.016$ (Figure A.13), and $\lambda = -0.01$ (Figure A.14).

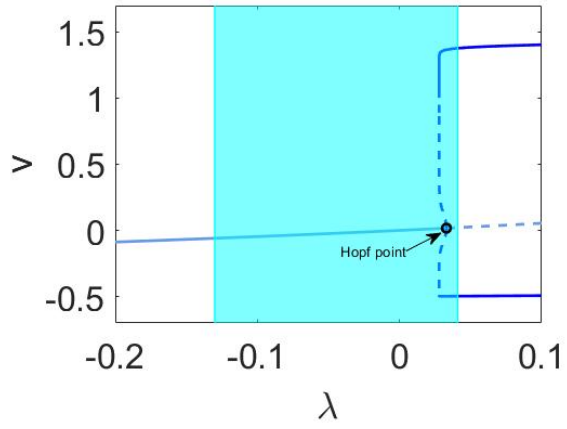

Figure A.3 Bifurcation diagram as a function of the parameter λ for $\alpha = 2$ and $\epsilon = 0.1$ showing the entrainment regions for square-wave forcing. We have subcritical Hopf bifurcation at $\lambda = 0.033$. The shaded region denote the λ values for the unforced system for which we have 1:1 polyglot entrainment.

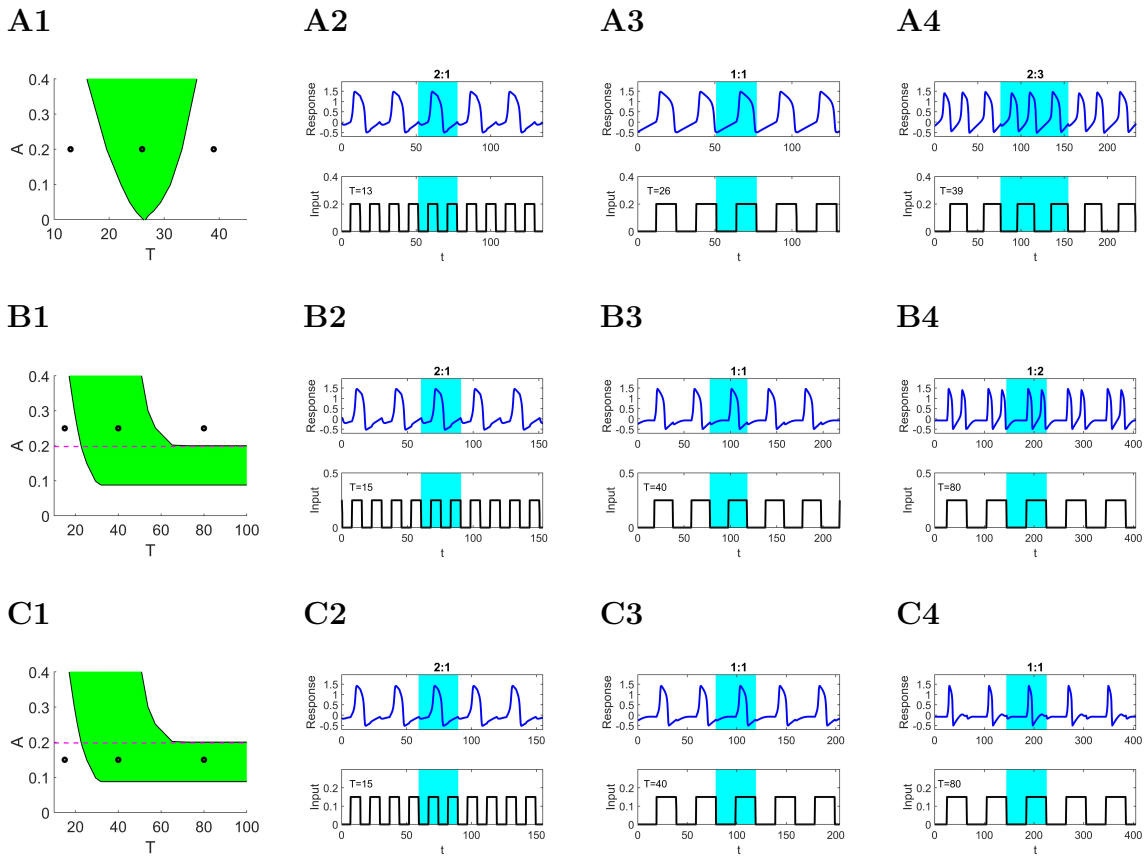

Figure A.4 Representative entrainment patterns and Arnold tongues with monoglot structure in response to square-wave forcing. **A1, B1, & C1.** Arnold tongues showing 1:1 entrainment regions (highlighted in green). The dashed-magenta (horizontal) lines in panels B1 and C1 indicate the value of A for which the system with constant forcing A changes from a stable (below) to an unstable (above) focus. **Remaining panels.** Time courses for v and the forcing signal for the values of T and A indicated in A1, B1, and C1 (black markers). **A.** $\lambda = 0.08$ (Fig. 3.1-A1) and $A = 0.2$. **B.** $\lambda = -0.17$ (Fig. 3.1-B1) and $A = 0.25$. **C.** $\lambda = -0.17$ (Fig. 3.1-C1) and $A = 0.15$. We used the following parameter values: $\alpha = 2$, $\epsilon = 0.1$.

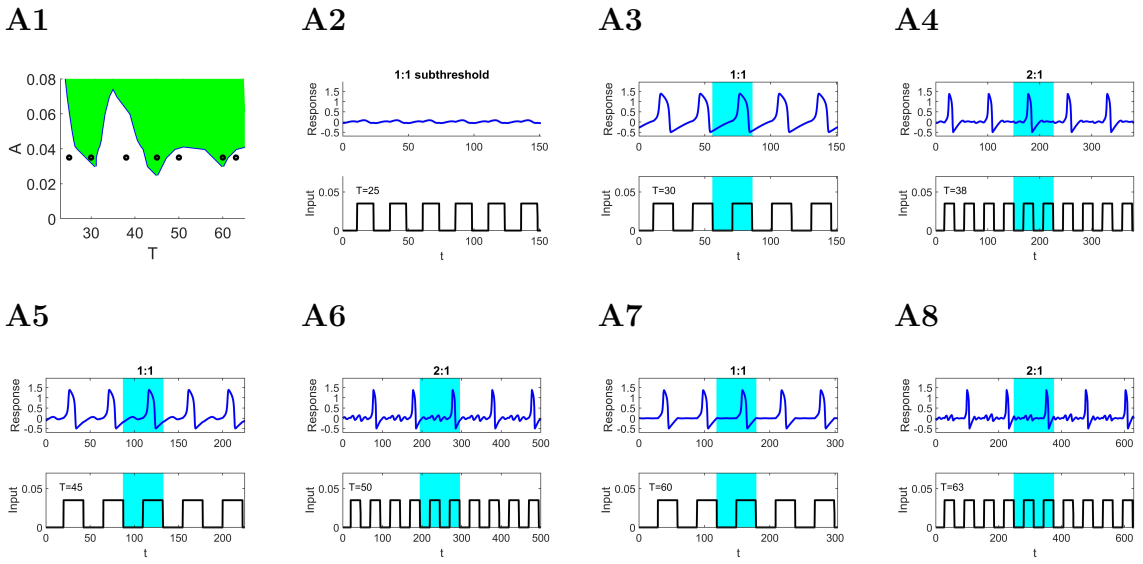

Figure A.5 Representative entrainment patterns and Arnold tongues with polyglot structure in response to square-wave inputs. **A1.** Arnold tongues showing 1:1 entrainment regions (highlighted in green). **Remaining panels.** Time courses for v and the forcing for the values of T and A indicated in A1 (black markers). We used the following parameter values: $\alpha = 2$, $\lambda = 0$ and $\epsilon = 0.1$.

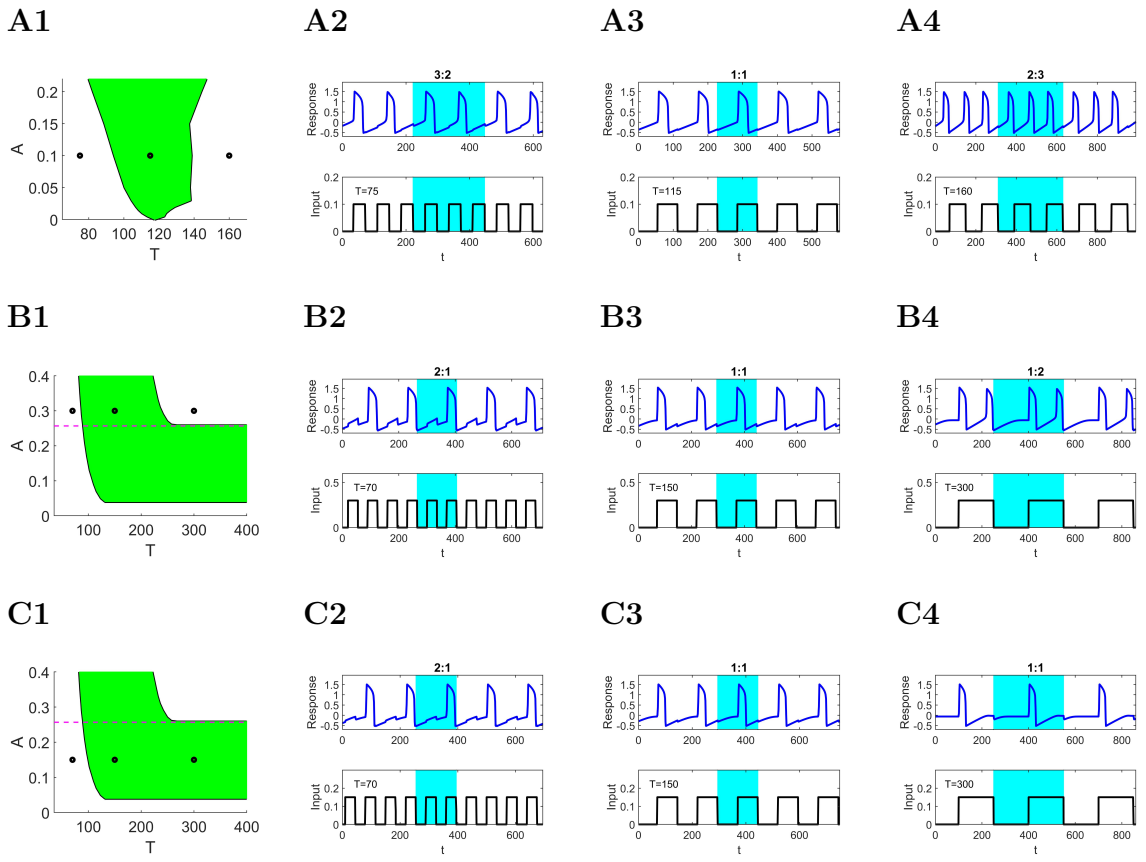

Figure A.6 Representative entrainment patterns and Arnold tongues with monoglot structure in response to square-wave forcing. **A1, B1, & C1.** Arnold tongues showing 1:1 entrainment regions (highlighted in green). The dashed-magenta (horizontal) lines in panels B1 and C1 indicate the value of A for which the system with constant forcing A changes from a stable (below) to an unstable (above) focus. **Remaining panels.** Time courses for variable v and the forcing signal for the values of T and A indicated in A1, B1, and C1 (black markers). **A.** $\lambda = 0.026$ and $A = 0.1$. **B.** $\lambda = -0.25$ and $A = 0.3$. **C.** $\lambda = -0.25$ and $A = 0.15$. We used the following parameter values: $\alpha = 4$, $\epsilon = 0.01$.

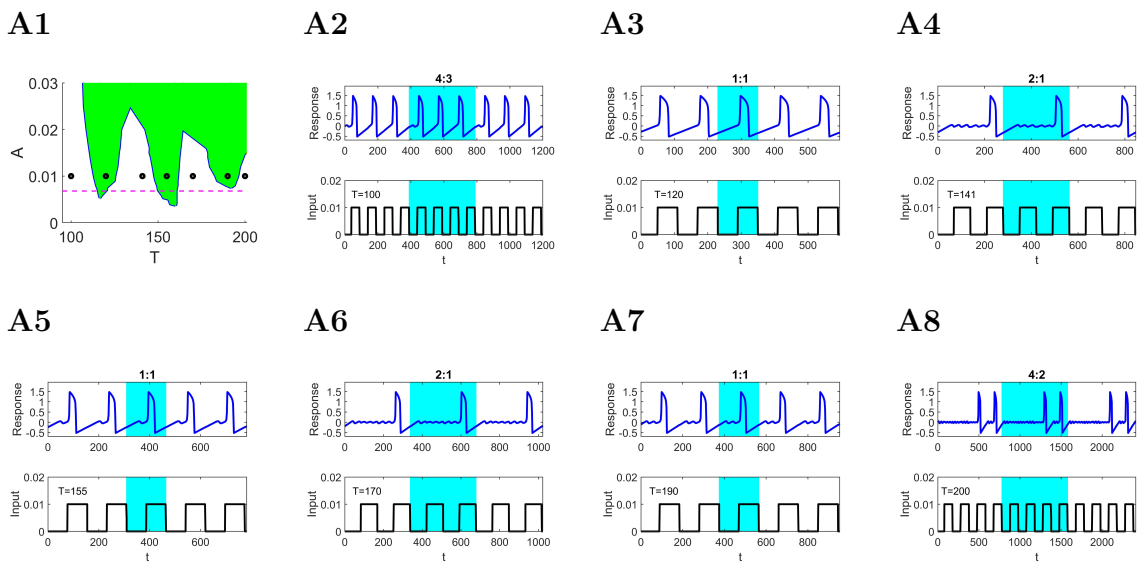

Figure A.7 Representative entrainment patterns and Arnold tongue with polyglot structure in response to square-wave inputs. **A1.** Arnold tongue showing 1:1 entrainment regions (highlighted in green). **Remaining panels.** Time courses for v and the forcing for the values of T and A indicated in A1 (black markers). The dashed-magenta (horizontal) lines in panel A1 indicate the value of A for which the system with constant forcing A changes from a stable (below) to an unstable (above) focus. We used the following parameter values: $\alpha = 4$, $A = 0.01$, $\lambda = 0$ and $\epsilon = 0.01$. The fixed point for the unforced system is a stable focus.

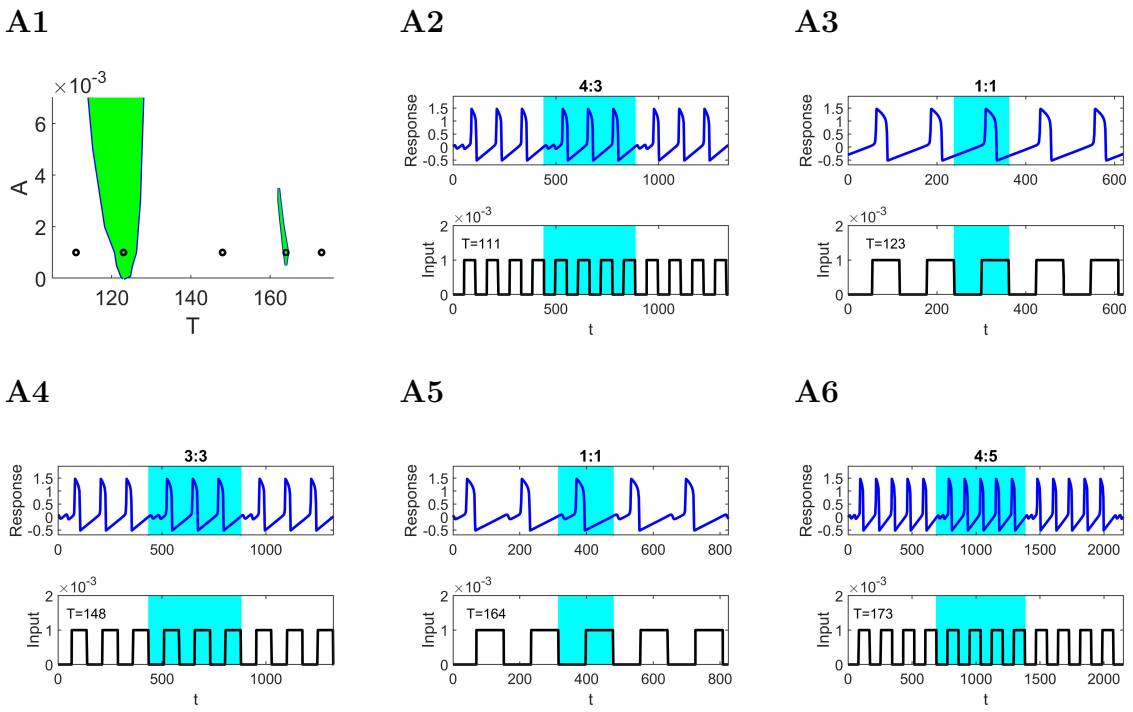

Figure A.8 Representative entrainment patterns and Arnold tongue with polyglot structure in response to square-wave inputs. **A1.** Arnold tongue showing 1:1 entrainment regions (highlighted in green). **Remaining panels.** Time courses for v and the forcing for the values of T and A indicated in A1 (black markers). We used the following parameter values: $\alpha = 4$, $A = 0.001$, $\lambda = 0.01$ and $\epsilon = 0.01$. The fixed point for the unforced system is an unstable focus.

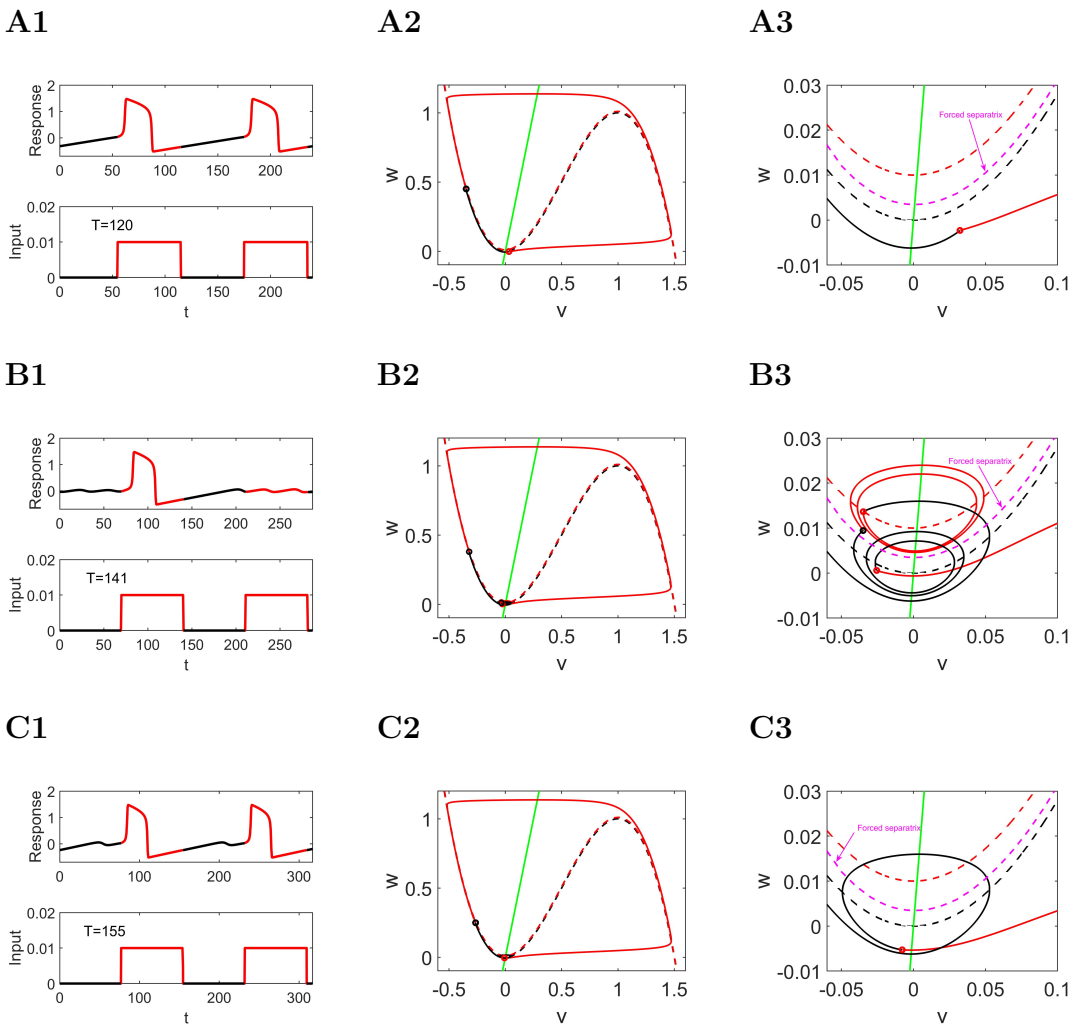

Figure A.9 Representative examples of 1:1 polyglot entrainment dynamics and their break-down. **Left column.** Time courses for v and the forcing. **Middle column.** Phase-plane diagrams. **Right column.** Phase-plane diagram magnification in vicinities of the knee of the v-nullclines. The black (red) portions of the v time courses and trajectories correspond to the forcing turned off (on). **A.** 1:1 entrainment for $T = 120$ (Fig. A.7-A3). **B.** 2:1 entrainment for $T = 141$ (Fig. A.7-A4). **C.** 1:1 entrainment for $T = 155$ (Fig. A.7-A5). We used the following parameter values $\alpha = 4$, $\lambda = 0$, $A = 0.01$ and $\epsilon = 0.01$ (Figure A.7-A).

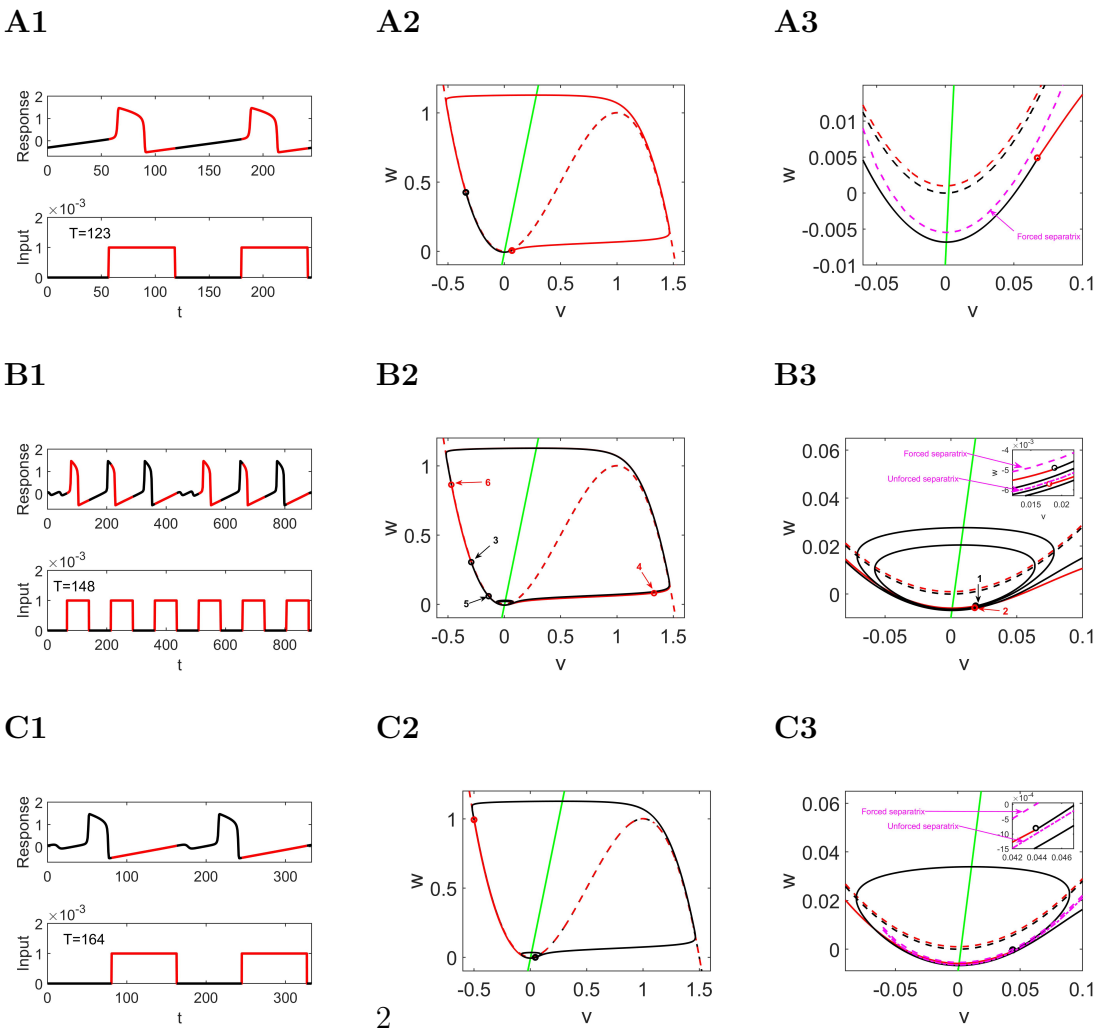

Figure A.10 Representative examples of 1:1 polyglot entrainment dynamics and their break-down. **Left column.** Time courses for v and the forcing. **Middle column.** Phase-plane diagrams. **Right column.** Phase-plane diagram magnification in vicinities of the knee of the v-nullclines. The black (red) portions of the v time courses and trajectories correspond to the forcing turned off (on). **A.** 1:1 entrainment for $T = 123$ (Fig. A.8-A3). **B.** 3:3 entrainment for $T = 148$ (Fig. A.8-A4). **C.** 1:1 entrainment for $T = 164$ (Fig. A.8-A5). We used the following parameter values $\alpha = 4$, $\lambda = 0.01$, $A = 0.001$ and $\epsilon = 0.01$ (Fig. A.8-A).

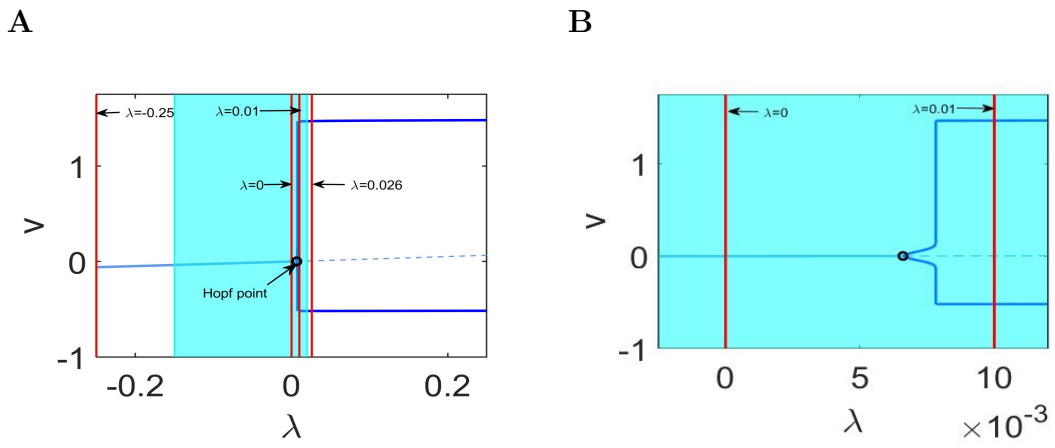

Figure A.11 Bifurcation diagram as a function of the parameter λ for $\alpha = 4$. We have Hopf bifurcation at $\lambda = 0.0066$. (a) The shaded region denote the λ values for the unforced system for which we have 1:1 polyglot entrainment. The red lines denote the representative λ values used in the previous figures for the unforced system. $\lambda = 0.026$ (Fig. A.6-A), $\lambda = -0.25$ (Fig. A.6-B & C), $\lambda = 0$ (Fig. A.7) and $\lambda = 0.01$ (Fig. A.8). (b) is the magnification of (a) around the Hopf point showing that Hopf bifurcation is supercritical.

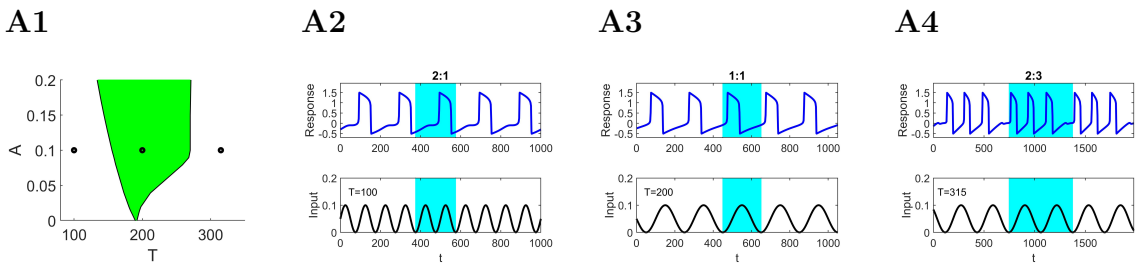

Figure A.12 Representative entrainment patterns and Arnold tongues with monoglot structure in response to sine-wave forcing. **A1** Arnold tongue showing 1:1 entrainment regions (highlighted in green). **Remaining panels.** Time courses for v and the forcing signal for the values of T and A indicated in A1 (black markers). We used the following parameter values: $\alpha = 2$, $\lambda = 0.04$, $\epsilon = 0.01$.

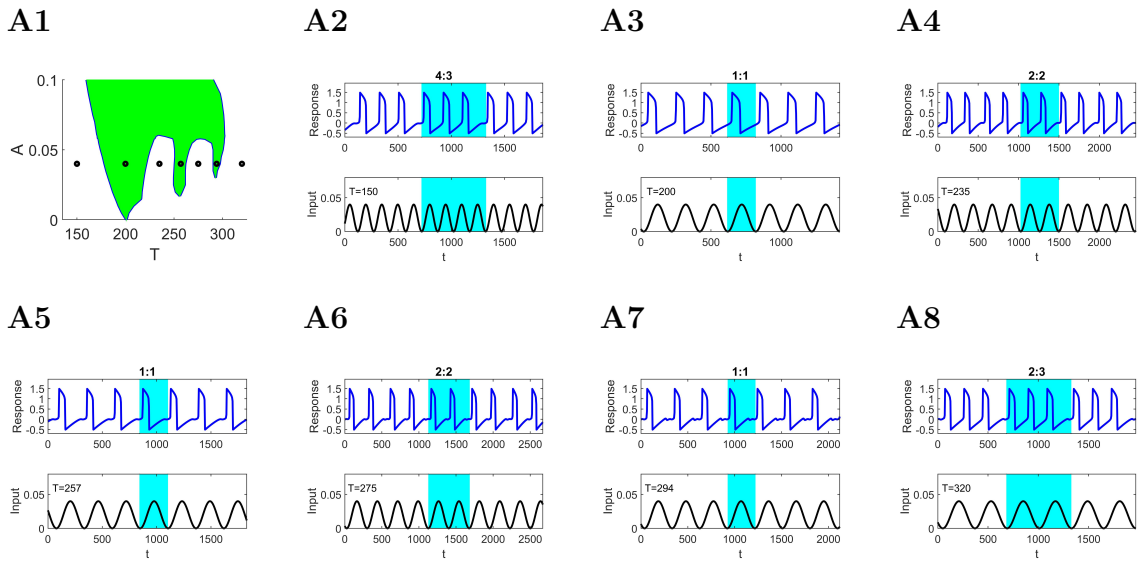

Figure A.13 Representative entrainment patterns and Arnold tongue with polyglot structure in response to sine-wave forcing. **A1** Arnold tongue showing 1:1 entrainment regions (highlighted in green). **Remaining panels.** Time courses for v and the forcing signal for the values of T and A indicated in A1 (black markers). We used the following parameter values: $\alpha = 2$, $\lambda = 0.016$, $\epsilon = 0.01$.

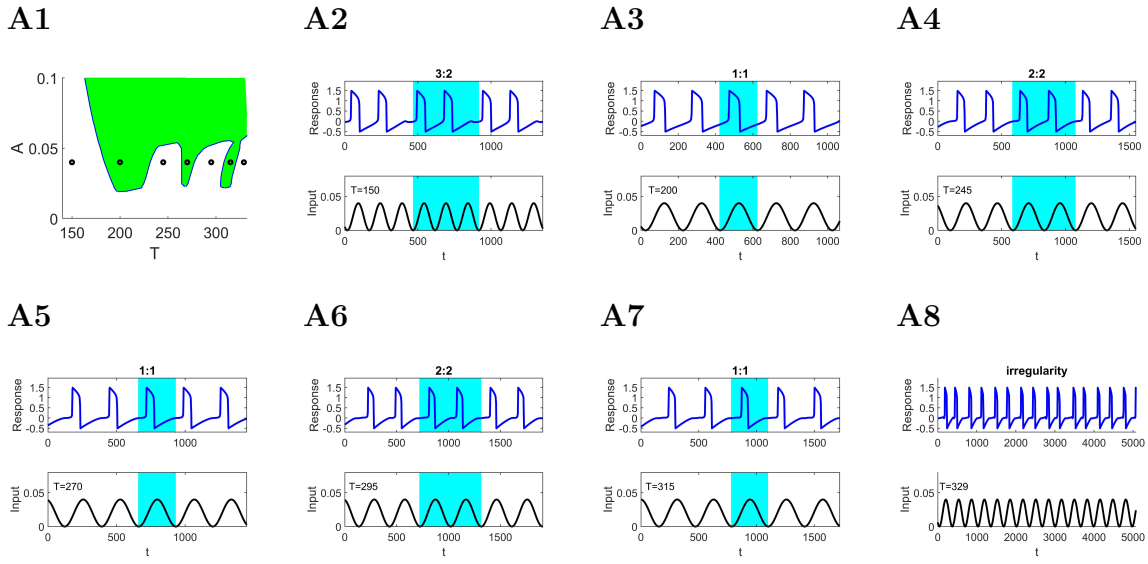

Figure A.14 Representative entrainment patterns and Arnold tongue with polyglot structure in response to sine-wave forcing. **A1** Arnold tongue showing 1:1 entrainment regions (highlighted in green). **Remaining panels.** Time courses for v and the forcing signal for the values of T and A indicated in A1 (black markers). We used the following parameter values: $\alpha = 2$, $\lambda = -0.01$, $\epsilon = 0.01$.

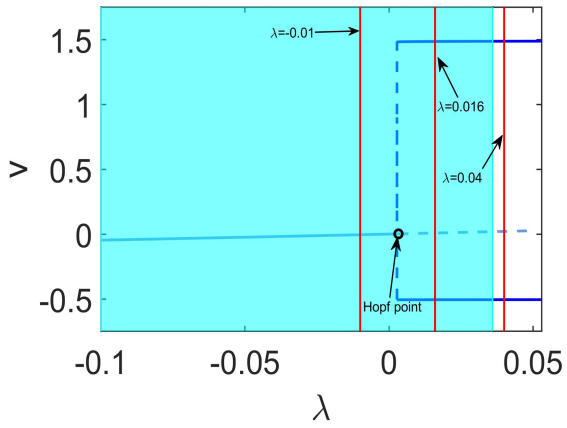

Figure A.15 Bifurcation diagram as a function of the parameter λ for $\alpha = 2$. We have subcritical Hopf bifurcation at $\lambda = 0.0033$. The shaded region denote the λ values for the unforced system for which we have 1:1 polyglot entrainment. The red lines denote the representative λ values used in the previous figures for the unforced system. $\lambda = 0.04$ (Fig. A.12-A1), $\lambda = 0.016$ (Fig. A.13-A1) and $\lambda = -0.01$ (Fig. A.14-A1)

APPENDIX B

ENTRAINMENT RESPONSES FOR OTHER PARAMETER REGIMES IN THE RUST MODEL AND BYRNE MODEL

In Chapter 5, we showed monolgot and polyglot entrainment responses for the Rust and Byrne Models under square-wave periodic forcing in the vicinity of one Hopf point. Here, we show results in the vicinity of another Hopf point.

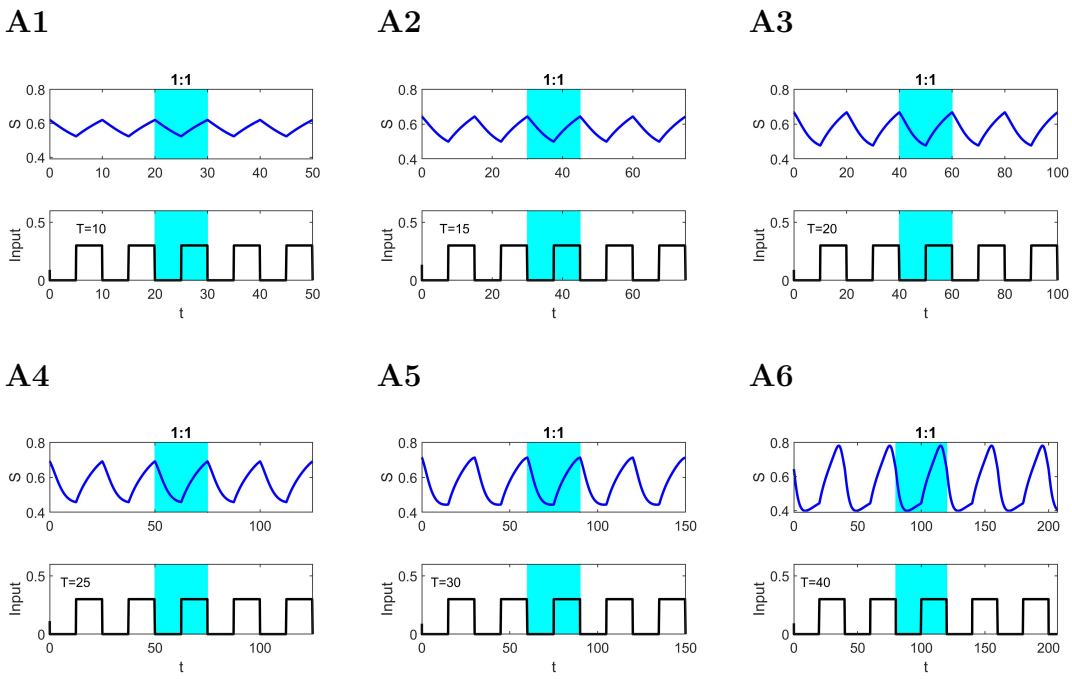

Figure B.1 Representative time course patterns for the Rust model in response to square-wave forcing for the fixed $A = 0.3$ and different period of the forcing T. An unforced system has damped oscillations and the stable fixed point lies in the vicinity of subcritical Hopf bifurcation (KaiA = 1.65).

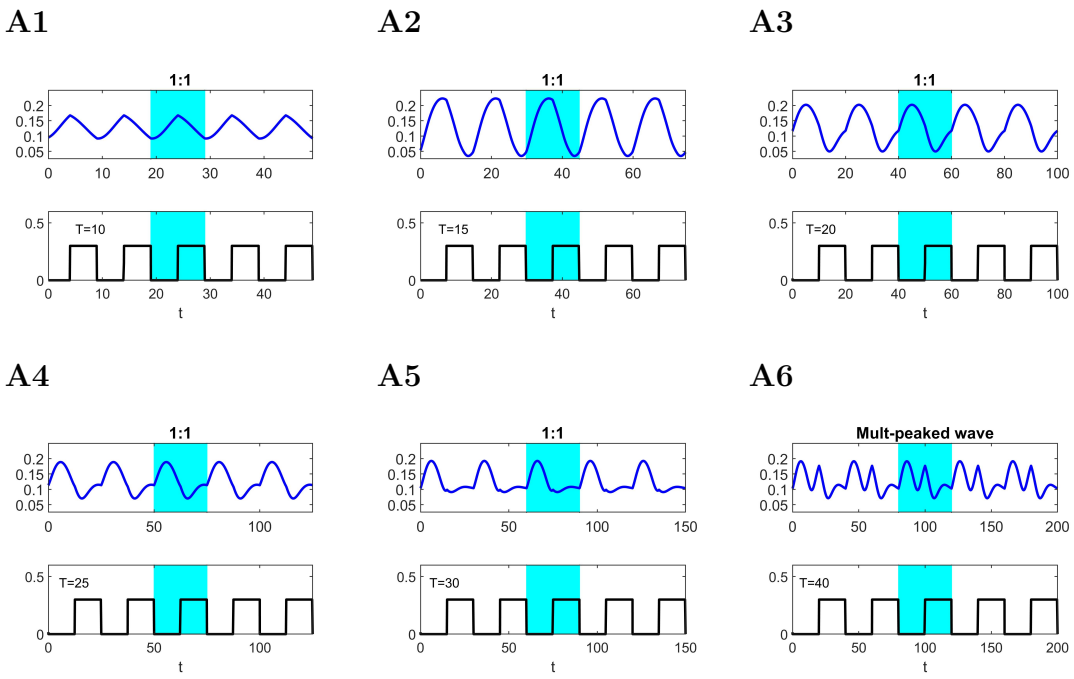

Figure B.2 Representative time course patterns for the Byrne model in response to square-wave forcing for the fixed $A = 0.3$ and different period of the forcing T. An unforced system has damped oscillations and the stable fixed point lies in the vicinity of first subcritical Hopf bifurcation ($E_0 = 0.135$).

REFERENCES

[1] Aihara, K., Matsumoto, G., and Ikegaya, Y. Periodic and non-periodic responses of a periodically forced hodgkin-huxley oscillator. *Journal of Theoretical Biology 109*, 2 (1984), 249–269.

[2] Arbel-Goren, R., Buonfiglio, V., Di Patti, F., Camargo, S., Valladares, A., Flores, E., Herrero, A., Fanelli, D., and Stavans, J. Robust, coherent and synchronized circadian clock-controlled oscillations along anabaena filaments. *Elife 10* (2021), e64348.

[3] Aronson, D. G., McGehee, R. P., Kevrekidis, I. G., and Aris, R. Entrainment regions for periodically forced oscillators. *Physical Review A 33*, 3 (1986), 2190.

[4] Balanov, A., Janson, N., Postnov, D., and Sosnovtseva, O. *Synchronization: From Simple to Complex*. Heidelberg, Berlin, Springer Science & Business Media, 2008.

[5] Başar, E., Başar-Eroglu, C., Karakaş, S., and Schürmann, M. Gamma, alpha, delta, and theta oscillations govern cognitive processes. *International Journal of Psychophysiology 39*, 2-3 (2001), 241–248.

[6] Beer, K., Joschinski, J., Sastre, A. A., Krauss, J., and Helfrich-Förster, C. A damping circadian clock drives weak oscillations in metabolism and locomotor activity of aphids (acyrthosiphon pisum). *Scientific Reports 7*, 1 (2017), 14906.

[7] Bernard, S., Gonze, D., Čajavec, B., Herzel, H., and Kramer, A. Synchronization-induced rhythmicity of circadian oscillators in the suprachiasmatic nucleus. *PLOS Computational Biology 3*, 4 (2007), e68.

[8] Bertram, R., Satin, L. S., Pedersen, M. G., Luciani, D. S., and Sherman, A. Interaction of glycolysis and mitochondrial respiration in metabolic oscillations of pancreatic islets. *Biophysical Journal 92*, 5 (2007), 1544–1555.

[9] Brown, S. A., Kowalska, E., and Dallmann, R. (Re) inventing the circadian feedback loop. *Developmental Cell 22*, 3 (2012), 477–487.

[10] Brunner, M., and Schafmeier, T. Transcriptional and post-transcriptional regulation of the circadian clock of cyanobacteria and neurospora. *Genes & Development 20*, 9 (2006), 1061–1074.

[11] Burden, R. L., and Faires, J. D. Numerical analysis pws. *Kent Publishing Co. Boston* (1989).

[12] Byrne, M. Simple post-translational circadian clock models from selective sequestration. *arXiv preprint arXiv:2002.08501* (2020).

[13] Chang, Y.-G., Cohen, S. E., Phong, C., Myers, W. K., Kim, Y.-I., Tseng, R., Lin, J., Zhang, L., Boyd, J. S., Lee, Y., et al. A protein fold switch joins the circadian oscillator to clock output in cyanobacteria. *Science 349*, 6245 (2015), 324–328.

[14] Chew, J., Leypunskiy, E., Lin, J., Murugan, A., and Rust, M. J. High protein copy number is required to suppress stochasticity in the cyanobacterial circadian clock. *Nature Communications 9*, 1 (2018), 1–10.

[15] Cohen, S. E., and Golden, S. S. Circadian rhythms in cyanobacteria. *Microbiology and Molecular Biology Reviews 79*, 4 (2015), 373–385.

[16] Croisier, H. *Continuation and bifurcation analyses of a periodically forced slow-fast system*. PhD thesis, Phd thesis, Academie Wallonie-Europe, Université de Liége, Liége, Wallonia, 2009.

[17] Di Bernardo, M., Budd, C. J., Champneys, A. R., Kowalczyk, P., Nordmark, A. B., Tost, G. O., and Piiroinen, P. T. Bifurcations in nonsmooth dynamical systems. *SIAM Review 50*, 4 (2008), 629–701.

[18] Diekman, C. O., and Bose, A. Entrainment maps: A new tool for understanding properties of circadian oscillator models. *Journal of Biological Rhythms 31*, 6 (2016), 598–616.

[19] Ditty, J., Mackey, S. R., and Johnson, C. H. *Bacterial Circadian Programs*. Heidelberg, Berlin, Springer Science & Business Media, 2009.

[20] Dumortier, F. Techniques in the theory of local bifurcations: Blow-up, normal forms, nilpotent bifurcations, singular perturbations. In *Bifurcations and Periodic Orbits of Vector Fields*. Springer, 1993, pp. 19–73.

[21] Dumortier, F., Roussarie, R., and Roussarie, R. H. *Canard Cycles and Center Manifolds*, vol. 577. Providence, Rhode Island, American Mathematical Soc., 1996.

[22] Dunlap, J. C. Molecular bases for circadian clocks. *Cell 96*, 2 (1999), 271–290.

[23] Eckhaus, W. Relaxation oscillations including a standard chase on french ducks. In *Asymptotic Analysis II*. TA, Utrecht, Springer, 1983, pp. 449–497.

[24] Ermentrout, B. *Simulating, Analyzing, and Animating Dynamical Systems: A Guide to XPPAUT for Researchers and Students*. SIAM, 2002.

[25] Español, M. I., and Rotstein, H. G. Complex mixed-mode oscillatory patterns in a periodically forced excitable belousov-zhabotinsky reaction model. *Chaos: An Interdisciplinary Journal of Nonlinear Science 25*, 6 (2015), 064612.

[26] Fenichel, N. Geometric singular perturbation theory for ordinary differential equations. *Journal of Differential Equations 31*, 1 (1979), 53–98.

[27] Field, R. J., and Noyes, R. M. Oscillations in chemical systems. iv. limit cycle behavior in a model of a real chemical reaction. *The Journal of Chemical Physics 60*, 5 (1974), 1877–1884.

[28] FitzHugh, R. Mathematical models of threshold phenomena in the nerve membrane. *The Bulletin of Mathematical Biophysics 17*, 4 (1955), 257–278.

[29] FitzHugh, R. Impulses and physiological states in theoretical models of nerve membrane. *Biophysical Journal 1*, 6 (1961), 445.

[30] Fries, P. A mechanism for cognitive dynamics: neuronal communication through neuronal coherence. *Trends in Cognitive Sciences 9*, 10 (2005), 474–480.

[31] Gallego, M., and Virshup, D. M. Post-translational modifications regulate the ticking of the circadian clock. *Nature Reviews Molecular Cell Biology 8*, 2 (2007), 139–148.

[32] Glass, L., and Bélair, J. Continuation of arnold tongues in mathematical models of periodically forced biological oscillators. In *Nonlinear Oscillations in Biology and Chemistry*. Springer, 1986, pp. 232–243.

[33] Gonze, D., and Abou-Jaoudé, W. The goodwin model: behind the hill function. *PlOS One 8*, 8 (2013), e69573.

[34] Gonze, D., Bernard, S., Waltermann, C., Kramer, A., and Herzel, H. Spontaneous synchronization of coupled circadian oscillators. *Biophysical Journal 89*, 1 (2005), 120–129.

[35] Goodwin, B. C. Oscillatory behavior in enzymatic control processes. *Advances in Enzyme Regulation 3* (1965), 425–437.

[36] Granada, A. E., and Herzel, H. How to achieve fast entrainment? the timescale to synchronization. *PlOS One 4*, 9 (2009), e7057.

[37] Ha, G. E., and Cheong, E. Spike frequency adaptation in neurons of the central nervous system. *Experimental Neurobiology 26*, 4 (2017), 179.

[38] Heltberg, M., Kellogg, R. A., Krishna, S., Tay, S., and Jensen, M. H. Noise induces hopping between nf-κb entrainment modes. *Cell Systems 3*, 6 (2016), 532–539.

[39] Heltberg, M. L., Krishna, S., Kadanoff, L. P., and Jensen, M. H. A tale of two rhythms: Locked clocks and chaos in biology. *Cell Systems 12*, 4 (2021), 291–303.

[40] Hirschie Johnson, C., Elliott, J. A., and Foster, R. Entrainment of circadian programs. *Chronobiology International 20*, 5 (2003), 741–774.

[41] Hodgkin, A. L., and Huxley, A. F. A quantitative description of membrane current and its application to conduction and excitation in nerve. *The Journal of Physiology 117*, 4 (1952), 500–544.

[42] Huang, R.-C. The discoveries of molecular mechanisms for the circadian rhythm: The 2017 nobel prize in physiology or medicine. *Biomedical Journal 41*, 1 (2018), 5–8.

[43] Hurley, J. M., Loros, J. J., and Dunlap, J. C. Circadian oscillators: around the transcription–translation feedback loop and on to output. *Trends in Biochemical Sciences 41*, 10 (2016), 834–846.

[44] Johnson, C. H., Stewart, P. L., and Egli, M. The cyanobacterial circadian system: from biophysics to bioevolution. *Annual Review of Biophysics 40* (2011), 143–167.

[45] Jolley, C. C., Ode, K. L., and Ueda, H. R. A design principle for a posttranslational biochemical oscillator. *Cell Reports 2*, 4 (2012), 938–950.

[46] Kageyama, H., Nishiwaki, T., Nakajima, M., Iwasaki, H., Oyama, T., and Kondo, T. Cyanobacterial circadian pacemaker: Kai protein complex dynamics in the kaic phosphorylation cycle in vitro. *Molecular Cell 23*, 2 (2006), 161–171.

[47] Karatsoreos, I. N., Bhagat, S., Bloss, E. B., Morrison, J. H., and McEwen, B. S. Disruption of circadian clocks has ramifications for metabolism, brain, and behavior. *Proceedings of the National Academy of Sciences* (2011), 201018375.

[48] Kawamoto, N., Ito, H., Tokuda, I. T., and Iwasaki, H. Damped circadian oscillation in the absence of kaia in synechococcus. *Nature Communications 11*, 1 (2020), 1–12.

[49] Keane, A., and Krauskopf, B. Chenciner bubbles and torus break-up in a periodically forced delay differential equation. *Nonlinearity 31*, 6 (2018), R165.

[50] Kim, J. K. Protein sequestration versus hill-type repression in circadian clock models. *IET Systems Biology 10*, 4 (2016), 125–135.

[51] Kim, Y.-I., Vinyard, D. J., Ananyev, G. M., Dismukes, G. C., and Golden, S. S. Oxidized quinones signal onset of darkness directly to the cyanobacterial circadian oscillator. *Proceedings of the National Academy of Sciences 109*, 44 (2012), 17765–17769.

[52] Komin, N., Murza, A. C., Hernández-García, E., and Toral, R. Synchronization and entrainment of coupled circadian oscillators. *Interface Focus 1*, 1 (2010), 167–176.

[53] Kondo, T., Strayer, C. A., Kulkarni, R. D., Taylor, W., Ishiura, M., Golden, S. S., and Johnson, C. H. Circadian rhythms in prokaryotes: luciferase as a reporter of circadian gene expression in cyanobacteria. *Proceedings of the National Academy of Sciences 90*, 12 (1993), 5672–5676.

[54] Kondo, T., Tsinoremas, N. F., Golden, S. S., Johnson, C. H., et al. Circadian clock mutants of cyanobacteria. *Science 266*, 5188 (1994), 1233.

[55] Krupa, M., and Szmolyan, P. Relaxation oscillation and canard explosion. *Journal of Differential Equations 174*, 2 (2001), 312–368.

[56] Kurosawa, G., Aihara, K., and Iwasa, Y. A model for the circadian rhythm of cyanobacteria that maintains oscillation without gene expression. *Biophysical Journal 91*, 6 (2006), 2015–2023.

[57] Lee, C., Etchegaray, J.-P., Cagampang, F. R., Loudon, A. S., and Reppert, S. M. Posttranslational mechanisms regulate the mammalian circadian clock. *Cell 107*, 7 (2001), 855–867.

[58] Leine, R., and Van Campen, D. Bifurcation phenomena in non-smooth dynamical systems. *European Journal of Mechanics-A/Solids 25*, 4 (2006), 595–616.

[59] Lengyel, I., and Epstein, I. R. Modeling of turing structures in the chloriteiodidemalonic acidstarch reaction system. *Science 251*, 4994 (1991), 650–652.

[60] Lengyel, I., and Epstein, I. R. A chemical approach to designing turing patterns in reaction-diffusion systems. *Proceedings of the National Academy of Sciences 89*, 9 (1992), 3977–3979.

[61] Liao, G., Diekman, C., and Bose, A. Entrainment dynamics of forced hierarchical circadian systems revealed by 2-dimensional maps. *SIAM Journal on Applied Dynamical Systems 19*, 3 (2020), 2135–2161.

[62] Makarenkov, O., and Lamb, J. S. Dynamics and bifurcations of nonsmooth systems: A survey. *Physica D: Nonlinear Phenomena 241*, 22 (2012), 1826–1844.

[63] Medvedev, A., Mattsson, P., Zhusubaliyev, Z. T., and Avrutin, V. Nonlinear dynamics and entrainment in a continuously forced pulse-modulated model of testosterone regulation. *Nonlinear Dynamics 94*, 2 (2018), 1165–1181.

[64] Mehra, A., Baker, C. L., Loros, J. J., and Dunlap, J. C. Post-translational modifications in circadian rhythms. *Trends in Biochemical Sciences 34*, 10 (2009), 483–490.

[65] Mohawk, J. A., Green, C. B., and Takahashi, J. S. Central and peripheral circadian clocks in mammals. *Annual Review of Neuroscience 35* (2012), 445–462.

[66] Monti, M., Lubensky, D. K., and Ten Wolde, P. R. Robustness of clocks to input noise. *Physical Review Letters 121*, 7 (2018), 078101.

[67] Morris, C., and Lecar, H. Voltage oscillations in the barnacle giant muscle fiber. *Biophysical Journal 35*, 1 (1981), 193–213.

[68] Nagumo, J., Arimoto, S., and Yoshizawa, S. An active pulse transmission line simulating nerve axon. *Proceedings of the Institute of Radio Engineers 50*, 10 (1962), 2061–2070.

[69] Nakajima, M., Imai, K., Ito, H., Nishiwaki, T., Murayama, Y., Iwasaki, H., Oyama, T., and Kondo, T. Reconstitution of circadian oscillation of cyanobacterial kaic phosphorylation in vitro. *Science 308*, 5720 (2005), 414–415.

[70] Nakajima, M., Ito, H., and Kondo, T. In vitro regulation of circadian phosphorylation rhythm of cyanobacterial clock protein kaic by kaia and kaib. *FEBS Letters 584*, 5 (2010), 898–902.

[71] Notbohm, A., Kurths, J., and Herrmann, C. S. Modification of brain oscillations via rhythmic light stimulation provides evidence for entrainment but not for superposition of event-related responses. *Frontiers in Human Neuroscience 10* (2016), 10.

[72] Novák, B., and Tyson, J. J. Design principles of biochemical oscillators. *Nature Reviews Molecular Cell Biology 9*, 12 (2008), 981–991.

[73] Osipov, G. V., Kurths, J., and Zhou, C. *Synchronization in Oscillatory Networks*. Heidelberg, Berlin, Springer Science & Business Media, 2007.

[74] Paijmans, J., Lubensky, D. K., and Ten Wolde, P. R. A thermodynamically consistent model of the post-translational kai circadian clock. *PLOS Computational Biology 13*, 3 (2017), e1005415.

[75] Pattanayak, G. K., Phong, C., and Rust, M. J. Rhythms in energy storage control the ability of the cyanobacterial circadian clock to reset. *Current Biology 24*, 16 (2014), 1934–1938.

[76] Phong, C., Markson, J. S., Wilhoite, C. M., and Rust, M. J. Robust and tunable circadian rhythms from differentially sensitive catalytic domains. *Proceedings of the National Academy of Sciences 110*, 3 (2013), 1124–1129.

[77] Pikovsky, A., Rosenblum, M., and Kurths, J. *Synchronization: A Universal Concept in Nonlinear Sciences*, vol. 12. Cambridge, Cambridge university press, 2003.

[78] Roenneberg, T., Daan, S., and Merrow, M. The art of entrainment. *Journal of Biological Rhythms 18*, 3 (2003), 183–194.

[79] Rotstein, H. G., Coombes, S., and Gheorghe, A. M. Canard-like explosion of limit cycles in two-dimensional piecewise-linear models of fitzhugh–nagumo type. *SIAM Journal on Applied Dynamical Systems 11*, 1 (2012), 135–180.

[80] Rust, M. J., Golden, S. S., and OShea, E. K. Light-driven changes in energy metabolism directly entrain the cyanobacterial circadian oscillator. *Science 331*, 6014 (2011), 220–223.

[81] Rust, M. J., Markson, J. S., Lane, W. S., Fisher, D. S., and O'Shea, E. K. Ordered phosphorylation governs oscillation of a three-protein circadian clock. *Science 318*, 5851 (2007), 809–812.

[82] Sato, M., Hyodo, H., Biwa, T., and Delage, R. Synchronization of thermoacoustic quasiperiodic oscillation by periodic external force. *Chaos: An Interdisciplinary Journal of Nonlinear Science 30*, 6 (2020), 063130.

[83] Schmal, C., Myung, J., Herzel, H., and Bordyugov, G. A theoretical study on seasonality. *Frontiers in Neurology 6* (2015), 94.

[84] Schnitzler, A., and Gross, J. Normal and pathological oscillatory communication in the brain. *Nature Reviews Neuroscience 6*, 4 (2005), 285–296.

[85] Sel'Kov, E. Self-oscillations in glycolysis 1. a simple kinetic model. *European Journal of Biochemistry 4*, 1 (1968), 79–86.

[86] Shabunin, A., Astakhov, V., Demidov, V., Provata, A., Baras, F., Nicolis, G., and Anishchenko, V. Modeling chemical reactions by forced limit-cycle oscillator: synchronization phenomena and transition to chaos. *Chaos, Solitons & Fractals 15*, 2 (2003), 395–405.

[87] Smolen, P., Baxter, D. A., and Byrne, J. H. Modeling circadian oscillations with interlocking positive and negative feedback loops. *Journal of Neuroscience 21*, 17 (2001), 6644–6656.

[88] Strogatz, S. H. *Nonlinear Dynamics and Chaos with Student Solutions Manual: With Applications to Physics, Biology, Chemistry, and Engineering*. Ithaca, New York, CRC press, 2018.

[89] Swan, J. A., Golden, S. S., LiWang, A., and Partch, C. L. Structure, function, and mechanism of the core circadian clock in cyanobacteria. *Journal of Biological Chemistry 293*, 14 (2018), 5026–5034.

[90] Tomita, J., Nakajima, M., Kondo, T., and Iwasaki, H. No transcription-translation feedback in circadian rhythm of kaic phosphorylation. *Science 307*, 5707 (2005), 251–254.

[91] Tyson, J. J., Hong, C. I., Thron, C. D., and Novak, B. A simple model of circadian rhythms based on dimerization and proteolysis of per and tim. *Biophysical Journal 77*, 5 (1999), 2411–2417.

[92] van Zon, J. S., Lubensky, D. K., Altena, P. R., and ten Wolde, P. R. An allosteric model of circadian kaic phosphorylation. *Proceedings of the National Academy of Sciences 104*, 18 (2007), 7420–7425.

[93] Vincent, U., and Kenfack, A. Synchronization and bifurcation structures in coupled periodically forced non-identical duffing oscillators. *Physica Scripta 77*, 4 (2008), 045005.

[94] Von Stein, A., and Sarnthein, J. Different frequencies for different scales of cortical integration: from local gamma to long range alpha/theta synchronization. *International Journal of Psychophysiology 38*, 3 (2000), 301–313.

[95] Webb, A. B., Angelo, N., Huettner, J. E., and Herzog, E. D. Intrinsic, nondeterministic circadian rhythm generation in identified mammalian neurons. *Proceedings of the National Academy of Sciences 106*, 38 (2009), 16493–16498.

[96] Westermark, P. O., Welsh, D. K., Okamura, H., and Herzel, H. Quantification of circadian rhythms in single cells. *PLOS Computational Biology 5*, 11 (2009), e1000580.

[97] Winfree, A. T. *The Geometry of Biological Time*, vol. 12. New York, Springer Science & Business Media, 2001.

[98] Woelfle, M. A., Ouyang, Y., Phanvijhitsiri, K., and Johnson, C. H. The adaptive value of circadian clocks: an experimental assessment in cyanobacteria. *Current Biology 14*, 16 (2004), 1481–1486.

[99] Woller, A., Gonze, D., and Erneux, T. The goodwin model revisited: Hopf bifurcation, limit-cycle, and periodic entrainment. *Physical Biology 11*, 4 (2014), 045002.

[100] Yoda, M., Eguchi, K., Terada, T. P., and Sasai, M. Monomer-shuffling and allosteric transition in kaic circadian oscillation. *PlOS One 2*, 5 (2007), e408.

[101] Zhabotinsky, A. M. A history of chemical oscillations and waves. *Chaos: An Interdisciplinary Journal of Nonlinear Science 1*, 4 (1991), 379–386.